The Pennsylvania State University

The Graduate School

Department of Chemistry

MICROMOTORS POWERED BY CATALYTIC REACTIONS AND THEIR APPLICATIONS

A Dissertation in

Chemistry

by

Shakuntala Sundararajan

Submitted in Partial Fulfillment
of the Requirements
for the Degree of

Doctor of Philosophy

May 2010

The dissertation of Shakuntala Sundararajan was reviewed and approved* by the following:

Ayusman Sen
Professor of Chemistry
Dissertation Advisor
Chair of Committee

Thomas E. Mallouk
DuPont Professor of Materials Chemistry and Physics

Mary E. Williams
Associate Professor of Chemistry

Jeffrey M. Catchmark
Associate Professor of Agricultural and Biological Engineering

Barbara J. Garrison
Shapiro Professor of Chemistry
Head of the Department of Chemistry

*Signatures are on file in the Graduate School

ABSTRACT

In this thesis the mechanism of motility and applications, of micro-sized, autonomously powered, platinum – gold (Pt-Au) motors are discussed. The Sen group had previously reported powered motion of striped Pt-Au motors (2 µm in length and 360 nm in diameter) in aqueous hydrogen peroxide (H_2O_2) 'fuel' solutions. The motors move at speeds of 5 – 10 µm/s. Transduction of the chemical energy derived from the catalytic conversion of H_2O_2 to products (H_2O and O_2), on the bimetallic motor surface results in the observed motility. The motility of these synthetic micromotors is comparable to that of micro-sized flagellar bacteria that convert chemical energy from ATP hydrolysis to power themselves at speeds of few body lengths per second.

Initially, the catalytic decomposition of the peroxide substrate was thought to occur at Pt end alone and the motility was ascribed to interfacial effects. According to this hypothesis, the hydrophobicity of the Au end powered the motor Pt end forward due to the lower interfacial tension at the O_2 rich environment. However, further investigation revealed the possibility of bipolar H_2O_2 decomposition, with both Pt and Au participating in fuel consumption. When bulk Au and Pt wires were placed in aqueous H_2O_2 solutions a current was observed indicating an electrochemical pathway for fuel decomposition. In the electrochemical pathway for peroxide decomposition, H_2O_2 is oxidized to O_2 at the Pt anode, and reduced to H_2O at the Au cathode. Based on the bipolar fuel decomposition, a self-electrophoretic mechanism for rod motility was proposed. According to this hypothesis, the electron current from Pt anode to Au cathode in the rod is accompanied by concomitant proton flux in the surrounding fluid. As the protons migrate from one end

to another an electroosmotic fluid flow occurs from Pt to Au, resulting in motor propulsion Pt end forward. Several approaches have been adopted to verify this hypothesis. The approach described in this thesis was to alter the surface charge of the motor. By analogy to electrophoresis where oppositely charged colloidal particles move in opposing directions in presence of an external field, self-electrophoretic micro-motors of opposite charges should also move in opposite directions. Negatively charged Pt-Au rods move Pt end forward. On altering the surface charge of the motors and rendering them positively charged, the rods were found to move Au end forward. The experiments relating to mechanism of motor motility are discussed in chapter 2.

Synthetic Pt-Au motors could be used as agents for transport and delivery of materials in the microscale regime. In chapter 3, the application of Pt-Au motors for transport of colloidal cargo is demonstrated. A couple of methods for attachment of prototypical microsphere cargo to Pt-Au motors were explored. In the first method, electrostatic attractive forces were used to attach positively charged, amidine functionalized, microsphere cargo to negatively charged Pt-Au-Polypyrrole (PPy) rods. The PPy end of the rod bears a higher negative charge than the metallic segment and the cargo preferably attached to that end. For the second mode of cargo attachment, the more specific biotin-streptavidin based interaction was used. A monolayer of a biotin terminated dithiol was formed on the gold end. Streptavidin-coated microsphere cargo was then bound to the biotin functionalized end of the rod. Motor-cargo doublets were found to exhibit motility. Subsequently, a quantitative study of the effect of cargo diameter on motor speed was performed. As the cargo diameter was increased, the motor-cargo doublet speed decreased due to increasing drag contribution from larger cargo. The

drag force on the doublets was computed and the speeds predicted by theory were found to be in close agreement with empirically observed speeds.

For maneuvering matter in the mesoscale, in addition to cargo transport the ability to deliver the payloads at desired locations is essential. In chapter 4 strategies for UV-light induced drop-off of cargo attached to motors are described. Applications of Pt-Au motors for delivery of materials or assembly of structures in the meso scale require transport and delivery of cargo. Two strategies for cargo drop-off were explored. In both methods, the link holding the motor and cargo snapped upon exposure to UV light. In the first approach the motor design incorporated Ag segments. Pt-Au-Ag-Au-PPy motors were attached to amidine functionalized cargo. This mode of cargo drop-off was based on the rapid dissolution of the Ag segment in the presence of UV light and chloride ions. In the second mode of cargo drop-off, a bifunctional linker with a photocleavable moiety was synthesized. The photocleavable moiety of the molecule was flanked by an amino group on one end and biotin on the other end. Pt-Au-PPy-PPyCOOH motors were synthesized. Carboxyl groups incorporated in the polymeric segment of the rods facilitated covalent attachment to the amine terminus of the bifunctional linker molecule via amide bond formation. The biotin end of the linker molecule was used to attach streptavidin-coated cargo to the motors. Upon exposure to UV light, the photocleavage of the linker molecule occurred, releasing the cargo from the motor.

In chapter 5, the feasibility of powering microscale objects using enzymatic reactions is explored. In earlier chapters, the catalytic micromotor system was based on the bimetallic Pt-Au catalytic system. Motor performance can be improved by using better catalysts. Naturally occurring biocatalysts – enzymes, are among the most efficient

catalysts known. In addition to the efficacy in their action, enzymes catalyze a wide range of reactions. The plethora of enzymatic reactions can be explored for design of future chemical locomotors. The enzyme catalase, which catalyzes the decomposition of H_2O_2 to H_2O and O_2 was asymmetrically functionalized on 0.5 µm polystyrene microspheres. The diffusion coefficients of the particles were tracked in the presence and absence of H_2O_2 fuel solutions. In this system, no directed motility or enhancement in diffusion coefficient of the catalase functionalized particles was observed in the presence of substrate. The most likely cause for this may be the poor activity of the enzyme, post-immobilization. Further investigation of this system is required to determine whether asymmetric gradients of neutral species can power microscale objects.

TABLE OF CONTENTS

LIST OF FIGURES

ACKNOWLEDGEMENTS

First I would like to thank my advisor, Dr. Sen, for encouraging me to work on interesting and challenging projects. I immensely appreciate his role in creating a work atmosphere where collaborations, regular discussions and constant learning were encouraged. Above all I appreciate his patience when I was faced with challenging times in my projects. I also want to thank Dr. Mallouk for his input and encouragement in weekly meetings. His scientific curiosity and optimism have been inspiring. I would also like to thank my other committee members Dr. Williams and Dr. Catchmark for their support and advice. I thank Dr. Velegol for the discussions we had on several projects. He acted as a sounding board for ideas and helped in troubleshooting on several occasions.

To Wally Paxton and Tim Kline I owe thanks for getting me started on the motors project. Thanks to Mike Ibele for providing much needed diversions (in the form of YouTube videos) to make some days more endurable. Thanks to Shikchya Tandukar, Dave Newsham, Angel Ugrinov, Sam Sengupta, Natallia Kulyba, Shraddha Surve, other Sen group members, Yang Wang, Paul Lammert, Young-Moo Byun, and the staff at the Penn State MRI, especially John McIntosh. I owe thanks to Eve Hong for far too many things. So I will just say ‘thanks’. Her role in helping me cultivate a liking for ‘all things coffee’ deserves special mention.

Thanks are due to my friends at A.I.D., Curtain Call, music lessons and roommates who helped me adjust to grad school and provided some memorable times during my stay at Penn State. Thanks to Anirban, Somesh, Vikas and Bhavana for their immense help during the last leg of my stay at State College.

Finally I would like to thank my family for their never-ending support: My father for his constant encouragement and instilling in me a sense of perspective; my mother for her *occasional* phone calls, *rasam podi* and for showing me the importance of perseverance; and my brother J for encouraging me to apply to grad school, and buying some of the best science books without which I may never have chosen to study chemistry. I would also like to thank J and Anu for the relaxing and enjoyable times spent with them on my time away from grad school. I hope their tendency for giving career related advice and more importantly, gift-giving does not cease when I leave grad school.

Chapter 1

Introduction

Motion in the macroscale world is easily achieved by using engines that consume chemical fuel directly or indirectly by drawing power from energy storage devices. Our day to day world is populated with a wide variety of man made machines. The diversity of their applications as well as performance is constantly improving. In recent years there has been a spurt in research in micron and sub-micron regime. Investigating properties of matter in micro/nano scale has revealed novel characteristics, giving rise to new applications. For example, the size dependent optical properties of noble metal nanoparticles and semiconductor quantum dots have been discovered and applications for the same, in the field of sensors has expanded tremendously.[1-4] While a lot of scientific knowledge exists on synthesis and tuning of properties of materials in the micro and nano regime, much needs to be explored. One such aspect is the ability to manipulate matter in the small scale and imparting motion to small scale objects.

1.1 Why Study Motility at the Micro and Nanoscale?

Some of the key motivations for understanding motion in the micro/nano scale are as follows:

1) Many motors found in nature are in the micron or sub-micron size regime. Biomotors perform several key tasks in living systems and do so with efficiencies that are

unparalleled in man made machinery. Two notable examples are the motor proteins (kinesins, myosins and dyneins) and the ubiquitous ATP synthase motor. Motor proteins are linear nanoscale motors that perform a variety of functions such as cytokinesis, signal transduction and intracellular material transport.[5] ATP synthase, another sub-micro scale biomotor, performs the important task of synthesizing ATP, the energy currency in biosystems. In some living systems, ATP synthase operates at an efficiency of greater than 80%.[6] While manmade machines can perform a wide variety of tasks, few can perform tasks as complex and as efficiently as those found in nature. A better understanding of the principles that govern motion in these and other miniature biomotors would aid us in making better synthetic machinery.

2) We may think of several novel applications where micromotors perform useful tasks. Microfluidic devices are already being used to replace bulk analytical techniques. Due to the small scale nature of these devices, analysis times are reduced and response times are faster.[7] Microscale motors that carry and deliver loads may find use as agents for bottom-up assembly of superstructures. Motors capable of material delivery may also be used to deliver small scale therapeutic agents to specific regions of the human body.

3) The laws of motion that govern motion in the macroscale no longer apply in the micron and sub-micron regime. Motion in macroscale world is governed by inertia whereas on the microscale, viscous forces dominate (i.e., low Reynolds number).[8-10] As a result, fluid flow profiles in the microscale are laminar rather than turbulent and viscous drag effectively eliminates any momentum based coasting of a micro/ nano object. Another factor to take into account is the dramatic increase in the surface to volume ratio. As the size of the object is scaled down, surface forces predominate over body forces.[8,11]

Additionally, since thermal diffusion of a micro/nano object is inversely proportional to its dimensions, a moving object in this size scale has to overcome the ever-present jostling due to Brownian motion.[12] So the question arises, how do we bring about motion in the micro/nano objects?

The most well known approaches for controlling motion of micro scale objects are electrophoresis and magnetophoresis.[13-15] Lesser known modes such as thermophoresis (migration due to thermal gradients) and diffusiophoresis (migration due to a concentration gradient) have also been used to achieve colloidal transport.[13,16,17] These approaches generate the ensemble response of particles suspended in solution. Optical trapping methods have been used to address individual or small groups of objects but the serial nature of this method would make it disadvantageous when dealing with larger particle populations.[18,19] The challenge lies in being able to impart to energy to an individual object to bring about its autonomous motion. Once this is achieved, more complex tasks such as drug delivery, bottom-up assembly of meso structures etc. can be envisioned. Figure **1-1** shows the design of a hypothetical micro/nanoscale transport system (from reference 20). Small scale motors can be engineered to pickup, transport and deliver materials along predetermined micro-channels.[20]

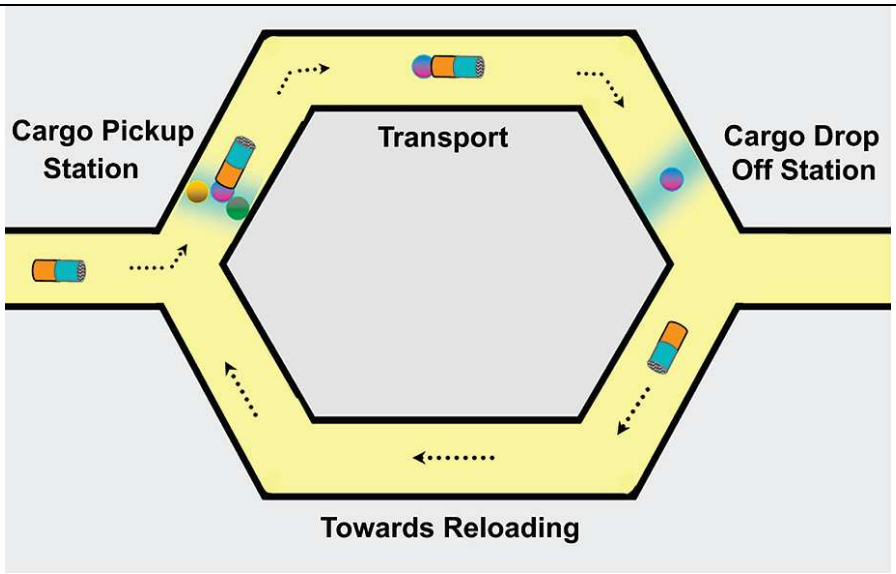

Figure **1-1** (from reference 20): Hypothetical design of a transport highway based on directed motion of artificial catalytic micro/nanomotors. The self-propelled motors load, transport, and deliver cargo along predetermined micro-fabricated tracks.

1.2 Designing Microscale Chemical Locomotors – Learning from Nature

While the versatility and efficacy of biomotors make them ideal models for artificial motors, the price to be paid is their structural complexity which in nearly impossible to replicate. However, two central features become evident when studying biomotor design: a) Incorporation and asymmetric placement of an onboard catalyst on the motile entity and b) Transduction of *locally* available chemical energy into mechanical energy to induce the motility of the object. Motors endowed with these characteristics exhibit autonomous propulsion independent of each other. Each object generates its own motive force through self-generated gradients. We and other groups

have adopted these features to design micro and macroscale catalytic motors capable of auto-propulsion in substrate solutions described in the remainder of this chapter.[21,22]

1.3 From Macroscale Motors to Microscale Catalytic Motors

The Sen group was the first to report the autonomous motion of synthetic Pt-Au based catalytic micromotors that exhibit autonomous motion in 'fuel' (aqueous H_2O_2 solutions) solutions.[23] These bimetallic, rod shaped, catalytic motors (2 µm in length and 370 nm in diameter) move Pt end forward, at average speeds of 10 µm/s in fuel solutions, Figure **1-2** (from reference 23).

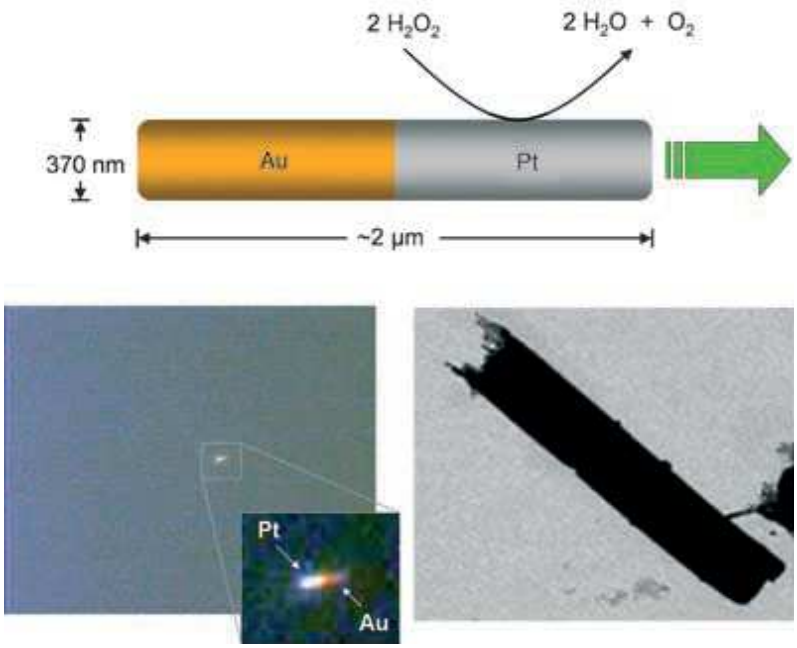

Figure **1-2** (from reference 23): Pt-Au catalytic micromotors: Top: Schematic of a Pt-Au motor. Bottom left: An optical micrograph (500×) of a Pt-Au rod. The rods move Pt end forward at speeds of 10 body lengths per second when placed in H_2O_2 solutions. Bottom right: Transmission electron micrograph of a Pt-Au rod. This was the first report of an artificial, self-propelled catalytic micromotor powered by the chemical decomposition of a 'fuel' (H_2O_2).

The inspiration for designing catalytic micromotors in the Sen group was a derived from a seminal paper from the Whitesides group.[22] In their report, the authors demonstrated autonomous motion of millimeter-sized PDMS disks with a Pt piece placed on one end of the disk, Figure **1-3** (from reference 22). When placed in a solution of aqueous H_2O_2, the disks moved on the air-liquid interface at speeds of few centimeters per second, with the Pt end tailing. The asymmetrically placed Pt piece catalyzed the decomposition of H_2O_2 substrate to O_2 and H_2O. The jet of O_2 bubbles emanating from one end of the object propelled it via a bubble propulsion mechanism in which the expansion and rupturing of bubbles provided the momentum for disk motion.

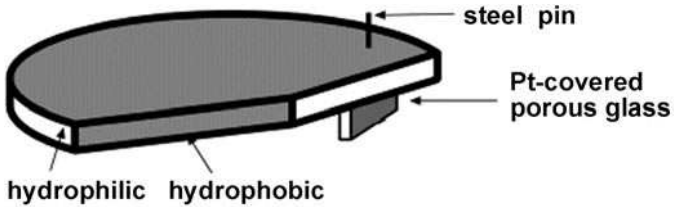

Figure **1-3** (from reference 22): Schematic of a self-propelling object consisting of a PDMS plate (ca. 1–2-mm thick and 9-mm diameter) and a 2 × 2 mm^2 piece of porous glass filter (covered with platinum by electron beam evaporation) mounted on the PDMS piece with a stainless steel pin.

In addition to autonomous motion, self-assembly of several such disks was achieved by tailoring their surface properties. The disks were modified to have both hydrophilic and hydrophobic regions on their periphery. The spontaneous motion facilitated inter-disk collision and upon close approach, the attractive forces arising from decrease in the total area of the air-water interface, resulted in disk self-assembly. Due to the catalyst based design motility was observed till all fuel in the surrounding media was consumed. The longevity of the disks proved to be crucial for facilitating the observation

of complex phenomena such as self assembly in non-biological systems, as the object itself was not consumed during the course of the motility imparting reaction.

1.3.1 Dissipative Chemical Locomotors

Prior to the Whitesides' report there were several reports of autonomous motion based on chemical and physical phenomena. In these systems, much like the Pt/PDMS system, the observed mechanical motion was intimately connected to a lowering in the free energy of the system via chemical or interfacial phenomena. These earlier reports however differ form the Pt/PDMS system in that, the object itself was gradually extinguished during the course of its motility. As a result, although autonomous motion was exhibited, it was short-lived. For instance, spontaneous motion of asymmetric mercury drops when placed in a solution of potassium dichromate and nitric acid was reported.[24] The reactants formed mercurous chromate that lowered the surface tension of the mercury surface. Subsequent contact with nitric acid cleansed the metal droplets' surface, exposing it to the dichromate. Once set into motion by some internal perturbation, the front of the crescent shaped drop is constantly exposed to fresh solution while the rear is surrounded by a product rich environment, thereby maintaining a difference between the leading and trailing sides of the moving mercury drop.

In another report, motion of camphor solids at the water-air interface was described. The dissolution of a piece of camphor lowers the air-water interfacial tension, propelling the solid to traverse the interface.[25] In yet another report, amphiphilic polymeric gels behaved in a similar fashion when swollen with tetrahydrofuran and

placed on a water surface. Much like the camphor boat system, gel motility arose due to lowering of the air-water surface tension resulting from the release the organic solvent.[26]

More recently, Toyota et al. described the self-propelled motion of surfactant 'fuel' droplets (10 -140 µm diameter) on a water surface. The catalytic hydrolysis of surfactant fuel droplets ((*N*-(4-[3-[trimethylamminio] ethoxy]benzylidene)-4-octylanilinebromide)) propelled them at speeds of 3 - 40 µm/s. The catalyst ([10-(4-formylphenoxy)decyl]imidazole hydrochloride) was dissolved in the droplet and facilitated its hydrolysis to the lipophilic 4-octylaniline and the hydrophilic 2-(2-formylphenoxy)ethyltrimethyl ammonium bromide. Once the hydrolysis reaction was initiated at a reactive site on the droplet surface, symmetry-breakage occurs due to product accumulation at those sites. This generation of reactant-rich and product-rich sites created an imbalance in interfacial tension, initiating droplet motion. Droplet motion was sustained till all the surfactant fuel was consumed.[27]

1.3.2 Catalytic Bubble-Propulsion Based Motors

In the examples described in the previous section, the motility is imparted to the object via a constantly reestablishing chemical and / or interfacial tension gradient. Due to the dissipative nature of these systems, the life-time of these chemical motors is limited. The use of an onboard catalyst in the Whitesides' PDMS/Pt system made it unique as the moving object itself was not extinguished during the course of its autonomous motion and motion was sustained till fuel was present in the surrounding media.

Since the Whitesides' report, there have been several reports of catalytic bubble-propulsion based systems. Feringa et al. reported two catalyst-based systems wherein bubble propulsion powered the motion of microscale particles. In the first report, the authors immobilized a manganese-based catalase mimic, rather than Pt to propel asymmetric silica particles (80 μm in diameter). Catalase is a naturally occurring enzyme that aids the breakdown of H_2O_2 to O_2 and water. The artificial catalase was functionalized all over the asymmetrically shaped silica particles.[28] In another report, the authors designed, a bi-enzymatic system in which naturally occurring catalase and glucose oxidase (GOx) were co-immobilized on multi-walled carbon nanotubes (MWCNT, 0.5 - 5.0 μm in length and 20-80 nm in diameter,).[29] Aggregates of the enzyme functionalized MWCNTs, (tens of μm in diameter) when placed in glucose solutions, exhibited translational motion. H_2O_2, the byproduct of glucose oxidation to δ-glucono-1,5-lactone, served as substrate for catalase. While neither system incorporated localized catalyst placement, motility in these systems was facilitated by the inhomogeneous distribution of bubble nucleation sites on the asymmetric particle.

More recently, Schmidt et al. described a novel microjet design consisting of conical tube shaped, catalytic microjets (100 μm in length and 5.5 μm in diameter), that exhibit motility in H_2O_2 solutions.[30] To fabricate these tube shaped motors, the authors deposited multi-metallic thin film layers (Pt-Au-Fe-Ti) on a sacrificial photoresist film. Upon dissolution of the photoresist, the metallic film spontaneously rolled into a tubular structure with each tube consisting of five windings of the film. The innermost Pt layer served as the catalyst for peroxide decomposition, the Fe layer facilitated remote control of the tube via an external magnetic field and the Ti and Au layers ensured good

adherence between the layers. The narrower end of the tube served as the entry point for the fuel which is converted to O_2 and water upon contact with the inner, catalytic, Pt layer. The O_2 bubbles collect, expand and are thrust out from the lager rear opening. The tubes were observed to move at speeds of 2 mm/s with the narrow end leading.

Another variation of the bubble propulsion motor was reported by Agrawal et al. wherein Pd nanoparticles coated resin beads (820 µm in diameter) exhibited vertical motion in H_2O_2 fuel solutions.[31] The resin particles exhibited maximum vertical velocities of nearly 0.6 cm/s and the motion resulted due to the buoyancy of the O_2 bubble trail that that lifted the beads from the bottom of the container. By altering the viscosity of the reaction medium, the authors were able to control the vertical speed; with increasing viscosity, the speed of the particles decreased.

1.3.3 Motility in the Microscale World vs. Macroscale World

From the video clips of object motility in the Whitesides, Feringa, Schmidt and Agrawal reports, it is evident the propulsion results from expansion of O_2 bubbles. The basis for motility of in these systems is very similar to the thrust-based propulsion that powers rocket vehicles where a stream of fast-moving fluid on one end of the rocket, pushes it in the opposite direction. In all the above mentioned systems, motion is described by Newtonian laws. These laws are applicable to the physics of macroscale objects where inertial forces play an important role in the objects motility.[9]

Motion in the microscale world is governed by viscous forces. The Reynolds number, *Re* is the ratio between inertial and viscous forces and gives us an idea of which force wins out in a given system, Equation **1.1**.

$$Re = \rho U L / \eta \qquad (\mathbf{1.1})$$

In Equation **1.1,** ρ is the fluid density, η is the viscosity, U and L particle velocity and radius, respectively. Motion in the macroscale regime (motion of automobiles, humans, bids etc.) is characterized by high *Re* values. Motion of micro objects is characterized by low *Re* (motion of microorganisms, artificial micromotors) and the viscous damping of the surrounding media quenches any momentum based coasting mechanisms of motion.[9] To get around this impediment, motile microorganisms move by what is known as non-reciprocal kinematics. In this kind of motion the organism itself or its appendages (flagella or cilia) undergo a series of cyclic deformations that are not time-reversible in nature. At the end of each cycle the organism undergoes translational motion. Discussion of non-reciprocal motion is beyond the scope of this chapter and more details may be found elsewhere. There have been several reports of artificial systems in the micro and meso scale that imitate biologically relevant mechanisms of non-reciprocal motion. While the non-reciprocal kinematics based motion described in these reports is fundamentally different from the mechanisms of motion employed by catalytic micromotors, the reports deserve mention as they have added to the pool of synthetic motors research and are described in brief below:

Ghosh et al. reported the design of non catalytic, magnetic propellers. The motor consisted of silica beads (200-300 nm in diameter) with a helical silica tail (1- 2 µm in

length) fabricated via glancing angle deposition.[32] The helical tails of the motors were coated with ferromagnetic cobalt. When an external magnetic field was used to guide and control the motion, the motors moved at speeds of 40 µm/s.. The helical structure of the motor imparted a rotation/translation coupling to the propeller motion, analogous to bacterial flagella. Whitesides et al. also reported the design of non-reciprocal swimmers in a rotating magnetic field. Using soft-lithographic techniques, flexible PDMS structures embedded with ferrite powder (2 - 10 mm long, 1 - 3 mm wide and 100 - 200 µm thick) were fabricated. An external rotating magnetic field was used to initiate and sustain the rotation of the tail like appendages ensuing in linear translation at a speed of 25 µm/s. This system with a *Re* range of 10^{-1} to 1 is classified into the low *Re* regime.[33]

The design of microscale catalytic locomotors has brought to light a new class of auto-propelled locomotors in low *Re* regime. Unlike non-reciprocal motion based swimmers, these motors rely on chemical reactions occurring on the objects' surface, to generate gradients, resulting in mechanical motion. In nearly all the reports of artificial microscale swimmers described hitherto, an imbalance in the osmotic pressure at opposite ends of microscale swimmer, generated by chemical reactions occurring on the object's surface responsible for the observed motility. Fluid flow occurs from one end of the body to the other as a result fields (electric, diffusiophoretic etc.) arising when substrate - product gradients are established.[34] These chemical micromotors continually pump fluid and plough their way through the viscous media they are immersed in.

1.4 Catalytic Micromotors

1.4.1 Controlling Motor Motion

Since our groups' report and investigation into rod motility, we and others have added to the toolbox of catalytic micromotor functions. Progress has been made to increase velocity, control trajectory and pattern of motion and perform application oriented tasks in catalytic micromotor systems. Pt-Au rods reported by our group move at average speeds of 10 μm/s. Wang et al. reported the dramatic increase in motor velocities by nearly ten times. In one example, the authors embedded carbon nanotubes (CNT) into the Pt segment of the motors. The incorporation of CNT increases the electrochemical activity of the motors toward H_2O_2 decomposition, Figure **1-4** .[20,35] The fabrication on Au-Ag segment, instead of single component Au segments and the use of H_2O_2 – hydrazine fuel mixtures resulted in fast motors that exhibited velocities up to 100 μm/s.[36] The predominant pattern of motion of Pt-Au rods is translational motion with meandering trajectories, while motion is circular trajectories or on the spot rotation is also seen. To gain better control over rod motion, several approaches have been adopted. In one of the earliest attempts by Sen et al., rods with magnetic Ni segments were synthesized. Using an external magnetic field, it was demonstrated that rods could be controlled to move in straighter paths or other desired trajectories.[37]

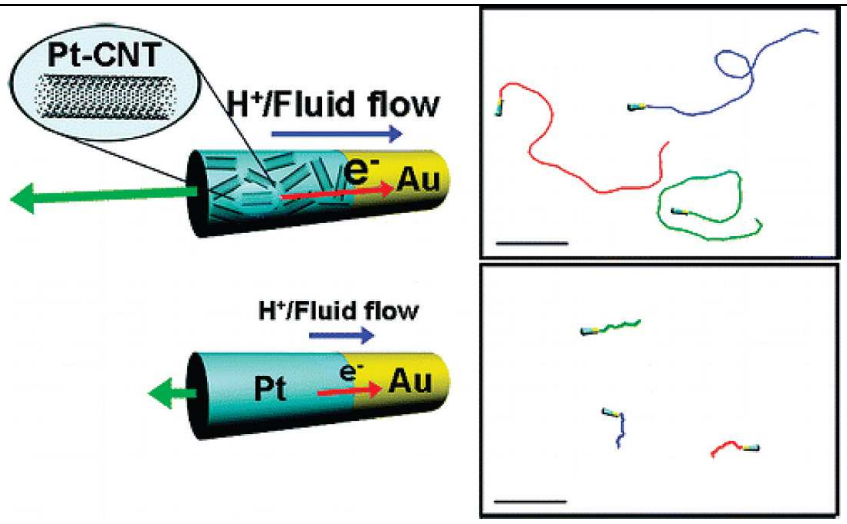

Figure **1-4** (from reference 36): Carbon nanotube (CNT)-induced high-speed catalytic Pt-Au based motors. (Right) Trajectories illustrating a typical motion and moving distances of Pt-Au motors (bottom) and Pt-Au/CNT (top) motors during a period of 4 s in the presence of 15 wt % hydrogen peroxide fuel. Scale bar = 45 µm. (Left) Schematic representation of the self-electrophoresis mechanism of a Pt-Au motors (bottom) and a Pt-Au/CNT (top) bipolar motor.

Zhao et al. used a dynamic shadowing growth to make Si-Pt or Si-Ag nanomotors capable of exhibiting a wide range of controllable motion like rotation, translation etc.[38] Dynamic shadowing deposition was used for growth of L-shaped and spring shaped silica scaffolds (3 µm length, 0.35 µm wide and 0.1 µm thick), followed by deposition of a catalytic metal (Pt or Ag). For a given motor design, a predominant pattern of motion was observed. For example, L-shaped motors were observed to rotate around a fixed point, whereas nano spring structures exhibited rotation motion resulting in a net translational displacement, due to the helical nature of the object. The mechanism of motility in this system is bubble propulsion resulting in motor speed of 10 µm/s.

In another report Zhao designed motors with a higher degree of control in rotational motion.[39] The motor consisted of 2 µm silica beads with a TiO_2 arm (3.5 µm in length and 0.5 µm in diameter). Pt metal was evaporated on one side of the TiO_2 arm.

The motors when placed in H_2O_2 fuel anchored to the surface and rotated freely about the nano arm axis. The authors were able to demonstrate finer control in rotational frequency by carefully varying H_2O_2 and surfactant concentrations.

Rotors of a different kind were fabricated lithographically by Catchmark et al. gold sprockets with a diameter of approximately 150 µm were decorated with platinum on one side of each tooth to impart catalytic asymmetry to the structure and resulted in rotary motion, Figure **1-5** (from reference 41).[40] The linear speed at the circumference of the rotors was 390 mm/s. Interestingly, the motion of the objects is towards the region of high concentration of product (oxygen), rather than away from it, unlike the larger structures described by the groups of Whitesides and Feringa and others.

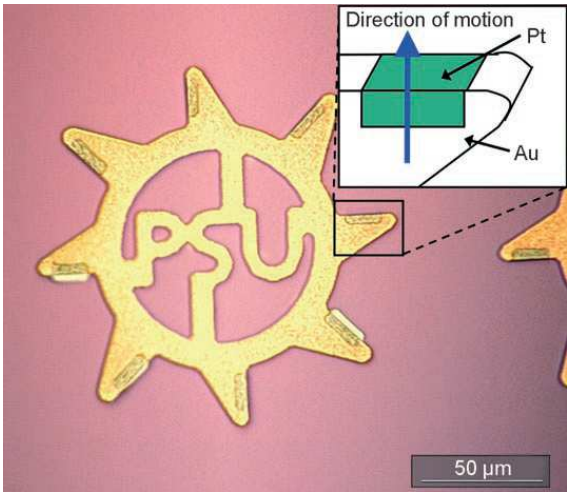

Figure **1-5** (from reference 41): Photograph of a gold gear-like structure with platinum deposited on the tooth regions. When placed in H_2O_2 solutions, the gears move anticlockwise, i.e. toward regions of higher O_2 concentrations unlike bubble propulsion based motors which move away from the jet of O_2 bubbles.

The Mirkin and Mallouk groups also reported synthesis of Pt-Au rod based motors that exhibited circular trajectories and rotation about a fixed point, respectively. In the Mirkin report, on-wire lithography (OWL) approach was adopted to passivate one

half of 5 µm Pt-Au rods with Au. Au was, deposited on along the long axis of the rod.[41] These motors were observed move in orbit-like paths at speeds of 10 to 20 rpms. Mallouk et al. fabricated tri-metallic rotors in which sequential vapor deposition was used to coat one half of Ru-Au motors along the longer rod axis, with Au and Pt layers, Figure **1-6** (from reference 43).[42] The vapor deposited Pt-Au layer adds a perpendicular force that moves the rod toward the center of the orbit induced by the asymmetric flow resulting pure rotatory (rotation about an axis) motion. In presence of 15% H_2O_2 the rods the rotors moved at speeds ranging from 180-400 rpms. A rudimentary analysis on of interaction between neighboring rotors was performed. Co-operative behavior among rotors was seen to occur at the micrometer length scale. Rotors spinning in the same direction were observed to maintain a tip-to tip distance of nearly 1 µm.

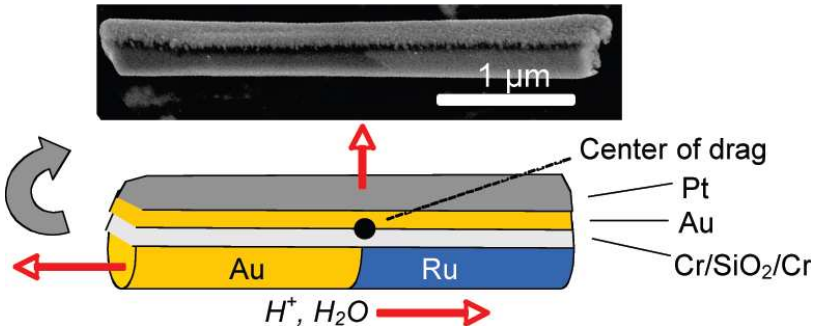

Figure **1-6** (from reference 43): (top) Field-emission scanning electron microscope image of an electrochemically grown Au-Ru micro rod with sequentially deposited Cr/ SiO_2/Cr, Au, and Pt layers. (bottom) Schematic drawing of the structure, showing the forces induced by catalytic H_2O_2 decomposition and the resulting rotary motion of the rod.

1.4.2 Imparting ‘On-Off’ Behavior to Motor Motility

In the next hierarchy of motor control, temperature and electrochemical triggers have been utilized to toggle rod motility between ‘on’ (fast-powered motion) and ‘off’ (slower powered motion or Brownian motion) states. Wang et al reported the thermal modulation of motor movement via application of heat pulses to the reaction medium.[43] The response of the motors to the thermal stimulus was found to be rapid and reversible. Speeds of rods switched from an average speed of 14 µm/s at 25 °C to nearly 45 µm/s at 65°C. The observed speed increase was attributed not only to the thermal activation of the disproportionation of H_2O_2 to the Pt and Au segments, but also to reduced fluid viscosity at higher temperatures.

In another report, ‘stop-start’ control of motor motion was achieved via an electrochemical trigger.[44] The potential for H_2O_2 reduction at the Pt surface was found to depend on O_2 concentrations. Lower the O_2 concentration; lower the electrochemical potential for H_2O_2 reduction. The O_2 levels in the medium were adjusted by application of a reduction potential and thereby depleting the O_2 concentration in the medium. Consequently, using the O_2 concentration as a knob, ‘stop-start’ behavior of motors was demonstrated. The switching of motor motion between ‘on’ and ‘off’ states would prove to be of use in scenarios where motors transport material during the ‘on’ state and are docked during the ‘off’ state during which payloads are dropped off or reattached.

1.4.3 Applications of Micromotors

Would micromotors be capable of transporting materials? Would attachment of payloads hinder the motion of these motors? Our group sought studied the feasibility of employing Pt-Au micromotors for transport of colloidal cargo.[45] In Chapter 3, strategies for attachment of microsphere cargo to Pt-Au motors are discussed. We found that motors still function after attachment of cargo, but as the cargo size was increased, motor speeds decreased. The effect of cargo size on motor speeds was quantified and compared to theory. A good agreement between observed and predicted motor speeds was seen. Wang et al also showed transport of colloidal cargo.[46] In their report, the authors synthesized Pt/Carbon nanotube-Au/Ni motors. The carbon nanotubes (CNT) embedded in the Pt segment aided in improving the catalytic activity of the motors, while the Ni segment was used to attach magnetic cargo to the motors. Cargo drop-off was also demonstrated by a magnetic torque based mechanism, Figure **1-7** (from reference 47).

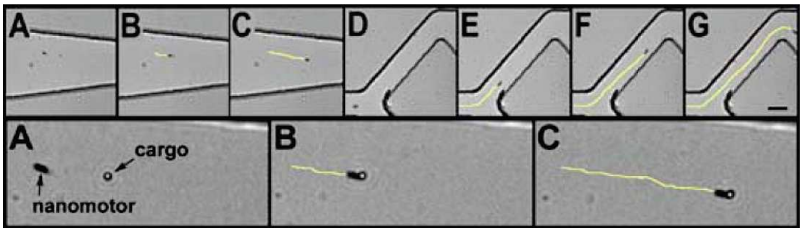

Figure **1-7** (from reference 47): Optical microscopy images of the dynamic loading of a Pt/Carbon nanotube-Au/Ni motor with a 1.3 μm diameter magnetic microsphere cargo (A-C). The motor transports the cargo through micro-fabricated (PDMS) micro channels (D-G). Scale bar in (G) = 25 μm. Bottom: magnified (× 3.5) images (A-C) of the top images (A-G).

When motor trajectory was changed by 180° by abruptly reversing the orientation of the

external magnetic field, the viscous forces overcame the weak magnetic interaction between motor and cargo resulting in release of the payload.

Our group adopted a different strategy wherein photochemical stimuli were used to exhibit cargo drop-off.[47] In chapter 4, two methods for cargo drop-off namely: I) silver dissolution assisted and II) photocleavable bi-functional linker assisted cargo delivery, are discussed in detail. In both routes, the bridge holding the motor and cargo snaps on exposure to UV light. The use of UV light as a trigger may allow for more precise control in delivery of cargo as compared to magnetic field-torque based methods. The use of implements like photomasks may be used to enable cargo drop-off at desired locations.

Application of synthetic micromotors is not confined to using them as agents of transport and delivery of materials at the microscale. Recently Wang et al. showed that Pt-Au motors may find use as Ag^+ ion sensors.[48] The authors discovered that in the presence of Ag^+ ions, the motor speeds increased due to Ag deposition on the Pt segment making it more catalytically active. A calibration study was performed to determine motor speeds at different Ag^+ ion concentrations. From the calibration curve, the quantity of Ag^+ ions in a medium containing unknown quantity of the ions may be determined by measuring the observed motor speeds in that medium.

Another novel application of Ag based catalytic motors was shown by Lee et al.[49] The authors demonstrated a facile method to produce ordered Si nanowire arrays using Ag based motors. A Si wafer coated with a film of Ag nanoparticles was immersed in a oxidizing HF/H_2O_2 solution. The Ag particles were found to exhibit highly directed, autonomous motion, etching through the Si to form Si nanowire arrays. The directed motion of the Ag particles is thought to occur via an electokinetic mechanism with

reduction of H_2O_2 to water occurs at the side of the particle facing the etching solution and oxidation of Si to H_2SiF_6 occurs on the opposite pole of the particle. Like the Pt-Au system the concomitant H^+ flux in the surrounding medium drives the motion of the Ag particles through the Si wafer, in a highly directed manner, Figure **1-8** (from reference 50).

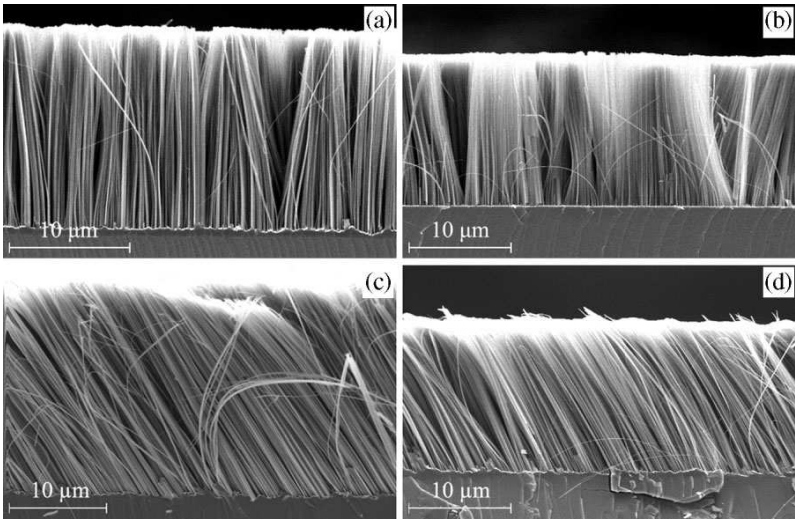

Figure **1-8** (from reference 50): Cross-sectional SEM images of Ag particle-coated Si wafers after etching in aqueous HF/H_2O_2 solution for 30 min showing aligned Si nanowire arrays produced on: a) p-type 7–14 Ω cm Si(100) wafer; b) p-type 5×10^{-3} Ω cm Si(111) wafer; c) p-type 4–7 Ω cm Si(110) wafer; and d) n-type 4–7 Ω cm Si(113) wafer.

1.4.4 Biommetic Behaviour of Micromotors

The reports described thus far the focus has been design of micromotors, control over motion and demonstrating some basic applications. The most exciting results of late have been from reports describing biommetic behaviour of catalytic micromotors. Sen et al. reported the chemotaxis of Pt-Au rods in a gradient of H_2O_2.[50] Much like food seeking microbes, the motors were observed to move up gradients of fuel concentrations. In

another report, Sen et al reported the phototaxis of Ag coated microspheres (2 μm in diameter).[51] The half Ag-coated colloids, in a gradient of UV light exhibit negative phototaxis i.e., movement toward regions of lower light intensity. In the presence of UV light and H_2O_2, Ag^+ and OOH^- ions are generated. The phototactic response was attributed to self-diffusiophoresis of the colloids. A macroscopic ion gradient is created in the presence of UV light, from which the particle move away from forming a region of gradually depleting colloid density. The same set of particles was observed to move back into the depleted zones due the thermal gradient formed. The interplay between these mechanisms adds to the complexity of the system, evident from the life-like behavior when watched for long periods of time.

In another report, predator-prey like behavior of AgCl microparticles and silica microspheres was reported.[52] When the two kinds of particles were mixed, the silica microspheres were seen to actively seek out the AgCl particles under UV illumination resulting in the Ag particles being engulfed by the silica, Figure **1-9** (from reference 53). This was attributed to the photo-decomposition of AgCl and the release of ions into the solution which caused electrophoretic and electroosmotic flows around the AgCl particles to which the silica tracers respond to. Similar effects were observed when photoactive TiO_2 particles reversibly repel or attract other colloids under UV illumination.

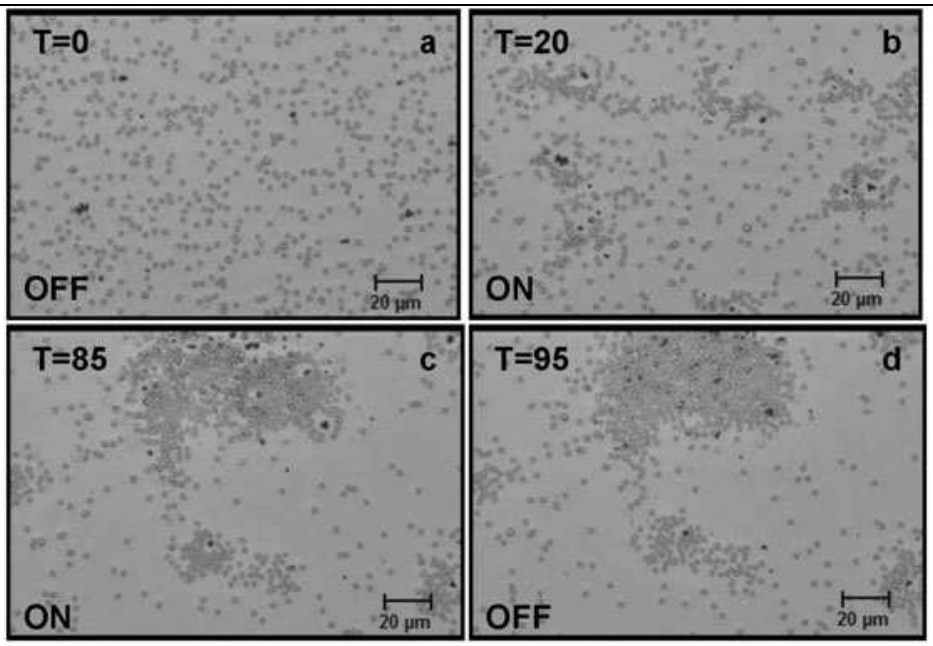

Figure **1-9** (from reference 53): Predator–prey behavior of two different particles. AgCl particles (darker objects) have been mixed with 2.34 µm silica spheres and placed in deionized water (a). When illuminated with UV light (b and c) the silica spheres actively seek out the AgCl particles and surround them. While the UV light is on, an exclusion zone is seen around the AgCl particles; this exclusion zone disappears when the UV light is turned off (d). Times in seconds are listed in the upper left hand corner. Status of the UV light is listed in the bottom left.

1.4.5 Designing Enzyme Based Micromotors

Nearly all the systems described above deal with noble metal catalysts so the next step was to explore other means to initiate motion. In the fifth chapter, the design of enzyme powered motors is discussed. Enzymes catalyze a wide range of reactions and are highly efficient catalysts. Since catalytic micromotor function is intimately connected to the activity of the catalyst, the use of enzymes would in the design faster and more powerful motors. Polystyrene spheres were asymmetrically functionalized with the enzyme catalase. Catalase catalyzes the decomposition of H_2O_2 to O_2 and H_2O. Unlike

the bipolar decomposition in the metallic Pt-Au system, a single site of catalase converts H_2O_2 to products H_2O and O_2. Attempts at powering microscale objects using this enzymatic reaction were unsuccessful, likely due to poor activity of immobilized catalase. However, this project needs to be explored further as the route for peroxide decomposition by catalase is fundamentally different from the noble metal catalytic system. The use of catalase and other enzymatic systems would open up opportunities for design of motors powered by new reactions and mechanisms. Some ideas for future directions for the micromotors project are briefly discussed in the final chapter.

The work discussed in this thesis deals with mechanistic aspects of catalytic micromotor motion and applications for the same. This work has added to the tool box of existing micromotor functions and has implications for design of future motors.

1.5 References

(1) Kamat, P. V. *J. Phys. Chem. B* **2002**, *106*, 7729-7744.
(2) Smith, A. M.; Nie, S. *Acc. Chem. Res.* **2009**.
(3) Parak, W. J.; Gerion, D.; Pellegrino, T.; Zanchet, D.; Micheel, C.; Williams, S. C.; Boudreau, R.; Gros, M. A. L.; Larabell, C. A.; Alivisatos, A. P. *Nanotechnol.* **2003**, R15.
(4) Katz, E.; Willner, I.; Wang, J. *Electroanal.* **2004**, *16*, 19-44.
(5) Schmidt, J. J.; Montemagno, C. D. *Annu. Rev. Mater. Res* **2004**, *34*, 315-337.
(6) Soong, R. K.; Bachand, G. D.; Neves, H. P.; Olkhovets, A. G.; Craighead, H. G.; Montemagno, C. D. *Science* **2000**, *290*, 1555-1558.
(7) T.M.Thorsen. *Science* **2002**, *298*.
(8) Went, F. W. *Am. Sci.* **1968**, *56*, 400-413.
(9) Purcell, E. M. *Am. J. Phys.* **1976**, *45*, 3-11.
(10) Happell, J.; Brenner, H. *Low Reynolds Number Hydrodynamics*; Prentice Hall: Englewood Cliffs, NJ, 1965.
(11) Lee, J.; Kim, C.-J. *Proc. IEEE MEMS Workshop* **1998**, *1998*, 538-543.
(12) Einstein, A. *Investigations on the Theory of Brownian Movement*; Dover Publications Inc: New York, 1956.

(13) Á. V. Delgado, e. *Interfacial Electrokinetics and Electrophoresis*; Marcel Dekker: New York, 2002.
(14) Watarai, H.; Suwa, M.; Iiguni, Y. *Anal. Bioanal. Chem* **2004**, *378*, 1693-1699.
(15) Vickrey, T. M.; Garcia-Ramirez, J. A. *Separ. Sci. Technol* **1980**, *15*, 1297-1304.
(16) Keh, H. J.; Wei, Y. K. *Coll. Polym. Sci.* **2000**, *270*, 539-546.
(17) Anderson, J. L. *Ann. Rev. Fluid Mech.* **1989**, *21*, 61-99.
(18) Block, S. M. *Nature* **1992**, *360*, 493-495.
(19) Agarwal, R.; Ladavac, K.; Roichman, Y.; Yu, G.; Lieber, C. M.; Grier, D. G. *Opt. Express* **2005**, *13*, 8906- 8912.
(20) Wang, J. *ACS Nano* **2009**, *3*, 4-9.
(21) Mano, N.; Heller, A. *J. Am. Chem. Soc.* **2005**, *127*, 11574-11575.
(22) Ismagilov, R. F.; Schwartz, A.; Bowden, N.; Whitesides, G. M. *Angew. Chem., Int. Ed.* **2002**, *41*, 652.
(23) Paxton, W. F.; Kistler, K. C.; Olmeda, C. C.; Sen, A.; St. Angelo, S. K.; Cao, Y.; Mallouk, T. E.; Lammert, P. E.; Crespi, V. H. *J. Am. Chem. Soc.* **2004**, *126*, 13424.
(24) Watanabe, N.; Kutsumi, K.; Sano, O. *J. Phys. Soc. Jpn* **1994**, *63*, 2955-2963.
(25) Raleigh, L. *Proc.R. Soc.London* **1890**, *47*, 364.
(26) Tetsu Mitsumata; Ikeda, K.; Gong, J. P.; Osada, Y. *Appl. Phys. Lett.* **1998**, *73*, 2366-2368.
(27) Toyota, T.; Maru, N.; Hanczyc, M. M.; Ikegami, T.; Sugawara, T. *J. Am. Chem. Soc.* **2009**, *131*, 5012-5013.
(28) Stock, C.; Heureux, N.; Browne, W. R.; Feringa, B. L. *Chem. Eur. J.* **2008**, *14*, 3146-3153.
(29) Pantarotto, D.; Browne, W. R.; Feringa, B. L. *Chem. Commun.* **2008**, 1533-1535.
(30) Solovev, A. A.; Mei, Y.; Ureña, E. B.; Huang, G.; Schmidt, O. G. *Small* **2009**, *5*, 1688-1692.
(31) Agrawal, A.; Dey, K. K.; Paul, A.; Basu, S.; Chattopadhyay, A. *J. Phys. Chem. C* **2008**, *112*, 2797-2801.
(32) Ghosh, A.; Fischer, P. *Nano Lett.* **2009**, *9*, 2243-2245.
(33) Garstecki, P.; Tierno, P.; Weibel, D. B.; Sagues, F.; Whitesides, G. M. *J. Phys.: Cond. Matt.* **2009**, 204110.
(34) Lauga, E.; Powers, T. R. *Rep. Prog. Phys.* **2009**, *72*, 096601.
(35) Laocharoensuk, R.; Burdick, J.; Wang, J. *ACS Nano* **2008**, *2*, 1069-1075.
(36) Demirok, U. K.; Laocharoensuk, R.; Manesh, K. M.; Wang, J. *Angew. Chem., Int. Ed.* **2008**, *47*, 9349-9351.
(37) Kline, T. R.; Paxton, W. F.; Mallouk, T. E.; Sen, A. *Angew. Chem. Int. Ed.* **2005**, *44*, 744.
(38) He, Y.; Wu, J.; Zhao, Y. *Nano Lett.* **2007**, *7*, 1369-1375.
(39) Gibbs, J. G.; Zhao, Y.-P. *Small* **2009**, *5*, 2304-2308.
(40) Catchmark, J. M.; Subramanian, S.; Sen, A. *Small* **2005**, *1*, 202-206.
(41) Qin, L.; Banholzer, M. J.; Xu, X.; Huang, L.; Mirkin, C. A. *J. Am. Chem. Soc.* **2007**, *129*, 14870-14871.
(42) Wang, Y.; Fei, S.-t.; Byun, Y.-M.; Lammert, P. E.; Crespi, V. H.; Sen, A.; Mallouk, T. E. *J. Am. Chem. Soc.* **2009**, *131*, 9926-9927.

(43) Balasubramanian, S.; Kagan, D.; Manesh, K. M.; Calvo-Marzal, P.; Flechsig, G.-U.; Wang, J. *Small* **2009**, *5*, 1569-1574.
(44) Calvo-Marzal, P.; Manesh, K. M.; Kagan, D.; Balasubramanian, S.; Cardona, M.; Flechsig, G.-U.; Posner, J.; Wang, J. *Chem. Commun.* **2009**, 4509-4511.
(45) Sundararajan, S.; Lammert, P. E.; Zudans, A. W.; Crespi, V. H.; Sen, A. *Nano Lett.* **2008**, *8*, 1271.
(46) Burdick, J.; Laocharoensuk, R.; Wheat, P. M.; Posner, J. D.; Wang, J. *J. Am. Chem. Soc.* **2008**, *130*, 8164.
(47) Sundararajan, S.; Sengupta, S.; Ibele, M.; Sen, A.,*Unpublished.* **2010**.
(48) Kagan, D.; Calvo-Marzal, P.; Balasubramanian, S.; Sattayasamitsathit, S.; Manesh, K. M.; Flechsig, G.-U.; Wang, J. *J. Am. Chem. Soc.* **2009**, *131*, 12082-12083.
(49) Peng, K.; Lu, A.; Zhang, R.; Lee, S.-T. *Adv. Funct. Mater.* **2008**, *18*, 3026-3035.
(50) Hong, Y.; Blackman, N. M. K.; Kopp, N. D.; Sen, A.; Velegol, D. *Phys. Rev. Lett.* **2007**, *99*, 178103(178101).
(51) Hong, Y.; Velegol, D.; Chaturvedi, N.; Sen, A. *Phys. Chem. Chem. Phys.* **2010**, *12*, 1423-1435.
(52) Ibele, M.; Mallouk, T. E.; Sen, A. *Angew. Chem. Int. Ed.* **2009**, *48*, 3308-3312.

Chapter 2

Electrokinetic Mechanism of Motility in Pt-Au Motors

2.1 Introduction

The first report of artificial motor powered by a catalytic reaction was devised by Whitesides and co-workers.[1] In their system, a Pt disk was placed asymmetrically on a millimeter sized PDMS 'boat'. When the set-up was placed in an aqueous H_2O_2 solution, it propelled itself on the air-water interface at speeds of a few centimeters per second. Platinum metal catalyzes the decomposition of the peroxide fuel to water and oxygen gas, Equation **2.1** .Due to the asymmetric placement of the Pt catalyst, the jet of oxygen gas released on end of the boat propelled the PDMS boat.

$$\mathbf{2H_2O_2\,(aq) \xrightarrow{Pt(s)} 2H_2O(l) + O_2(g)} \qquad (\mathbf{2.1})$$

Walter Paxton in the Sen group devised a microscale catalytic motor. The motor consisted of bimetallic Pt-Au rods (2 μm in length and 360 nm diameter), that exhibited autonomous motion when placed in hydrogen peroxide solutions.[2] When observed through an optical microscope, the rods moved at average speeds of 10 μm/s. It was hypothesized that a bubble propulsion mechanism, much like the millimeter sized PDMS/Pt motors, would be in operation in the microscale Pt-Au system. Hence, the motor propulsion was expected to occur with the Au leading due to the jet of O_2 gas emanating from the Pt end. However, upon closer inspection, the rods were observed to

move Pt end forward, ruling out the possibility of bubble propulsion based mechanism. Moreover, nucleation of O_2 bubbles was not seen to occur on the rod surface, unlike the PDMS/Pt system, where motility of the PDMS boat was directly correlated to bubble bursting at the Pt disk. In the Pt-Au system, bubbles were observed to nucleate in the surrounding media instead. These observations suggested that other mechanism/s were at play in the microscale Pt-Au system.

Several mechanisms have been considered for the motility of the Pt-Au motors. Initially Paxton et al. proposed an interfacial tension model.[2] According to this model, the hydrophobic nature of Au surface propels the rod toward the oxygen rich environment, resulting in rod motion, Pt end forward. Later, Dhar et al. proposed a Brownian ratchet mechanism in which the oxygen evolution at the Pt end lowers the viscosity, allowing thermal motion to drive the motor Pt end forward.[3]

A third possibility, a self-electrophoresis model (also referred to as bipolar electrochemical mechanism), for rod motility was considered when a current between bulk Pt and Au was observed in H_2O_2 solutions. Unlike the interfacial surface tension model or the Brownian ratchet model, which consider decomposition of H_2O_2 at the Pt end alone, the self-electrophoresis model assigns a more active role to the Au end. The crux of the self-electrophoresis model is the bipolar decomposition of the H_2O_2 fuel.

Equation 2.1 represents the overall reaction of H_2O_2 decomposition. The reaction has a large driving force of 212 kJ/mol O_2 Reactions **2.2** and **2.3** are the oxidation and reduction halves of the reaction, respectively. The standard potentials of reactions **2.2** and **2.3** are 0.15 and 1.21 V with respect to Ag/AgCl electrode (3M NaCl), respectively.

$$\textbf{Oxidation: } H_2O_2(aq) \rightarrow O_2(g) + 2H^+(aq) + 2e^- \quad (2.2)$$

$$\textbf{Reduction : } H_2O_2(aq) + 2H^+(aq) + 2e^- \rightarrow 2H_2O(l) \quad (2.3)$$

According to the self-electrophoresis hypothesis, the decomposition of H_2O_2 fuel occurs at both metals, Figure **2-1**. Oxidation of H_2O_2 to O_2 occurs at the Pt anode and reduction to H_2O occurs at the Au cathode. As the reactant is continually converted to products, an electrical current is established in the bimetallic rod. To maintain the charge balance, positive ions, predominantly protons, migrate from Pt end to gold end in the fluid outside. The migrating ions carry along with them water molecules, resulting in an electroosmotic flow from Pt to Au. By Galilean invariance, the motion of the fluid from Pt to Au is the equivalent to rod propulsion in the opposite direction, i.e. Pt end forward.

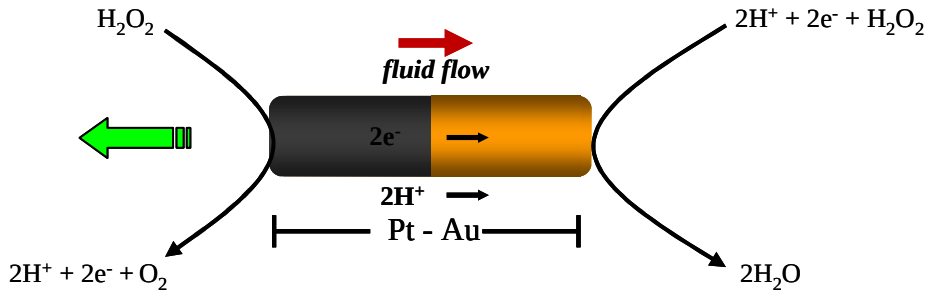

Figure **2-1**: Self-electrophoresis of Pt-Au motors resulting form bipolar decomposition of H_2O_2 at the Pt and Au ends. At the Pt (anode), H_2O_2 is converted to O_2 and at the Au (cathode), H_2O_2 is reduced to H_2O. As the reaction proceeds, the electrical current within the Pt-Au motor is balanced by flow of protons from Pt to Au in the surrounding fluid, resulting in motor propulsion in the opposite direction, i.e., Pt end forward.

Several approaches have been adopted to confirm the self-electrophoresis hypothesis. Kline et al. proved that the bipolar H_2O_2 decomposition was indeed a major contributing factor to Pt-Au motor motility.[4] In their setup, the authors patterned Ag disks on a Si wafer coated with Au. Instead of catalytic motor moving through fluid, in this system, the catalyst was immobilized and electroosmotic flow was observed using colloidal tracers. The colloidal tracers were observed to form patterns as a result of fluid pumping resulting from the bipolar decomposition of H_2O_2. The pattern formation did not occur when an insulator was placed in between the two metals indicating that electrical contact between the two metals was necessary for the observation for fluid pumping. Paxton et al. adopted a method wherein an inter-digitated array of Au and Pt electrode fingers separated by borosilicate glass, was used.[5] In this system colloidal tracer motion in the presence of H_2O_2 was observed only when the fingers were in electrical contact. In a setup similar to that used by Kline et al., Subramanian et al. showed that electroosmotic flow patterns could be altered by tailoring the surface charge of the immobilized metals.[6]

Wang et al. validated the mechanism by using different combinations of bimetallic rods.[7] Nobel metal rods such as Ni-Ru, Au-Pd, Au-Ru and Rh-Pt were synthesized. From Tafel plots of anodic and cathodic hydrogen peroxide reactions at various metal (Au, Pt, Rh, Ni, Ru, and Pd) ultra microelectrodes, mixed potentials at which the anodic and cathodic reaction rates are equal for each metal were determined. In each pair one metal takes over the oxidation half of the H_2O_2 decomposition while the other metal takes over the reduction half of the reaction depending on the relative mixed potential values for each metal pair. Metals higher up in the series, i.e. those with lower mixed potential values catalyzed the anodic reaction whereas those lower down in the

series catalysed the cathodic reaction. The propensity of the metal to act as the anode or cathode was correlated to the direction of rod motion. For e.g., in the case of Pt-Au rods, Pt act as the anode resulting in Pt-Au motors moving Pt end forward. However in the case of Au-Ru rods, Au acts as the anode, resulting in rods moving Au end forward.

In this chapter, the Pt-Au bimetallic pair system was used to validate the mechanism.† Two strategies that were explored to demonstrate that the self-electrophoresis mechanism is predominantly responsible for motility of Pt-Au rods, are discussed. In the first approach, a poor conductor (PPy) was placed between Pt and Au to shut -off the electrical current. To begin with, the PPy used had low conductivity but Pt-PPy-Au rods were observed to exhibit motility. Increasing PPy resistivity did not have a significant effect in rod speeds; hence, an alternative approach was adopted where the surface charge of the particle was altered.

2.2 Placing a Poor Conductor Between Pt and Au Segments

Figure **2-1** depicts the self-electrophoresis propulsion mechanism proposed for the Pt-Au/H_2O_2 system.[8] The Pt-Au rod propulsion occurs as a result of the self-generated electric field produced as reactants are converted to procucts. The electrical current setup in the rod as a result of H_2O_2 decomposition is accompanied by a concommitant proton flux from Pt to Au, propelling the particle Pt end forward. The first approach to

† It should be noted that all these above-mentioned strategies for verifying the mechanism were adopted, as the problem was being approached from different perspectives by the Sen, Mallouk, and Catchmark groups. Several of these experiments were carried out in parallel and results from one approach helped in designing experiments for other approaches and vice versa.

validating the electrokinetic mechanism in the case of Pt-Au rod system was to place a poor conductor between the two metals. In the self-electrophoresis model for Pt-Au motor propulsion, disrupting the electron flow should hinder the fluid flow leading to decreased motor speeds.

2.2.1 Polypyrrole as Choice of Material for Insulating Layer

Polypyrrole (PPy), a conducting polymer, was chosen as the material for the insulating segment between the Pt and Au segments for a couple of reasons. Firstly, synthesis of PPy rod segments is amenable to template based synthesis. Martin and coworkers had reported the synthesis of PPy wires via template synthesis and later the Mallouk and Mirkin groups reported the synthesis of wires containing metallic and PPy segments.[9-132] Secondly, PPy is a conducting polymer whose conductivity can be tuned. The conductivity of the material can be tuned from 10^{4} S cm^{-1} (conductor) to 10^{-12} S cm^{-1} (insulator).[13] Once synthesized, the conductivity of the polymer could be reduced by chemical or electrochemical methods.

Figure **2-2** shows the oxidation of the pyrrole monomer to polypyrrole and conducting and overoxidized, less conducting (OPPy) forms of the polymer.[14] PPy is synthesized by applying an oxidation potential to a solution of the monomer Py (Figure **2.2 A**) in the presence of a supporting electrolyte. The oxidation of the pyrrole monomer E_{ox} begins at 0.57 V vs. Ag/AgCl reference. Polymerization occurs at the 2 and 5 positions on the pyrrole ring.[14] The electropolymerization reaction is initiated by the generation of a radical cations of the Py monomer followed by rapid growth of the chain.

The non-conjugated polymer thus obtained becomes conjugated on oxidation at the electrode, Figures **2.2 B** and **C**. If the polymer is further oxidized, either by chemical or electrochemical means, the backbone of the polymer is chemically modified, disrupting the conjugation and therby reducing the conductance of the polymer chain, Figure **2.2 D**. The oxidation potential of the polymer is lower than that of the monomer, therefore the simultaneous oxidation of the PPy once formed during Py oxidation is unavoidable.

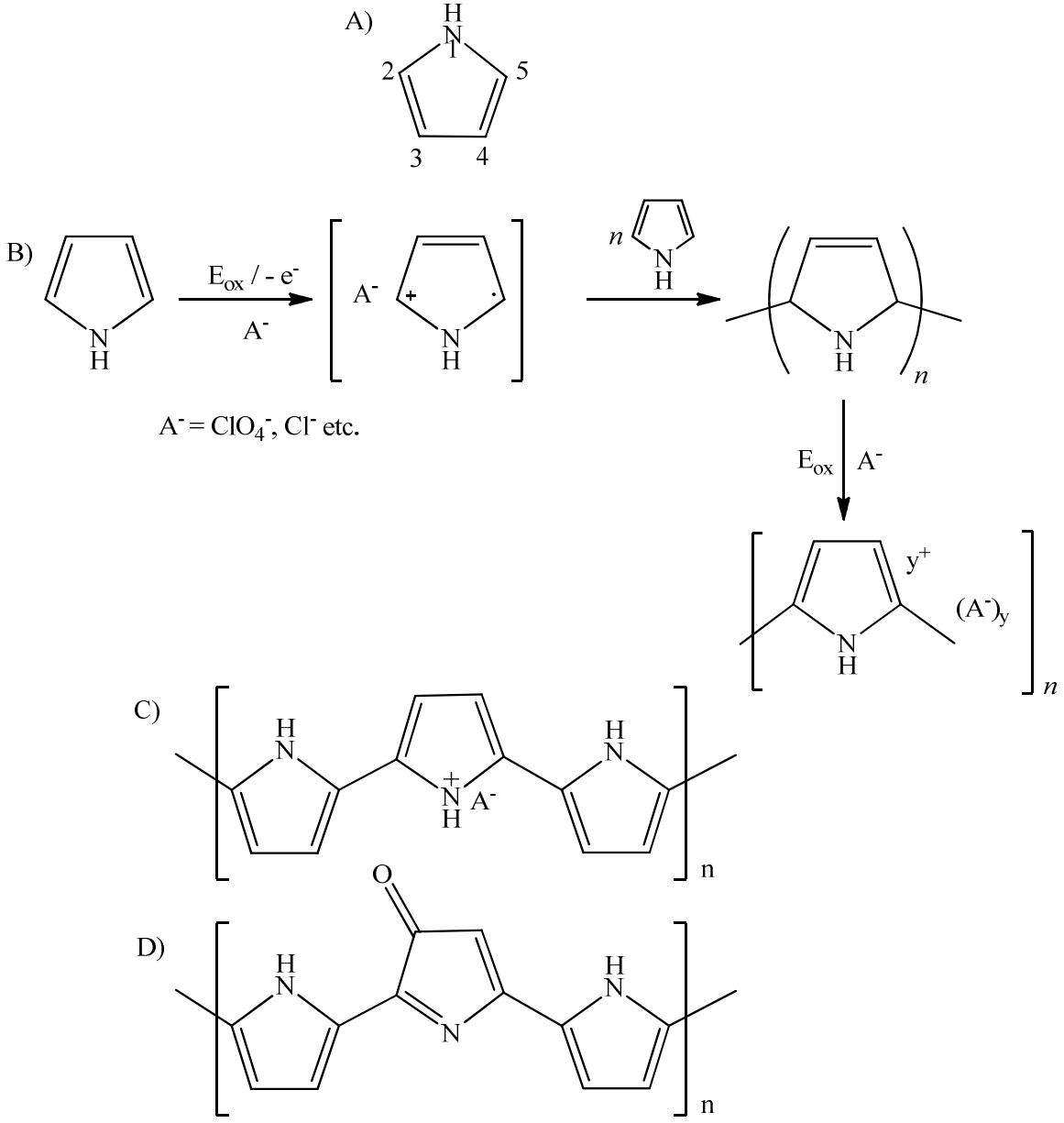

Figure **2-2**: **A)** Pyrrole monomer, **B)** Mechanism for Py monomer electropolymerization to yield PPy, **C)** Conducting form of Polypyrrole (PPy) and **D)** Overoxidized PPy. The perfectly altering conjugating ions disrupted by over-oxidation, resulting in a polymer of lower conductivity.

2.2.2 Synthesis of Pt-PPy-Au Rods

Pt-PPy-Au rods were prepared by electrodepositing in the pores of alumina membranes.[2] All metal plating solutions were purchased from Technic Inc and, metal deposition steps were carried out galvanostatically. A sacrificial silver layer (-5mA, 50 minutes) was deposited to block the branched portion of the alumina membrane (Whatman), followed by gold deposition (-1.25 mA, 20 minutes). The pyrrole monomer (Sigma) was purified by distillation prior to the electropolymerization step. The PPy was deposited by electrochemical oxidation of aqueous 0.5 M pyrrole solution in the presence of 0.5 M $LiClO_4$ (Sigma) by cycling the potential between 0.6 and 0.85 V vs. an Ag/AgCl reference electrode at 20 mV/s.[11] It may be noted that the PPy deposition was carried out in aqueous media and at E_{ox} greater than 0.57 V. In these experimental conditions the overoxidation of the PPy formed is unavoidable. Hence the PPy in the rods prior to any treatment to lower conductivity, was expected to be a poor conductor and the polymer structure at this stage is shown in Figure **2-2 D**. The lowered conductivity of the PPy was even desirable as the objective of the experiment was to insert a poor conductor between the Pt and Au segments. The hypothesis was that the poor conductor would hinder electron flow and thereby reduce observed rod speeds. The PPy deposited, was however found to be sufficiently conducting to enable electrodeposition of the subsequent Pt layer (-1.75 mA, 30 minutes). The sacrificial silver layer was dissolved in 20% v/v nitric acid followed by the template dissolution in 0.2 M KOH for 40 minutes.

All electrodeposition steps were carried out using a potentiostat (Pine model AFRED5). The lengths of the Pt and Au segments were approximately 1.2 µm each in Pt-Au and the PPy segments were 1.5 µm. The diameter of the rods is approximately 370 nm. Lengths were characterized by transmission electron microscopy (JEOL 1200 EXII),

and dark-field optical microscopy (Zeiss Axiovert 200 reflectance/transmission). Figure **2-3** shows a section of a TEM of a Pt-PPy-Au rod and Figure **2-4** shows optical microscopy image of the rod.

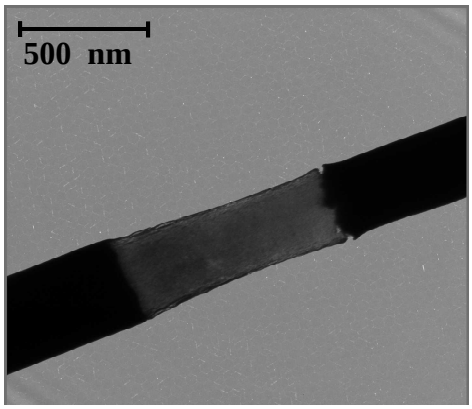

Figure **2-3**: TEM image showing a section of Pt-PPy-Au rod. The Pt-PPy and Au-PPy junctions are indicated in the image. In many rods like the one above, the Au-PPy junction was found to be discontinuous. This observation is analogous to the poor adherence of bulk PPy films when deposited on bulk Au surfaces. Unlike metallic rods that are centrifuged and re-suspended via sonication, gentler techniques such as vortexing were used to re-suspend Pt-PPy-Au rods to prevent the breakage of the rods. Pt-PPy-Au rods were observed to move at speeds comparable to that of Pt-Au rods (5-10 µm/s) indicating that the flow of electronic current across the Au-PPy interface occurred in spite of the irregularity in the junction.

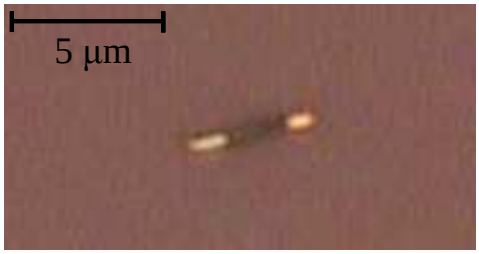

Figure **2-4**: Optical microscopy image of a Pt-PPy-Au rod.

2.2.3 Motility of Rods Before and After PPy Chemical Overoxidation

Pt-PPy-Au motor motility experiments were performed by mixing a dilute solution of the rods in deionized water and an aqueous 5% v/v H_2O_2 solution. 30 µL of that solution was placed in a well created by a silicone spacer on a glass slide. A cover slip was placed on top. Rod motility was observed using optical microscope and video clips of rod motility were captured with the help of a camera attached to the microscope. Rod speeds were quantified by analysing the videos using home made MATLAB based particle tracking software.

Pt-Au rods move at average speeds of 5 to 10 µm/s. Due to the overoxidized nature of the as synthesized PPy, the speeds of Pt-PPy-Au rods even prior to any treatment to lower PPy conductivity was expected to be lower but this was not found to be the case in our experiments. The average speed of nearly 30 rods before PPy overoxidation was found to be 6.9 ± 0.6 µm/s indicating that in spite of the poor quality of the PPy formed it was not insulating enough to suspend electron flow between the Pt and Au segments.‡ We therefore sought to further lower the conductivity of the PPy. Chemical overoxidation of the PPy segment of Pt-PPy-Au rods was carried out by treating the rods in solution of 0.5 M KOH for 6 hours in the presence of 0.1M $FeCl_3$ solution.[15] The rods were subsequently rinsed thoroughly in deionized water. The speed post oxidation was found to be 6.4 ± 0.9 µm. The overoxidation experiment did not show any major changes in the rod motility. Simultaneously, single rod conductivity was

‡ This was not entirely unexpected as the PPy segment was found to conducting enough to facilitate electrodeposition of the subsequent Pt layer.

measured to coorelate any observable changes in speed, to the decrease in the conductivity of the PPy segment, resulting from chemical overoxidation of PPy.

2.2.4 Conductivity of Pt-PPy-Au Rods

The Mayer group at Penn State reported electrofluidic assembly of single nanorods for measurment of metallic nanorods.[16] Figure **2-5** shows a side view of the electrofluidic assembly setup. The alignment of the rods between the electrode fingers occurs in AC electric fields as the metallic rods polarize easily. As a result they experience a dielectrophoretic force that produces net movement in the direction of increasing field strength, which occurs at the high aspect ratio features, the electrode fingers. As the nanowires approach the electrodes with spacing approximately equal to the length of the nanowires, the electric field strength between the electrodes and nano-wire tips increases proportionally to the inverse of the distance from the electrodes, resulting in rod assembly between the spacing.

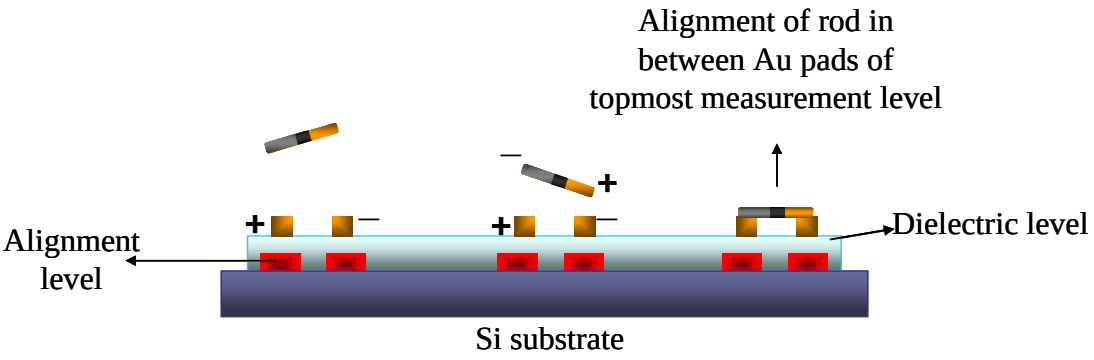

Figure **2-5**: Schematic of the setup used for electrofluidic alignment of Pt-PPy-Au rods. The device allows for the alignment of microsized rods for resistance measurements and is comprised of three layers: the bottom-most alignment level, the topmost measurement level and the intermediate dielectric level. A suspension of the rods in isopropyl alcohol is

placed on the device and an AC current is applied to the alignment layer. The electric field propagated through to the topmost measurement layer. Rods in solution get polarized and align on the pads of the measurement level. Contact is made on the measurement level using a micromanipulator and desired voltage is applied and I-V response of each individual rod is obtained, enabling calculation of the resistivity of the rod.

Mask designs were obtained form the Mayer group and the device was fabricated with some modifications to the procedure followed by the Mayer group.[16] The procedure followed is described briefly below: A p-type Si wafer with a 1 µm thick oxide layer (SQI international) was used as the substrate. The alignment layer was fabricated using a lift-off method. First, a lift-off resist (LOR 5A) was applied to the wafer by spinning at 3000 rpm for 45 seconds and baked for 10 minutes at 180°C. Then a positive resist (SPR 3013, Shipley) was spin coated on the wafer at 4000 rpm for 40 seconds. The wafer was then baked at 100 °C for 1 minute.

Contact lithography was used to transfer the mask pattern of the alignment level (i.e., bottom most layer) on to the wafer. The UV exposure was performed using a mask aligner (Karl Suss MA6). The exposure was done in contact mode for 4 seconds. A post exposure bake step was at 100 °C for 1 minute. Subsequently the wafer was placed in a developing solution (tetramethyl ammonium hydroxide, Rohm and Haas CD26) for 2-5 minutes. The UV exposed areas were removed allowing for metal deposition in those areas. A 15 nm Cr adhesion layer was evaporated followed by Au deposition of 80 nm. Finally the wafer was placed in acetone and sonicated gently to remove the undeveloped photoresist, to leave behind the desired metal pattern of the alignment layer.

In the next step the interlayer dielectric was deposited. The original procedure called for fabrication of a silicon nitride layer, but in this case it was modified to use spin on glass (SOG) instead. SOG (300F, Filmtronics) was spun on the wafer from the previous step at 3000 rpm for 45 s. The wafer was baked at 425°C for 1 hour and allowed to cool to room temperature. The top contact layer was fabricated in a manner similar to the bottom layer, using the mask for the measurement level. Finally, to enable contact to the bottom most, alignment layer, reactive ion etch (RIE) step was performed to remove the dielectric in regions where contact was required.

Figure **2-6** shows an optical microscopy image of a single Pt-PPy-Au rod between Au pads of the topmost layer. A suspension of the rods in isopropyl alcohol was prepared and a drop of the suspension is placed on the device. An AC field (10V @ 1 kHz) was applied to align the rods in between the topmost layer i.e., the measurement layer. Contact was made to the measurement layer and conductivity of the PPy segment is obtained.

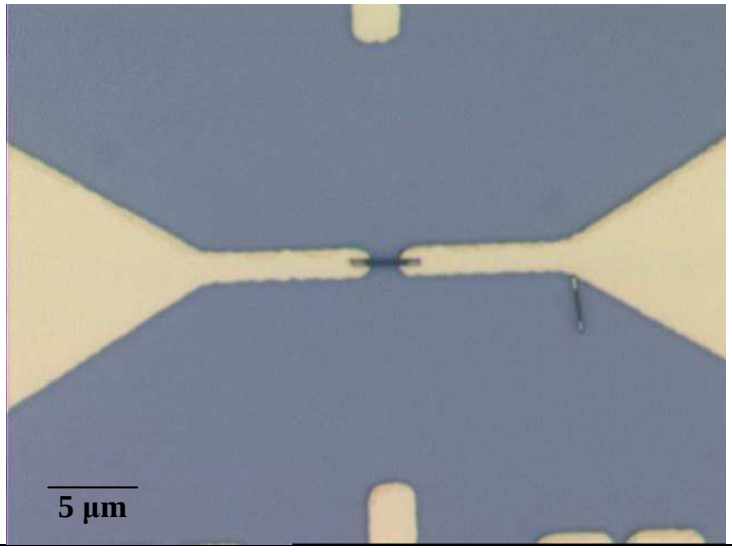

Figure **2-6**: Optical microscopy image of electro fluidic alignment of Pt-PPy-Au rods between the Au pads of the measurement level. An AC field of 10 V @ 1kHz was applied to a suspension of Pt-PPy-Au rods in isopropyl alcohol. Contact is made on the Au pads in order to measure conductivity of the PPy segment.

While the original procedure called for silicon nitride dielectric layer, in these experiments it was substituted with spin on glass layer. This was unavoidable due to non-availability of silicon nitride deposition tool at the time of performing these experiments. The device fabricated was prone to frequent contact failures most, likely due to the failure in dielectric layer. Hence, it was not possible to acquire a large sample size of rod conductivity data pre- and post-chemical overoxidation treatment. However the data obtained (conductivity data for 5 rods or fewer in each case) indicated a decrease in the conductivity by nearly an order of magnitude. The conductivity of the rods pre-chemical overoxidation ($FeCl_3$, KOH treatment) was 10^{-1} S cm^{-1} and it decreased to 10^{-2} S cm^{-1}, post-chemical overoxidation. The conductivity of the pre-chemical overoxidation rods was low to begin with. As noted earlier, this may be attributed to the electroploymerization conditions (aqueous media and unavoidable overoxidation of the polymer) used in our experiment. While the use of aqueous conditions could have been bypassed by using acetonitrile as solvent of choice, we hypothesized that the insertion of a poor conductor in itself should affect the rod motility. Therefore, PPy electropolymerization conditions were chosen such that the PPy formed would be a poor conductor. When this hypothesis was proved incorrect, the chemical overoxidation route was chosen to further decrease the conductivity of the PPy segment, and allow for comparisons to be made between pre and post-chemical overoxidation experiments for

rod motility. This decrease in conductivity was insufficient to cause an appreciable decrease in the rod speeds (6.9 ± 0.6 μm/s to 6.4 ± 0.9 μm/s). Additionally the frequent failure of the device due to defects in the dielectric layer made this approach non-viable. Therefore an alternate approach was chosen to investigate the problem, and is described in the following section.

2.3 Zeta Potential Reversal Approach

In the electrokinetic model of Pt-Au rod motility, motion is predicted to be Pt end forward. The half reactions are written in terms of proton flux surrounding a metallic Pt-Au particle that bears a negative zeta potential in the experimental conditions, equations **2.2** and **2.3**. Hence for a negatively charged particle, the double layer has a higher concentration of positively charged ions (in deionized water, the positively charged species being protons predominantly). If the surface properties of the particle were altered such that the metal particle bears a positive charge, the double layer would comprise of negatively charged species, predominantly hydroxyl ions in our experimental conditions. Rewriting the anodic (Equation **2.4)** and cathodic (Equation **2.5)** in terms of hydroxyl ions we get:

$$\textbf{Oxidation: } 2H_2O_2(aq) + 2OH^-(aq) \rightarrow O_2(g) + H_2O(l) + 2e^- \qquad (2.4)$$

$$\textbf{Reduction : } H_2O_2(aq) + 2e^- \rightarrow 2OH^-(aq) \qquad (2.5)$$

The standard potentials of reactions **2.4** and **2.5** are 0.146 V and -0.076 V with respect to standard hydrogen electrode, respectively. In a negatively charged particle, the flux of protons from the Pt to Au drives the motor Pt end forward, Figure **2-1**. For a positively charged particle, the ion flux due to hydroxyl ion migration, in the double layer is reversed. In this case, the hydroxyl ions migrate from Au end to Pt end, transporting the fluid in that direction. As a result, a positively charged particle should propel itself Au end forward Figure **2-7** . To test this hypothesis, the surface of Pt-Au rods was modified, to render them positively charged.

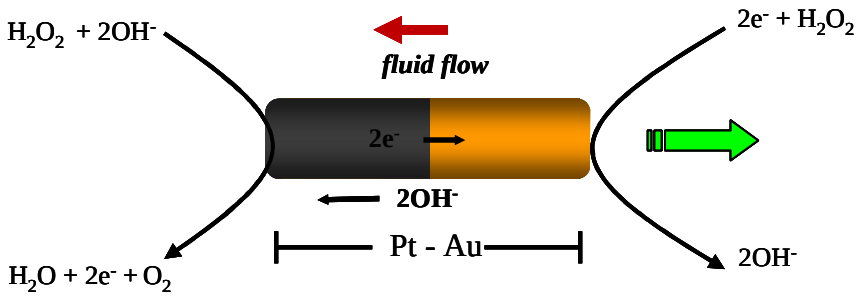

Figure **2-7**: For a positively charged Pt-Au motor, the double layer is comprised of negatively charged ions, mostly OH^- ions. We rewrite the half reactions in terms of OH^- ions. In this case, the hydroxyl ions produced at the Au end migrate to the Pt end, transporting the fluid in that direction. The (positively charged) motor itself moves in the opposite direction, with the Au end forward.

3.1 Synthesis of Positively Charged Pt-Au Rods

To render the Pt-Au motor surface positively charged, the surface sol-gel technique was used.[17] Using this technique, rods with SiO_2 shell were synthesised. SiO_2 coated Pt-Au rods are negatively charged due to the presence of surface OH^- groups.The

rods were silanized with an amine terminated silane to render them positive. The pK_a of the amine used, aminopropyl triethoxy silane is 10.6. In our experimental conditions, the pH of deionized water medium is 5.5 and hence the amine group remains protonated in these conditions, making the surface positively charged. The surface sol-gel technique for making silica coated metallic wires was adopted for making glass coated Pt-Au wires, Figure **2-8** shows a schematic of the process to make glass coated rods.[17] The alumina membrane with silver backing was dipped in $SiCl_4$ soution. The excess $SiCl_4$ was washed away using CCl_4 wash steps leaving only the $SiCl_4$ adhered to the walls of the alumina to remain. The surface adhered $SiCl_4$, was then hydrolyzed to give silica coated alumina membranes. Rods were released in phosphoric acid solutions overnight as silica dissolves in basic conditions. Zeta potential measurements (ZETAPALS, Brookhaven Instruments) of these rods revealed the charge to be: -30 mV. To render the rods positively charged, the rods were treated to an ethanolic (3-aminopropyl)-trimethoxysilane (APTMS) solution for 5 hours. The zeta potential of the APTMS treated rods was measured to be +20 mV. To prevent sticking of positively charged rods to the glass surface the latter was also functionalized with APTMS.

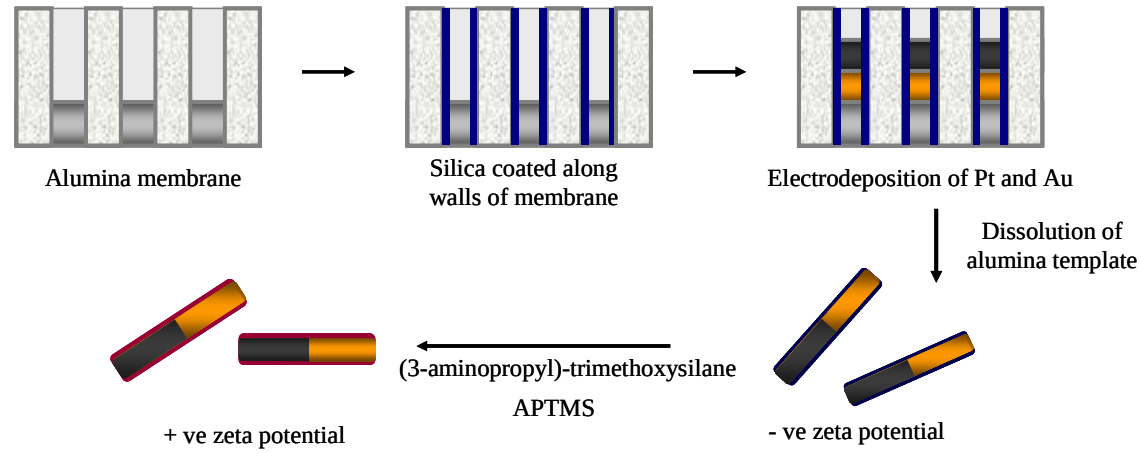

Figure **2-8**: Surface sol-gel technique for synthesis of glass coated Pt-Au rods. First, the walls of the alumina template are treated to multiple $SiCl_4/H_2O$ exposure cycles. Once a glass coating of desired thickness was obtained, electrodeposition of the Au and Pt segments was carried out. SiO_2 coated rods bear a negative surface charge and are further silanized with APTMS, and amine terminated silane that renders the rod surface positive.

Figure **2-9** shows TEM images of silica coated Pt-Au rods. The silica coating of 5 nm was obtained by performing 2 cycles of the surface sol-gel process. The porosity of 5 nm thick silica coatings allowed for diffusion of H_2O_2 fuel to the Pt surface as evidenced by the motility of the SiO_2-coated rods in H_2O_2 (7.2 ± 1.01 μm/s). Oxygen evolution experiments to determine the catalytic activity of the silica coated rods revealed a lowering in activity of these rods compared to bare Pt-Au rods. Paxton et al. reported oxygen evolution rates of nearly 9.74×10^{-17} mol O_2/sec per rod whereas in silica coated rods the rate dropped to 5.10×10^{-17} mol O_2/sec per rod.[18] The oxygen evolution rate of APTMS functionalized rod dropped still further to 2.77×10^{-17} mol O_2/sec per rod. Correlations between rod speeds and oxygen evolution rates were not made as it is not possible to separate the contribution of the chemical and electrochemical peroxide decomposition routes by O_2 evolution experiments.

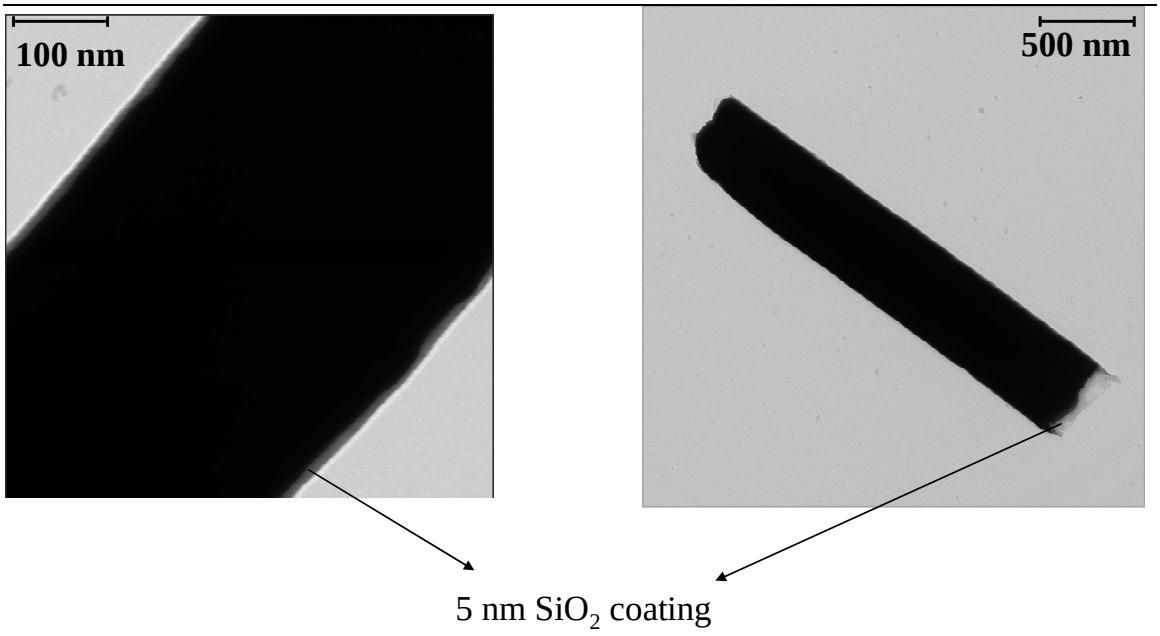

Figure **2-9**: TEM images of silica coated Pt-Au rods prepared by the surface sol-gel technique.

2.3.2 Rod Motility Experiments -.Validation of the Self-Electrophoresis Mechanism

The motility of silica coated rods and pre- and post-APTMS treatment was observed in 5% H_2O_2 solutions. Prior to the APTMS treatment the rods bear a negative zeta potential and thus, like Pt-Au rods, they were observed to move Pt end forward. Upon silanization with APTMS, the rods were rendered positively charged. These rods were seen to move Au end forward validating the self-electrophoresis model for motility in this system. Figure **2-10** shows screen capture images of a Pt-Au rod moving from the bottom of the screen to the top, over a span of 5 seconds, Au end forward.

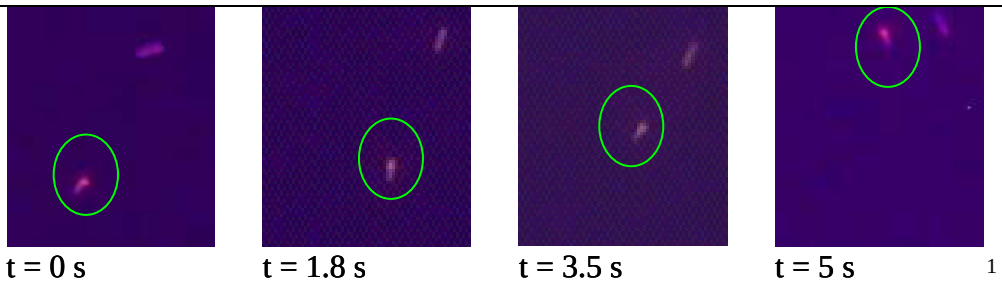

Figure **2-10**: Screen capture images of a Pt-Au rod moving from the bottom of the screen to the top over a span of 5 seconds, Au end forward. The rod of interest is circled for clarity.

2.4 Summary

In this chapter a couple of approaches were explored to validate the self-electrophoretic mechanism of motility in Pt-Au motors. The self-electrophoretic mechanism assigns a active role for both Pt and Au end of the motor in H_2O_2 decomposition. The Pt end acts as the anode converting H_2O_2 to O_2 gas and the Au end acts as the cathode by converting H_2O_2 to H_2O. In order to maintain charge balance, the electron current from Pt to Au inside the motor is balanced by a flux of protons in the fluid outside. Two approaches to validate the mechanism were tested. In the first approach Pt-PPy-Au rods were synthesised and the conductivity of the PPy was lowered by chemical treatment. The overoxidation of the PPy did reduce the conductivity of the PPy segment by an order of magnitude but an appreciable decrease in the rod speed was not observed.

Another approach for validating the self-electrophoresis mechanism was adopted. Negatively charged Pt Au rods move Pt end forward due to migration of solvated protons fro Pt to Au. Rewriting the half-reactions in terms of hydroxyl ions for a positively

charged particle, the fluid pumping occurs from Au to Pt, propelling the rods Au end forward. The surface solgel technique was used to make glass coated rods that were further silanized to yield positively charged Pt-Au rods. When placed in H_2O_2 solutions, the charge reversal of the rods (-ve to +ve) did indeed result in a direction reversal (Au end forward), validating the self-electrophoresis mechanism.

In retrospect, the fabrication of Pt-PPy-Au rods for controlling rod motility by altering the conductivity of the PPy segment would not have panned out as planned. This was because subsequent calculations performed by Walter Paxton to estimate the current density per rod, to propel a particle 10 μm/s was determined to be miniscule (on the order of 10^{-4} mA/cm^{-2}).[19] A superior insulator would be required to completely suspend rod motility. Also, Pt rods themselves show some degree of powered motion in H_2O_2 solutions, hence it may be challenging to stop rod motion completely. Even if one were to fabricate a rod with a perfect insulator between the Pt and Au segments, the insulator-Au segment would act as a dead weight that lowers rod speed due to added length of the latter segment, however it may not entirely suppress the non-Brownian motion due to the active Pt segment. While other mechanisms for Pt-Au motor motility cannot be completely ruled out, the self-electrophoresis model is likely the predominant mechanism contributing to Pt-Au rod motility.

2.5 Acknowledgements

I would like to acknowledge the following for their contributions: Professor Theresa Mayers' group for providing the L-EDIT mask designs for the fabrication of the electrofluidic rod assembly device. Rose Hernandez for assistance in the rod alignment step.

2.6 References

(1) Ismagilov, R., F; Schwartz, A.; Bowden, N.; Whitesides, G. M. *Angew. Chem. Int. Ed.* **2002**, *41*, 652.
(2) Paxton, W. F.; Kistler, K. C.; Olmeda, C. C.; Sen, A.; St. Angelo, S. K.; Cao, Y.; Mallouk, T. E.; Lammert, P. E.; Crespi, V. H. *J. Am. Chem. Soc.* **2004**, *126*, 13424-13431.
(3) Dhar, P.; Fischer, T. M.; Wang, Y.; Mallouk, T. E.; Paxton, W. F.; Sen, A. *Nano Lett.* **2006**, *6*, 66.
(4) Kline, T. R.; Paxton, W. F.; Wang, Y.; Velegol, D.; Mallouk, T. E.; Sen, A. *J. Am. Chem. Soc.* **2005**, *127*, 17150-17151.
(5) Paxton, W. F.; Baker, P. T.; Kline, T. R.; Wang, Y.; Mallouk, T. E.; Sen, A. *J. Am. Chem. Soc.* **2006**, *128*, 14881-14888.
(6) Subramanian, S.; Catchmark, J. M. *J. Phys. Chem. C* **2007**, *111*, 11959-11964.
(7) Wang, Y.; Hernandez, R. M.; Bartlett, D. J.; Jr, n.; Kline, T. R.; Sen, A.; Mallouk, T. E. *Langmuir* **2006**, *22*, 10451.
(8) Paxton, W. F.; Sen, A.; Mallouk, T. E. *Chem. Eur. J.* **2005**, *11*, 6462-6470.
(9) Martin, C. R. *Science* **1994**, *266*, 1961.
(10) Martin, C. R. *Acc. Chem. Res.* **1995**, *28*, 61.
(11) Hernandez, R. M.; Richter, L.; Semancik, S.; Stranick, S.; Mallouk, T. E. *Chem. Mater.* **2004**, *16*, 3431-3438.
(12) Park, S.; Lim, J.; Chung, S.; Mirkin, C. A. *Science* **2004**, *303*, 348.
(13) Gustafsson, G.; Lundstrom, I.; Liedberg, B.; Wu, C. R.; Inganas, O.; Wennerstrom, O. *Synth. Met.* **1989**, *31*, 163-179.
(14) Sadki, S.; Schottland, P.; Brodie, N.; Sabouraud, G. *Chem. Soc. Rev.* **2000**, *29*, 283.
(15) Thiéblemont, J. C.; Gabelle, J. L.; Planche, M. F. *Synth. Met.* **1994**, *66*, 243-247.
(16) Smith, P. A.; Nordquist, C. D.; Jackson, T. N.; Mayer, T. S.; Martin, B. R.; Mbindyo, J.; Mallouk, T. E. *App. Phys. Lett.* **2000**, *77*, 1399-1401.
(17) Kovtyukhova, N. I.; Mallouk, T. E.; Mayer, T. S. *Adv. Mater.* **2003**, *15*, 780-785.

(18) Paxton, W. F.; Kistler, K. C.; Olmeda, C. C.; Sen, A.; St. Angelo, S. K.; Cao, Y.; Mallouk, T. E.; Lammert, P. E.; Crespi, V. H. *J. Am. Chem. Soc.* **2004**, *126*, 13424.

(19) Paxton, W. F. *Dissertation in Chemistry*; Pennsylvania State University: University Park, **2006**.

Chapter 3

Catalytic Micromotors for Transport of Colloidal Cargo

3.1 Introduction

Autonomously moving Pt-Au micromotors should, in principle, deliver materials in a site-directed fashion, powering the assembly of dynamic, non-equilibrium superstructures. These miniature workhorses could then be programmed to control the transport and organization of materials at the mesoscopic level, as inspired by the elegant chemomechanical ballet that is cellular biology. Such capabilities would be valuable for bottom-up assembly of superstructures and devices, targeted delivery of chemicals, roving sensors, etc. Several groups have reported transport of microscale loads using biomotors such as phototactic bacteria and kinesin motor proteins.[1,2]

In this chapter, the first report of synthetic motors for transport of microscale payloads is demonstrated. Catalytic Pt-Au motors were linked to prototypical cargo: polystyrene microspheres. A quantitative study of a Pt-Au motor's cargo-carrying capability, elucidating systematic trends in motor speed as a function of cargo radius is also presented. In addition, directionality of motors-cargo doublets was improved by incorporating Ni segments in the motor design. The magnetic Ni segments aid in minimizing both Brownian orientational fluctuations and biased rotation of the doublet to enable persistent steerable, uniaxial motion in an external magnetic field. While the drag on regular shapes like spheres and cylinders is well-known, the shape of the motor-cargo

doublet is unique. Our collaborators in the Physics department, Dr. Crespi and Dr. Lammert, computed the drag on the rod-sphere doublets using a boundary integral equation and thereby demonstrated that doublets with largest-radius cargos exhibit an anomalously large motility.

3.2 Attaching Colloidal Cargo to Catalytic Motors

Pt-Au rods were prepared by galvanostatic deposition in the pores of alumina membranes and released as described previously.[3] Briefly, a sacrificial silver layer was deposited to block the branched portion of the membrane, followed by platinum and finally gold deposition. Pt-Au-PPy and Pt-Ni-Au-Ni-Au-PPy rods were prepared in a similar fashion, with the PPy being deposited last. The electropolymerization of the aqueous 0.5 M pyrrole solution was carried out in the presence of 0.1 M KCl by cycling the potential between 0.8 and 1.0 V vs. Ag/AgCl reference electrode at 20 mV/s.[4]

All electrodeposition steps were carried out using a potentiostat (Pine model AFRED5). The lengths of the Pt and Au segments were approximately 1.2 µm each in Pt-Au and Pt-Au-PPy rods. In Pt-Ni-Au-Ni-Au-PPy rods the Pt segment was nearly 1.2 µm, the Ni segments were 100 nm long and separated by a 200 nm long gold segment, while the terminal Au segment was nearly 800 nm long. The length of the polypyrrole segment ranged from 100 to 800 nm. The diameter of the rods is approximately 370 nm. Lengths were characterized by transmission electron microscopy (JEOL1200 EXII), scanning electron microscopy (JEOL JSM 5400), and dark-field optical microscopy (Zeiss Axiovert 200 reflectance/transmission).

Pt-Au, Pt-Au-PPy, and Pt-Ni-Au-Ni-Au-PPy motors were attached to polystyrene cargo of varying radii. To provide a reasonably consistent geometry, we attached the cargo to the tip of the rod, using the two methods shown in Figure **3-1**. First, electrostatic interaction was used to attach positively charged polystyrene-amidine microspheres (Interfacial Dynamics) to a negatively charged PPy segment at one end of the rods. The PPy segment enabled preferential attachment of the cargo, as it bears a more negative zeta potential (-35 mV) than the metal segment (-10 mV), as determined by zeta potential measurements (Brookhaven Zeta PALS) of PPy rods and Pt-Au rods. The PPy segment in our rods is deposited at a higher oxidation potential than required for pyrrole monomer oxidation (approximately 0.6 V vs. Ag/AgCl reference electrode). As a result, in the overoxidized polymer, hydroxyl, carboxyl, and carbonyl groups are incorporated along the polymer chain, which contribute to the observed negative zeta potential of the polymer.[5] In addition to the electrostatics, hydrogen bonding between the functional groups of the motor (imine groups in the polypyrrole) and cargo (amidine groups) also likely contributes to motor-cargo attachment.

A 1:2 mixture of rods and spheres was allowed to couple over several minutes. Subsequently, the autonomous motion of the motor-cargo doublets in aqueous 5% H_2O_2 solution was observed through an optical microscope. The great majority of doublets had the cargo fixed to the desired PPy/gold end; a few motors pushed rather than pulled their cargo, which were non-specifically bound to the Pt end. The second attachment method used a more specific biotin-streptavidin interaction: the Au ends of the Pt-Au rods in-membrane (with no PPy segment) were exposed to a 1 mM ethanolic solution of biotin-terminated disulfide; (EZ-Link Biotin HPDP, Pierce) to form a self-assembled monolayer

of biotin-terminated disulfide.[6] The functionalized rods were released by dissolving the membrane in dilute NaOH and subsequently mixed with streptavidin-coated microspheres (Polysciences). While the latter method gave higher yields of doublets with the desired geometry, the former method was used for further quantitative study of rod motion because positively charged amidine-coated microspheres are available in a wider range of radii than streptavidin-coated microspheres.

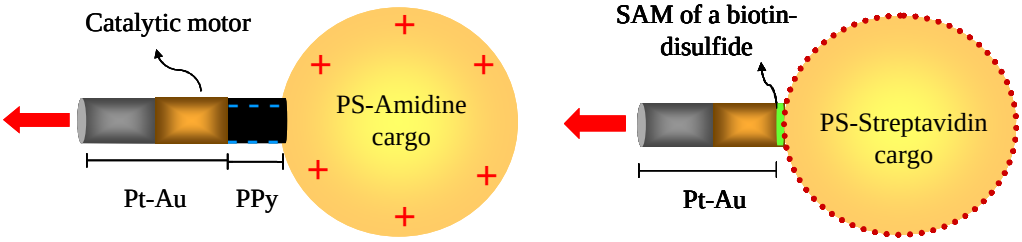

Figure **3-1**: Cargo attachment by (left) electrostatic interaction between the negative PPy end of a Pt-Au-PPy motor and a positively charged PS amidine microsphere and (right) biotin-streptavidin binding between the Au tips of Pt-Au rods functionalized with a biotin terminated disulphide and streptavidin-coated cargo.

3.3 Effect of Cargo Attachment

We attached amidine-functionalized PS microsphere cargo of radii 0.38, 0.60, 1.05, and 1.65 µm. Figure **3-2** shows a Pt-Au-PPy motor in action linked to a 1.05 µm cargo.

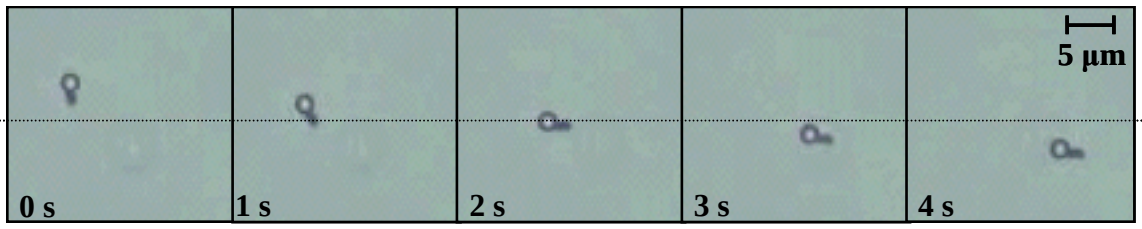

Figure **3-2**: Transmission optical microscopy images of Pt-Au-PPy motor pulling 1.05 μm radius cargo, showing the trajectory over 4 s. Images were captured at 1000 × magnification.

Video clips were recorded using an optical microscope equipped with a digital video camera connected to a PC. A steady decrease in speed with increasing cargo radius was anticipated. The 1.65 μm spheres slowed rods to such an extent that translational motion was barely discernible, although non-Brownian rotational motion could be observed in some doublets. Table **3-1** shows the doublet speed as a function of cargo radius (these are discussed in greater detail below). Columns I, II, and III are repetitions with different batches of rods and depict the observed batch to batch variability in rod speeds. Each entry is an average over 20 or more rods; the sample standard deviations are indicated alongside. To determine doublet velocities, video clips were analyzed by an internally developed MATLAB-based particle tracking program.

Table **3-1**: Effect of Cargo Radii on Pt-Au-PPy motor Speed

Cargo Radius (μm)	**Speed (μm/s) I**	**II**	**III**
0	7.4 ± 0.3	6.4 ± 0.2	6.1 ± 0.1
0.38	5.9 ± 0.4	5.1 ± 0.1	4.7 ± 0.3
0.6	4.9 ± 0.2	4.3 ± 0.1	3.7 ± 0.3
1.05	3.9 ± 0.2	3.5 ± 0.1	3.0 ± 0.1

All trajectory data, for both diffusive and powered motion, were collected within 5 minutes of placing the solution on a glass slide. Pt-Au rods and rod-sphere doublets

typically sit 2-3 µm above the surface of the glass.[‡] Hence it was necessary to determine whether the interaction between the positively charged microspheres and the oppositely charged glass substrate affect the doublet speed. Any impediment due to this interaction would be revealed by a lowering of the diffusion coefficient below that expected for a free particle in two dimensions. The translational diffusion coefficients in water, of the 0.6, 1.05, and 1.65 µm radius spheres (without motors) when sitting 2-3 µm above the surface were measured. Video clips of the microspheres in water were analyzed using a homemade, MATLAB based particle tracking program. The measured average diffusion coefficients of particles after 5 min for 0.6, 1.05, and 1.65 µm radius spheres are 4.3×10^{-9}, 2.2×10^{-9}, and 0.8×10^{-9} cm^2/s, respectively, compared to theoretical values of 4.1×10^{-9}, 2.0×10^{-9}, and 1.9×10^{-9} cm^2/s. The close agreement between the theory and experiment for the 0.6 and 1.05 µm spheres suggests that the interaction between these spheres and the glass substrate is minimal. The lower experimental diffusion coefficient for the largest (1.65 µm) spheres indicates that substrate effects cannot be neglected in this case: at this separation from the surface, a 1.65 µm radius cargo is nearly dragging on the surface, and rods attached to such spheres are greatly hindered. The diffusion coefficients in water of doublets with 0.6 and 1.05 µm spheres were also measured; they are reasonably stable over the course of 30 min, Table **3-2** . Doublets have smaller diffusion coefficients than the plain spheres, as expected. Since all videos of non-

[‡] In order to calibrate the z axis vertical motion, a glass slide or cover slip of known thickness is viewed under the microscope. The top surface and the bottom surfaces are each bought to focus separately. The angular displacement of the z axis control / focus control knob on the optical microscope is noted in going from one surface to the other. From the known thickness of the slide / cover slip, the angular displacement of the focus knob is correlated to the vertical distance traversed. Thus an estimate of the level in which objects reside is obtained.

Brownian motion are recorded within the first 5 minutes of placing the solution over the glass slide, the stability of both sphere and doublet diffusion over much longer times suggests that substrate-cargo interaction has a negligible effect on doublet speed for 0.6 and 1.05 μm radius cargo.

Table **3-2**: The average diffusion coefficients of 0.6 μm rod-sphere doublets, 1.05 μm rod-sphere doublets and Pt-Au-PPy rods measured over 30 minutes. The sample standard deviations are indicated over time. The diffusion coefficients are stable over 30 minutes of placing the solution over the glass slide, the observed stability of both sphere and doublet diffusion over much longer time suggests that substrate-cargo interaction has a negligible effect on the doublet speed for 0.6 and 1.05 μm radius cargo.

Time (min)	**Diffusion Coefficients × 10^{-9} cm^2/s**		
	0.6 μm Cargo-Rod Doublets	**1.05 μm Cargo-Rod Doublets**	**Pt-Au-Ppy Rods**
5	3.0 ± 0.8	1.8 ± 0.8	3.1 ± 0.8
10	3.0 ± 0.6	1.4 ± 0.4	3.6 ± 1.0
15	2.9 ± 0.7	1.4 ± 0.2	3.4 ± 0.7
20	2.8 ± 0.7	1.5 ± 0.4	4.1 ± 0.5
25	2.3 ± 0.8	1.5 ± 0.2	4.0 ± 0.6
30	2.3 ± 0.7	1.7 ± 0.4	3.0 ± 0.7

3.4 Remote-Controlled Pt-Ni-Au-Ni-Au-PPy Motors for Increased Directionality.

Unconstrained autonomously moving catalytic motors, with or without cargo, exhibit orientational diffusion. In addition, rods which are attached asymmetrically to cargo tend to exhibit a sustained biased rotation, an effect that is more pronounced at larger cargo diameters. For applications such as transport and delivery in the mesoscale, it is necessary to overcome these two effects and sustain directionality across both time and space. Hence we have incorporated thin Ni segments into the motors, with the overall segment sequence Pt-Ni-Au-Ni-Au-PPy.[7] Such motors can be oriented by an external magnetic field because the Ni segments experience a magnetic torque. Two small NdFeB bar magnets, parallel and equidistant from the sample on opposite sides, produce a field of a few hundred gauss.[7] The external magnetic field completely suppresses the orientational drift and diffusion, except for a residual fluctuation about the preferred axis (perpendicular to the field direction and parallel to the surface of the slide), as shown in Figure **3-3**.

Table **3-3** and Table **3-4** summarize the rotational characteristics of ~10 doublets for each cargo size (radii: 0.38, 0.60, and 1.05 μm), as well as rods with no cargo, in the absence and presence of the magnetic field. Motions with or without magnetic field are qualitatively distinct, so different physical quantities (with different units) are necessary to describe them.

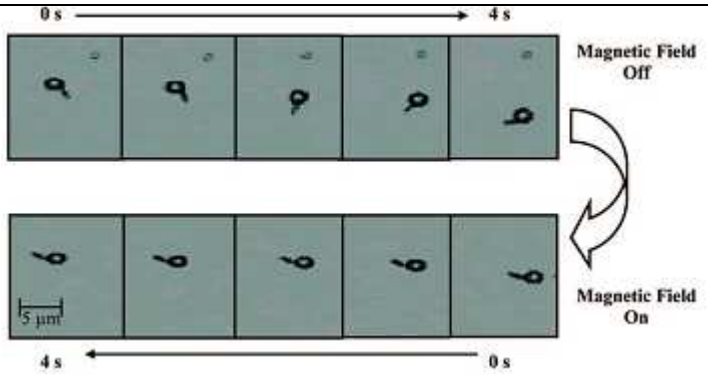

Figure **3-3**: Transmission optical microscopy images of a Pt-Ni-Au-Ni-Au-PPy motor pulling 1.05 µm radius cargo, showing the trajectory over 4 s. Images were captured at 1000× magnification. The top pane shows the trajectory in the absence of the field while the bottom pane shows the trajectory in the presence of the field. The external magnetic field suppresses the rotation of the doublet.

The steady drift and rotational diffusion coefficient D_{rot} were obtained from statistical analysis. Motility in the absence of the external magnetic field is characterized by a biased rotational drift θ, (measured in degrees per second) superimposed with an orientational diffusion D_{rot}, (measured by a diffusion constant in degrees^2 per second). D_{rot} is given by Equation **3.1**:

$$<d(\xi)^2> = 2\, D_{rot}\, dt \qquad (\mathbf{3.1})$$

where $d\xi$ is the instantaneous rotational diffusion and dt is the time interval between consecutive frames. The duration of dt is 0.033 s; the capture rate of the video camera interfaced with the optical microscope that was used for the imaging experiments. The instantaneous observed orientational motion $d\theta$, is described as the sum of the instantaneous variables: biased rotation ($\omega\, dt$) and rotational diffusion $d\xi$, Equation **3.2:**

$$d\theta = \omega\, dt + d\xi \qquad (\mathbf{3.2})$$

where ω is the angular velocity of the particle tracked over the time interval *dt*.

From the video clips of doublet motion, $d\theta$ is empirically determined, for each rod or rod - cargo doublet. First, the orientation of the particle with respect to the x axis (defined as the horizontal of the video clip) is plotted as a function of time. $\Delta\theta_i$ is the difference in particle orientation values at times t = 0 s and t = 5 s. Subsequently, the contributions due to ω and D_{rot} (i.e., ξ) were determined.

Form the data we determine $\Delta\theta_i$ given by Equation **3.3**

$$\Delta\theta_i = \theta_{(i+1)} - \theta \qquad (\mathbf{3.3})$$

where, θ_i *and* θ_{i+1} are doublet orientations for consecutive frames.

We also obtain an estimate for the drift over the entire time duration (*T*) of the video clip, Equation **3.4** :

$$\omega = \{\theta(T) - \theta(0)\} / T \qquad (\mathbf{3.4})$$

The contribution due to rotational diffusion ξ is obtained as follows:

Equation **3.5**

$$\Delta\theta_i = \theta_i - \omega\,\Delta t \qquad (\mathbf{3.5})$$

D_{rot} is obtained for each particle over a 5 s video clip as follows, Equation **3.6** :

$$\frac{1}{N}\sum_{i=1}^{n}(\Delta\theta_i)^2 = 2D_{rot}\,\Delta t \qquad (\mathbf{3.6})$$

Motility in the presence of the field involves neither drift nor diffusion but simply a characteristic magnitude for angular fluctuations about the mean orientation. In the

presence of the magnetic field, the wobble parameter is the standard deviation in $\hat{D}_{rot}$ With no field, orientational drift of tens of degrees per second and effective rotational diffusion coefficients D_{rot} of several hundred to a few thousand degrees squared per second are common. Such values of D_{rot} are consistent with a purely thermal origin of the orientational diffusion, but there may be a significant component related to fluctuations in the reaction distribution and flexing of the PPy linkers. Doublets with 1.05 μm cargo have much slower rotational motion, as is to be expected. When the external field is imposed, the ability of rotationally biased doublets to cycle through 360° is fully quenched. The doublets are well-oriented, exhibiting fluctuations of only a few degrees, as shown in tables **3.3** and **3.4**.

While small, these orientational fluctuations are an order of magnitude larger than thermal fluctuations would produce if the net magnetic moments of the two Ni segments were aligned and saturated. This is not surprising, since the "two Ni pancake" geometry is designed such that the fields which the two segments exert on each other are comparable to or greater than the external field, and these self-fields favor opposite moments. More highly magnetized rods are not currently useful since they agglomerate so strongly as to interfere with doublet formation.

Table **3-3**: Effect of external magnetic field on Pt-Ni-Au-Ni-Au-PPy motors and motors with 0.38 μm radius cargo.. For each doublet or unloaded motor, five second video clips were taken in the absence and presence of a few hundred gauss field from a handheld magnet. In absence of a field, the orientational motion is assumed to consist of a steady rotational drift velocity (biased rotation) with rotational diffusion superimposed. The steady drift and rotational diffusion coefficient (D_{rot}) are extracted from a statistical analysis. There is a large uncertainty in the drifts due to the short length of the video clips. With the field on, the motors are strongly oriented along a direction perpendicular to the magnetic field. The reported wobble (with the field on) is the standard deviation of the orientation- in this case, the drift and diffusion coefficients are effectively zero over

long times.

	Rods		0.38 μm cargo		
Particle number	**D_{rot} (deg^2/s) [field off]**	**Wobble (deg) [field on]**	**Drift (deg/s) [field off]**	**D_{rot} (deg^2/s) [field off]**	**Wobble (deg) [field on]**
1	1072	4.8	-104 ± 26	3207	7.3
2	666	9.6	-173 ± 33	5058	6.7
3	3602	7.7	-174 ± 18	1476	5.1
4	1317	3.7	-193 ± 54	13444	6.9
5	2540	6	-44 ± 22	2349	5
6	2809	8.5	-6 ± 22	2353	8.7
7	562	7.6	-61 ± 20	1943	6.1
8	1790	5.7	73 ± 14	979	6.1
9	834	3.3	-73 ± 18	1498	5.9
10	573	5.9	-9 ± 27	3334	8.7

Table **3-4**: Effect of external magnetic field on Pt-Ni-Au-Ni-Au-PPy motors with cargo of 0.60 μm and 1.05 μm radius cargo.

	0.60 μm cargo			**1.05 μm cargo**		
Particle number	**Drift (deg/s) [field off]**	**D_{rot} (deg^2/s) [field off]**	**Wobble (deg) [field on]**	**Drift (deg/s) [field off]**	**D_{rot} (deg^2/s) [field off]**	**Wobble (deg) [field on]**
1	1 ± 12	617	8.7	0 ± 9	403	3.8
2	16 ± 12	664	5.4	0.0 ± 5.6	149.7	4
3	-16 ± 13	816	3.1	1.2 ± 6.1	174.9	14
4	20 ± 14	933	7.7	11 ± 8	295	3.8
5	-22 ± 12	620	3.7	14 ± 8	280	7
6	-3.9 ± 6.2	179.8	55.4	16 ± 10	464	4.8
7	33 ± 16	1243	5.8	18 ± 8	292	5.4
8	35 ± 12	674	3.9	-20 ± 6	172	5.6
9	-42 ± 13	768	7.3	37 ± 6	166	3.2
10	-5 ± 12	672	5.4	5.7 ± 8.4	328.4	6.2

3.5 Calculation of Drag on the Rod-Cargo Doublets[§]

While doing experiments to quantify the effect of cargo of various radii on Pt-Au motors, our collaborators in the Physics department were interested in computing the drag on motor-cargo doublets. While the drag on regular shapes like spheres and

[§] This section of the chapter was contributed entirely by Dr. Paul Lammert of the Physics department at Penn State.

cylinders is well-known, the shape of motor-cargo doublet shape is unique. The drag on on the rod-sphere doublets was computed using a boundary integral equation.

In our current understanding, electrochemical activity generates a persistent electric field which drives ion currents in the Debye layer around the motor. The corresponding reaction force of the ions on the motor is the primary motive force. The motor generates force throughout the Debye layer, which is comparable in thickness to the motor radius. Because of the thick Debye layer, it is not appropriate to analyze the situation in terms of slip velocity, as done by Golestanian et al. in recent interesting work on design of phoretic motors.[8] The force on the ions is rapidly transferred to the fluid, from whence some of it returns to the motor via viscous back-reaction. Using the generalized Lorentz reciprocal relation we can write Equation **3.7**,

$$\gamma\vec{U} = \vec{F}_{direct} + \int \vec{v} \cdot \vec{f}\, \mathrm{dx} \qquad \textbf{(3.7)}$$

for the velocity $\vec{U}$ of the doublet in translational motion along its symmetry axis, where γ is the drag coefficient, $\vec{F}_{direct}$ is the motive force, and the integral is the viscous back-reaction where $\vec{f}$ is the force density on the fluid resulting from the electric field set up by the motor's electrochemical activity and $\vec{v}$ is the fluid velocity which would be induced if the rod moved at unit speed in the absence of electrochemical activity.

Separation of the cargo from the catalytic part of the motor suggests that the cargo should not have a large effect on motor function, so we will assume that the magnitude of $\vec{F}_{direct}$ is independent of the cargo size. The viscous back-reaction is

difficult to estimate without detailed knowledge of the fields set up by electrochemical activity. If the back-reaction was independent of cargo size, the speed of a doublet would be inversely proportional to the drag coefficient γ. Naively, the viscous back-reaction is expected to be both negative (impeding motion) and increasing with the cargo size, so that the assumption of cargo independence should lead to an overestimate of the speed of large doublets relative to small doublets. Interestingly, the experiments reveal a correction in the opposite direction.

Since there are no closed-form expressions or useful approximations for the Stokes drag on a body shaped like our rod-sphere doublet, we compute γ via the completed double-layer boundary-integral equation method (CDL-BIEM).[9-11] This technique uses an indirect representation of the flow around a moving particle via point-force sources, with a singularity inside the particle and a force-dipole density on the surface. The latter is the principal unknown and is found through numerical solution of an integral equation on the particle surface. This method is well-suited to calculating particle mobility because the fluid bulk does not have to be treated explicitly.

We express the drag coefficient in terms of the radius of a sphere with the same hydrodynamic drag as the doublet: R_{eq}, so that a doublet moving at speed U incurs a hydrodynamic drag $6\pi\eta R_{eq}U$. From γ we compute the ratio of doublet speed to rod speed ($U_{doublet}$ / U_{rod}) for different cargo sizes and compare them to the experimental ratios (Table 3). The range of equivalent radii corresponds to the experimental range in lengths of PPy segments: the smallest corresponds to 2.5 µm long rods (a 2.4 µm motor plus a 0.1 µm PPy segment) and the largest to 3.2 µm long rods (0.8 µm PPy segment). If

the viscous back-reaction were independent of cargo size, we would expect the speeds of doublets to be inversely proportional to the equivalent radius. The ratios of cargo-loaded speed to unloaded speed calculated under this assumption are shown in Table **3-5**. Corresponding experimental ratios are shown in the last three columns. Although the origin of the anomalously high mobility for the doublets with the largest-radius cargo is unknown, it does bode well for future applications.

Table **3-5**: Experimentally observed doublet speeds versus theoretical expectations based on completed double-layer boundary-integral equation (CDL-BIEM) calculations. The equivalent sphere radius R_{eq} of a rod (Pt-Au-PPy) or a rod-sphere doublet is the radius of a sphere which has the same drag coefficient. The lower (higher) values correspond to rods of 2.5 (3.2) μm length, for cargo of the indicated radii. (The variation of length of the rods arises due to the polydispersity of PPy segments. The lengths of the Pt and Au segments were approximately 1.2 μm each, while the length of the PPy ranged from 0.1 μm to 0.8 μm).

R_{cargo} (μm)	**Req doublet calculated by CDL-BIEM (μm)**	**Velocity ratio predicted by R_{eq}**	**Experimentally observed velocity ratio ($U_{doublet}$ / U_{rod})**		
			I	**II**	**III**
0	0.46 - 0.53	NA	NA	NA	NA
0.38	0.59 - 0.65	0.78 - 0.81	0.80 ± 0.03	0.79 ± 0.01	0.76 ± 0.04
0.6	0.76 - 0.81	0.61 - 0.66	0.67 ± 0.01	0.67 ± 0.01	0.63 ± 0.03
1.05	1.14 - 1.18	0.40 - 0.45	0.53 ± 0.01	0.54 ± 0.00	0.49 ± 0.01

3.5.1 Particle velocity related to direct force and viscous back reaction

For a fluid velocity, pressure field pair (v, p), the hydrodynamic stress tensor is given by Equation **3.8**

$$\sigma_{ij} = -\,\delta_{ij}\, p + \eta\left(\frac{\partial v^{i}}{\partial x^{j}} + \frac{\partial v^{j}}{\partial x^{i}}\right) \qquad (\mathbf{3.8})$$

where η is the dynamic viscosity. If there are non-hydrodynamic body forces, such as an electrostatic force density $\vec{f}_e$ acting on the fluid, then for low Reynolds number,($\nabla \cdot \sigma = -\vec{f}_e$).

For two velocity-pressure pairs (v, p) and (v', p') outside a particle surface S, the generalized Lorentz reciprocal relation can be written (Equation **3.9)**[12,13]

$$\int_S v \cdot t'\, dA - \int_\Omega v \cdot f_e'\, dV = \int_S t \cdot v'\, dA - \int_\Omega f_e \cdot v'\, dV \qquad (\mathbf{3.9})$$

where,

$$\vec{t} = \sigma \cdot \hat{n}$$

is the surface traction exerted by hydrodynamic forces on the particle surface. With $\vec{v}'$ a Stokes velocity field ($\nabla \cdot \sigma' = 0$) such that

$$\vec{v}' \mid s = \hat{e},$$

where $\hat{e}$ is along a symmetry axis of the particle, the second term on the left-hand side of (Equation **3.9)** vanishes, while the first term is $\vec{U} \cdot \vec{F}'$. On the right-hand side, the first term is $\vec{e} \cdot \vec{F}$, leading to, Equation **3.10,**

$$\vec{U} \cdot \vec{F}' = \vec{e} \cdot \vec{F} - \int_{\Omega} \vec{f}_e \cdot \vec{v}' dV \qquad (\mathbf{3.10})$$

Since the primed variables refer to an ordinary Stokes flow situation, $\vec{F}' = -\gamma \hat{e}$, where γ is the drag coefficient for the symmetry axis. The particle speed in the presence of electrokinetic phenomena is then Equation **3.11**

$$\vec{U} = \frac{F_{direct}}{\gamma} + \frac{1}{\gamma} \int_{\Omega} \vec{f}_e \cdot \vec{v}' dV \qquad (\mathbf{3.11})$$

3.6 Summary

In summary, the feasibility of using the Pt-Au-PPy motors for transport of microsphere cargo was demonstrated. The motor function is not disrupted due to the presence of passive cargo although a decrease in speed was observed upon cargo attachment. Magnetic Ni segments incorporated into the rods quench the rotational diffusion (and biased rotation) in the presence of an external magnetic field, making such doublets ideal for cargo pick-up and delivery. Many interesting applications can be envisioned for such cargo-bearing motors in the mesoscale. Cargo can be concentrated at desired regions. This may find application in bottom-up assembly of colloids or for delivery of materials at a specific location whereupon further binding events may be triggered depending on cargo surface functionality. This would require the ability to pick up and drop off cargo. The concentration of colloids against natural tendency to diffuse is made possible by coupling with the motor-fuel interaction that lowers the overall free energy of the system.

3.7 Acknowledgements

I would like to acknowlege the following for their contributions toward the research described in this chapter: Dr. Paul Lammert and Dr. Vincent Crespi for the calculations of drag on rod-cargo doublets and quantitative data presented on the remote controlled rods. Undergraduates Andrew Zudans and Gregory Sloan for assistance in rod synthesis, particle tracking and movie capture.

3.8 References

(1) Weibel, D. B.; Garstecki, P.; Ryan, D.; DiLuzio, W. R.; Mayer, M.; Seto, J. E.; Whitesides, G. M. *Proc. Nat. Acad. Sci. U.S.A.* **2005**, *102*, 11963-11967.
(2) Bohm, K. J.; Stracke, R.; Muhlig, P.; Unger, E. *Nanotechnol.* **2001**, *12*, 238.
(3) Paxton, W. F.; Kistler, K. C.; Olmeda, C. C.; Sen, A.; St. Angelo, S. K.; Cao, Y.; Mallouk, T. E.; Lammert, P. E.; Crespi, V. H. *J. Am. Chem. Soc.* **2004**, *126*, 13424-13431.
(4) Hernandez, R. M.; Richter, L.; Semancik, S.; Stranick, S.; Mallouk, T. E. *Chem. Mater.* **2004**, *16*, 3431-3438.
(5) Shigi, H.; Kishimoto, M.; Yakabe, H.; Deore, B.; Nagaoka, T. *Anal. Sci.* **2002**, *18*, 41-44.
(6) K.K.Caswell; J.N.Wilson; U.H.F.Bunz; C.J.Murphy *J.Am.Chem.Soc.* **2003**, *125*, 13914-13915.
(7) Kline, T. R.; Paxton, W. F.; Mallouk, T. E.; Sen, A. *Angew. Chem. Int. Ed.* **2005**, *44*, 744-746.
(8) Golestanian, R.; Liverpool, T. B.; Ajdari, A. *New J. Phys.* **2007**, *9*, 2630.
(9) S.J.Karrilla; S.Kim *Chem. Eng. Commun* **1989**, *82*, 123-161.
(10) Power, H.; Wrobel, L. C. *Boundary Integral methods in fluid mechanics*, 1995.
(11) Power, H.; Miranda, G. *SIAM J. Appl. Math.* **1987**, *47*, 689.
(12) M.Teubner *J. Chem. Phys.* **1982**, *76*, 5564-5573.
(13) Kim, S.; Karrila, S. J. *Microhydrodynamics: Principles and Selected Applications*, 2006.

Chapter 4

Delivery of Colloidal Cargo Transported by Pt-Au Motors via Photochemical Stimuli

4.1 Introduction

In this chapter the use of photochemical stimuli for delivery of cargo from load bearing catalytic Pt-Au motors in H_2O_2 fuel solutions is described. Applications for motors that can transport and deliver materials in meso size regime include bottom-up assembly of structures, delivery of materials for performing localized reactions etc. For such applications transport and delivery of cargo is essential. Several methods of cargo drop-off can be envisioned.[1] The stimulus for unloading cargo could be chemical/internal (i.e. a motor swims into a region where presence of a chemical agent triggers release of cargo) or external (an external light source or magnetic field triggers release of cargo).

Wang et al. reported the loading and unloading of magnetic cargo by catalytic Pt/Carbon nanotube (CNT) -Au based motors in H_2O_2/N_2H_4 (hydrazine) fuel mixtures. In the report, magnetic attraction between the catalytic Pt/CNT-Au-Ni-Au and microsphere cargo with magnetic core was used to load the motor to cargo. Cargo drop-off was achieved by using an external magnet to change the motor direction by 180 degrees. Due to the sharp change in the motor-cargo trajectory, the viscous fluid drag on the cargo overcomes the weak magnetic attraction, leading to cargo release.[2]

We adopted a different approach wherein UV light was used as the stimulus to facilitate cargo delivery. Figure **4-1**, shows a schematic where irradiation of UV light

(365 nm) breaks the link holding a preformed motor-cargo doublet, releasing the cargo from the motor. Two routes for photochemically assisted cargo delivery were explored, namely: I) silver dissolution assisted and II) photocleavable bi-functional linker assisted cargo delivery.

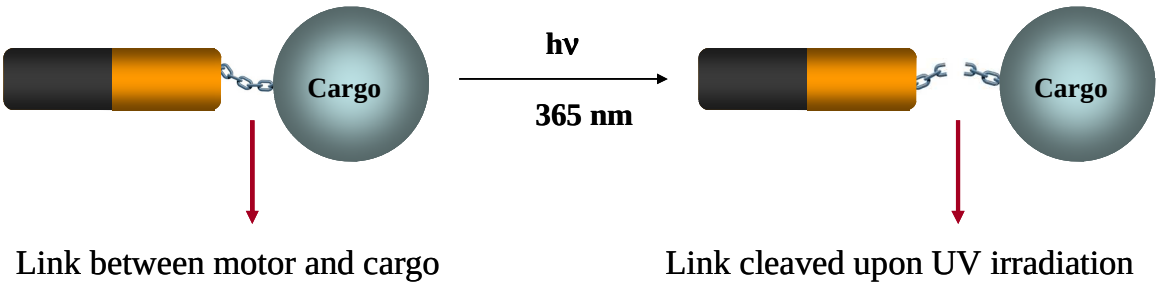

Figure **4-1**: Schematic for UV light induced cargo drop-off. The link connecting Pt-Au motor to the cargo breaks upon exposure to UV light (365 nm).

4.2 Silver Dissolution Assisted Cargo Delivery

For this mode of cargo delivery, catalytic motors containing silver segments were synthesized. This method of cargo drop-off is based on our observation of the rapid dissolution of Ag rods in the presence of chloride ions, H_2O_2 and UV light. Bulk silver metal is well known to dissolve in solutions of hydrogen peroxide in the absence of light.[3] Surprisingly, silver sections of nanorods only partially dissolve in the dilute solutions of peroxide used, leaving a mechanically robust organic residue behind in their place.[4] We have empirically found that adding chloride ions and UV light to the system results in a cleaner break of the silver nanorods and the accompanying residue. The mechanism of this light-induced dissolution in the presence of chloride ions is currently being investigated and likely involves the formation of an AgCl intermediate which is

known to decompose under UV illumination.[5,6] This result has been used for the light triggered release of cargo from preformed motor-cargo doublets.

Figure **4-2** shows a schematic of the Pt-Au-Ag-Au-Polypyrrole (PPy) catalytic motor design. In addition to the catalytic Pt-Au motor component motor, an Ag segment was deposited which dissolved to aid cargo delivery. The second Au segment was necessary as the electrodeposition of the PPy layer was found to occur more reproducibly on the Au surface than the Ag surface. The negatively charged PPy end was used to bind positively charged amidine-functionalized polystyrene microspheres (PS-Amidine) via electrostatic interactions.

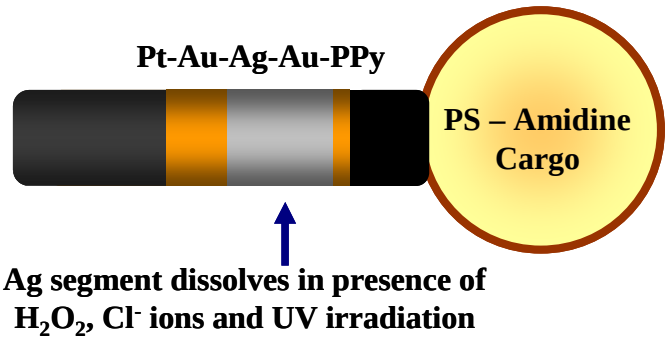

Figure **4-2**: Schematic of motor design for silver assisted cargo drop-off. Pt-Au-Ag-Au-PPy motor attached to positively charged 0.8 µm diameter PS-amidine cargo. The blue arrow points to the Ag section of the rod that dissolves in the presence of UV light (365 nm), releasing the cargo.

4.2.1 Synthesis of Pt-Au-Ag-Au-Polypyrrole Motors

Pt-Au-Ag-Au-PPy rods were synthesized by electrodeposition in alumina templates (Whatman). The rods were prepared by galvanostatic deposition in the pores of alumina membranes and released as described previously.[7] Briefly, a sacrificial silver

layer was deposited to block the branched portion of the membrane, followed by Pt, Au, Ag, a second Au deposition with the PPy being deposited last. The second gold deposition was required as electropolymerization of PPy on Au was found to be more reproducible than on Ag surface. The electropolymerization of the aqueous 0.5 M pyrrole solution was carried out in the presence of 0.1 M KCl by cycling the potential between 0.8 and 1.0 V vs. Ag/AgCl at 20 mV/s. All electrodeposition steps were carried out using a potentiostat (Pine model AFRED5). The lengths of the Pt and Au segments were approximately 0.5 µm each. The length of the Ag segment was approximately 0.3 to 0.5 µm, while the shorter Au segment was 0.1 µm long. The length of the polypyrrole segment was 0.2 to 0.5 µm. The diameter of the rods was approximately 0.35 µm.

Lengths were characterized by scanning electron microscopy (Leo 1530 FESEM), transmission electron microscopy (JEOL 2010 LaB6) and dark-field optical microscopy (Zeiss Axiovert 200 reflectance/transmission). Figure **4-3** and Figure **4-4** show SEM and TEM images of the rods respectively. Rods were released by first removing the sacrificial Ag layer in 20% nitric acid followed by dissolution of the alumina template in 0.5 M sodium hydroxide. 0.8 µm diameter PS-amidine microspheres were purchased from Invitrogen. The microsphere cargo and rods were premixed to form doublets followed by the addition of 10 µM KCl and 5% H_2O_2 (final concentrations).

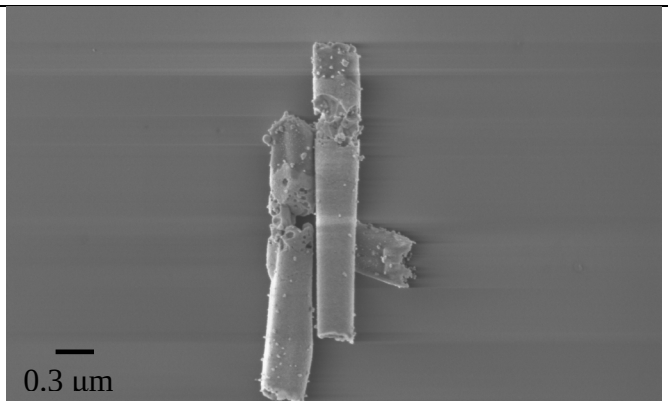

Figure **4-3**: SEM image of Pt-Au-Ag-Au-PPy rods.

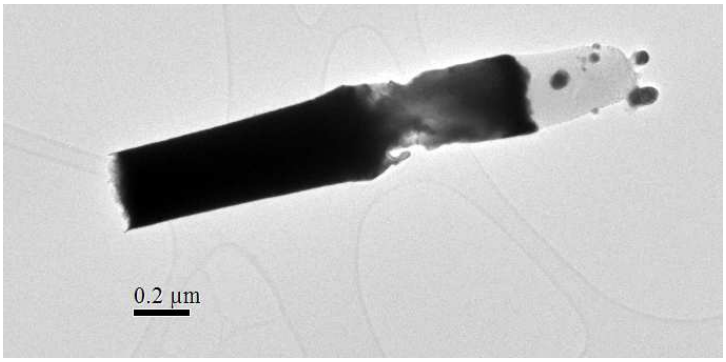

Figure **4-4**: TEM image of a Pt-Au-Ag-Au-PPy rod.

4.2.2 Cargo Drop-Off Experiments

The preformed cargo-motor doublets in the presence of 10 µM KCl, 5%H_2O_2 were exposed to UV light form a mercury lamp (Zeiss HBO 100) attached to the microscope. The light wavelength was predominantly 365 nm with a maximum power of 2.5 W/cm^2 when focused through a 100 × objective. Cargo drop-off was observed to occur within 10 - 20 seconds of UV light exposure. Figure **4-5**, shows screen capture

images of a Pt-Au-Ag-Au-PPy motor – microsphere cargo doublet, before and after drop-off. While this mode of cargo delivery is highly reproducible, the production of ions as a result of Ag dissolution eventually increases the ionic strength of the system leading to decrease in motor speeds. Motor average speed prior to UV exposure was approximately 2 to 3 μm/s. Post UV exposure the speeds decreased to 1 to 1.8 μm/s. In some cases the motor motility was suspended immediately after UV exposure. The speed v of a particle undergoing electrophoresis scales as a function of the parameters in the Helmholtz-Smoluchowski equation, Equation **4.1**:

$$v \propto \mu_e E \qquad (\mathbf{4.1})$$

where, μ_e is the electrophoretic mobility of the bimetallic particle (a function of the dielectric constant, solution viscosity, particle's dimensions and particle's zeta potential) and E is the electric field generated by the flux of ions. E is given by, Equation **4.2**:

$$E = \frac{J_+}{\sigma} \qquad (\mathbf{4.2})$$

where J_+ is the current density due to the electrochemical reaction and σ is the conductivity of the bulk solution. Thus, the velocity of the self-electrophoretic Pt-Au motor is expected to decrease with increasing ionic concentration, as is observed. In our experimental conditions Ag dissolution and the presence of Cl^- ions used to accelerate this process contribute toward reducing motor speeds.[**] Hence we explored another route

[**] The local ionic strength around each micromotor as a result of Ag dissolution cannot be easily determined, hence motor speed was not correlated to the changing ionic strength of the system pre and post UV exposure.

wherein the mechanism of cargo drop-off does not interfere with long term motor function.

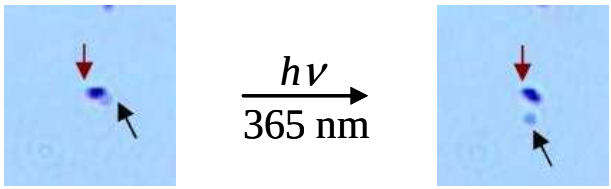

Figure **4-5**: Screen capture images depicting silver dissolution assisted cargo drop-off. The image on the left is before UV exposure and the image on the right is post UV exposure where the cargo dissociates from the motor. For clarity, the red arrow points to the motor and the black arrow to the cargo.

4.3 Photocleavable Linker Assisted Cargo Drop-Off

In this method of cargo drop-off a bi-functional molecule with a photocleavable moiety, (this molecule is henceforth referred to as photocleavable bifunctional linker (PCL)), was used to bring about cargo drop-off. One end of the PCL links to the motor while the other end attaches to the cargo. Figure **4-6** shows the schematic of motor design.

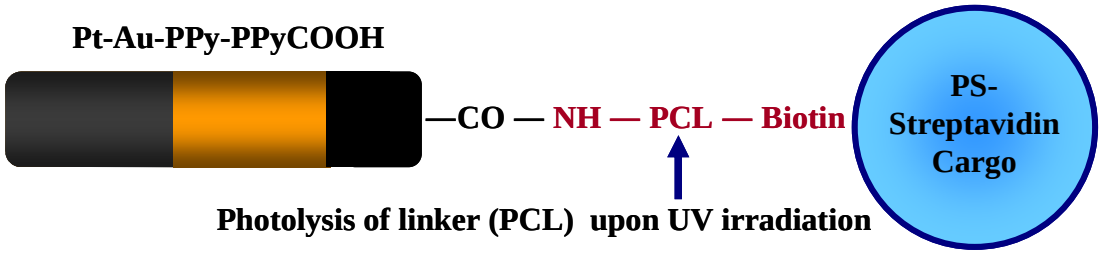

Figure **4-6**: Schematic of motor design for photocleavable bi-functional linker (PCL) assisted cargo drop-off. Pt-Au-PPy-PPyCOOH-PCL motors are attached to PS-streptavidin coated cargo. PPy-PPyCOOH refers to the copolymer of pyrrole (Py) and 4-(3-pyrrolyl)butyric acid (PyCOOH). The blue arrow indicates the PCL that breaks, releasing the cargo from the motor.

Pt-Au-polymer rods with carboxyl groups that covalently bind to cargo were synthesized. The carboxyl groups were incorporated by electropolymerizing pyrrole (Py) and 4-(3-pyrrolyl)butyric acid (PyCOOH) monomers, to yield a random copolymer PPy-PPyCOOH, Figure **4-7**. As with the homopolymerization of pyrrole, the polymerization occurs in the 2, 5 positions of the pyrrolic ring. The polymer end of the rod was functionalized with the bifunctional photocleavable linker (PCL), Figure **4-8** . PCL has a photocleavable moiety flanked by amine functionality on one end and biotin on the other end. The amine functionality affords attachment to the rod via amide bond formation and the biotin end was used to link motor to streptavidin coated cargo on the other end. Photolysis of the ortho-nitrobenzyl moiety affords release of cargo from motor. *Ortho*-nitrobenzyl based linkers are widely employed in combinatorial organic synthesis for light assisted release of surface bound molecules from solid supports.[8] Weibel et al. demonstrated the release of cargo from phototatic bacteria using such linkers.[9] Photolysis of PCL occurs upon UV illumination (365 nm) resulting in the formation of a methyl ketone and a primary amide, thereby facilitating release of the PS-Streptavidin cargo from the motor. [10,11]

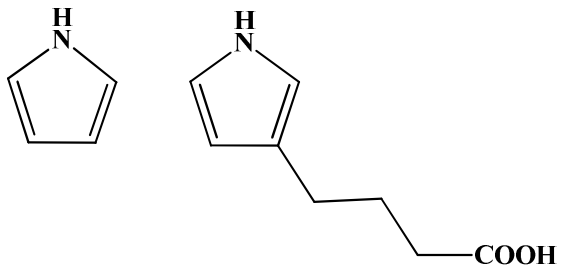

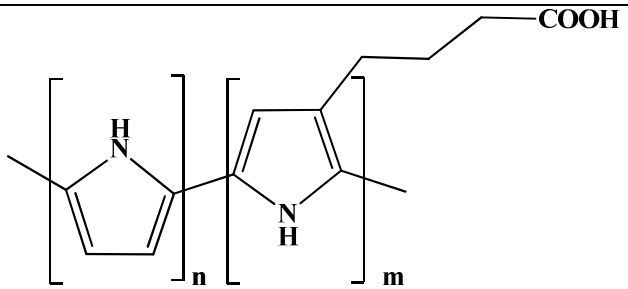

Figure **4-7**: Pyrrole (Py, top left) and 4-(3-pyrrolyl)butyric acid (PyCOOH, top right) monomers. Random copolymer of Py and PyCOOH (bottom), polymerization occurs at the 2 and 5 positions of the pyrrolic ring.

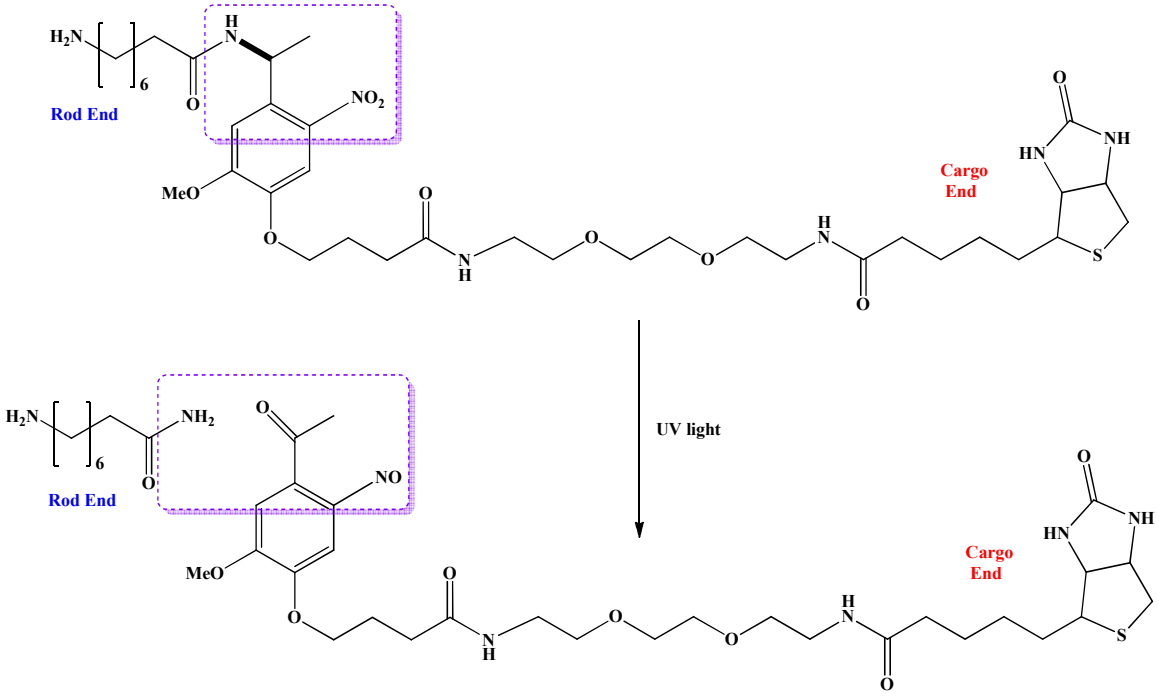

Figure **4-8**: Structure of the bifunctional linker with the photolabile bond (indicated in bold) also referred to as photocleavable linker (PCL). The amine end of the PCL is coupled to the carboxyl groups on the polymer end of the rod. The biotin end of the molecule couples with streptavidin coated cargo. UV illumination (365 nm) of the molecule results photo cleavage of the bond in bold resulting in formation of a methyl ketone and a primary amide.

4.3.1 Synthesis of Copolymer of Pyrrole – Pyrrole Carboxylic Acid

A copolymer of pyrrole (Py) and 4-(3-pyrrolyl)butyric acid (PyCOOH) was used to link the amine end of the PCL molecule to bind the motor and cargo. It was necessary to form a copolymer of Py and PyCOOH (PPy-PPyCOOH) instead of using PPyCOOH, as the latter polymer is completely soluble in basic conditions. A polymer that can withstand basic conditions is necessary as we use aqueous NaOH or KOH solutions to dissolve the sacrificial alumina template in which the rods are synthesized. Pure PPy is insoluble in the basic conditions used to dissolve the alumina membrane (0.2 M NaOH for 30 minutes).

To test the optimal monomer ratio for the copolymer several monomer ratios of Py and PyCOOH were tested: 0.1 M solutions of Py, PyCOOH and $LiClO_4$ were prepared in acetonitrile. Three monomer ratios were tried: a) 100% Py, b) 100% PyCOOH and c) 1:1 Py:PyCOOH. For ratios a) and b) 1 mL of the monomer solution was used. For ratio c) 0.5 mL each of Py and PyCOOH were used. The monomer mixtures were subsequently mixed with 1 mL of 0.1M $LiClO_4$. Electropolymerization of the mixtures was carried by cycling the potential between 3.5 and 4.0 V vs. a pseudo-reference Pt electrode at a rate of 50 mV/s to yield bulk polymer films on gold coated glass slides. Although both monomers are water soluble, acetonitrile was used as the solvent of choice. When the synthesis was carried out in aqueous solutions, the electropolymerization did not proceed as expected due to partial dissolution of oligomers of PyCOOH.

Using the above conditions, films formed after 3 seconds were found to be ideal for analysis by grazing angle IR studies films (Bruker IFS 66/s FT-IR Spectrometer). IR spectra of the films for the different compositions were obtained before and after exposure to 0.2 M NaOH solutions for 30 minutes. Films of pure PPy were insoluble in base whereas films of pure PPyCOOH dissolved in the basic conditions. Films with 1:1 ratio of Py and PyCOOH were found to withstand the base exposure and IR analysis of the showed the carboxyl groups were present post-base exposure. Figure **4-9** shows IR spectra of (from bottom to top) PPy, PPyCOOH, PPy-PPyCOOH, and base-treated PPy-PPyCOOH. The presence of carbonyl group adsorption of the –COOH group at 1711 cm^{-1} [1] in the base-treated PPy-PPyCOOH was confirmed. The 1:1 monomer mixture of Py and PyCOOH was used for electropolymerization of the polymer segment in the synthesis of Pt-Au-PPy-PPyCOOH rods. The grazing angle IR studies that were performed were qualitative in nature as the objective of the analysis was to confirm presence of carboxyl groups post-base exposure.

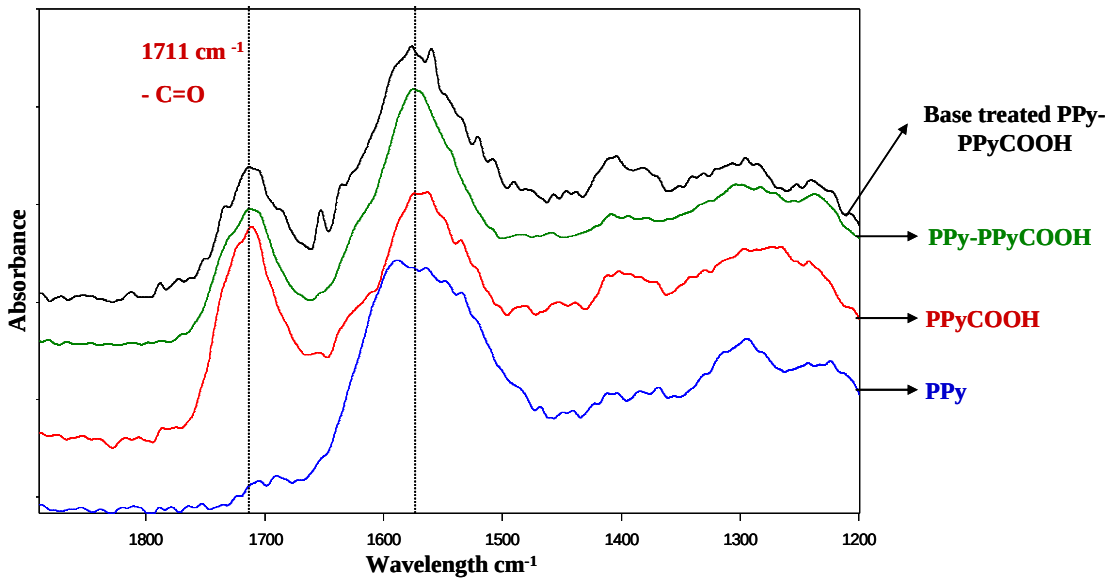

Figure **4-9**: Grazing angle IR spectra of bulk films of (from bottom to top) PPy, PPyCOOH, PPy-PPyCOOH, and base-treated PPy-PPyCOOH. The presence of carbonyl group adsorption of the –COOH group at 1711 cm^{-1} the base-treated PPy-PPyCOOH was confirmed. The other dotted line in the region around 1570 cm^{-1} corresponds to the pyrrolic C=C stretch vibrations.

4.3.2 Synthesis of Bifunctional Photocleavable Linker (PCL) Molecule

A bifunctional linker with a photocleavable moiety (PCL) was synthesized from the building blocks in Figure **4-10** .

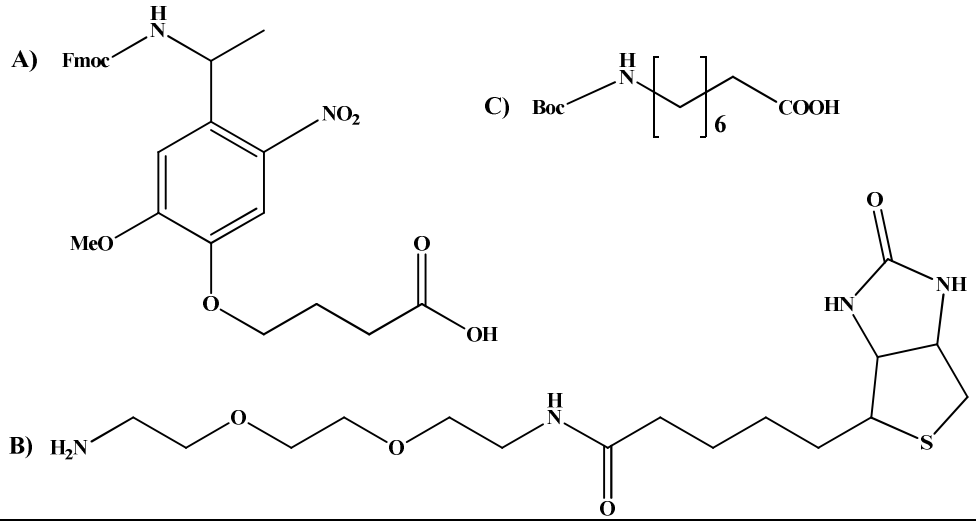

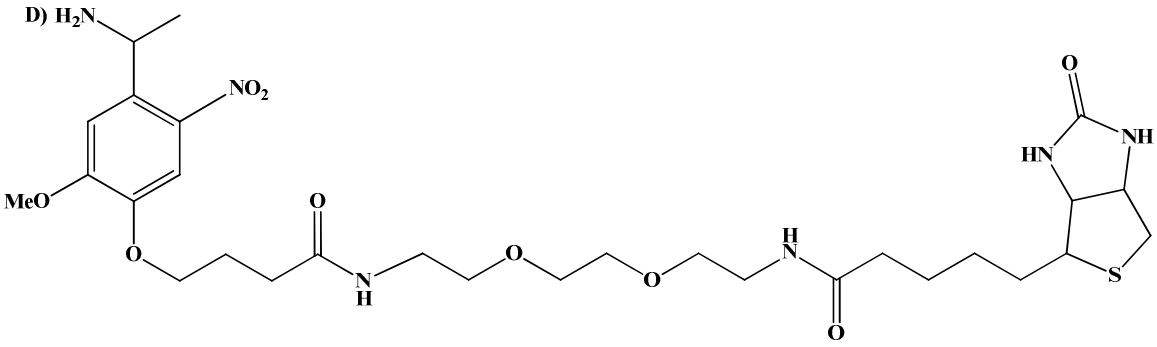

Figure **4-10**: Building blocks used in the synthesis of bifunctional photocleavable linker (PCL): **(A)** 4-[4-[1-[[(9H-fluoren-9-ylmethoxy)carbonyl]amino]ethyl]-2-methoxy-5-nitrophenoxy]-butanoic acid (Fmoc PC Linker), **(B)** Biotinyl-3,6-dioxaoctanediamine(Amine PEG2- Biotin), **(C)** *tert*-butoxycarbonyl-8-aminooctanoic acid, and **(D)** intermediate product of reaction between **A** and **B.**

A, 4-[4-[1-[[(9H-fluoren-9-ylmethoxy)carbonyl]amino]ethyl]-2-methoxy-5-nitrophenoxy]-butanoic acid (Fmoc PC Linker) and **C**, *tert*-butoxycarbonyl-8-aminooctanoic acid were purchased from Advanced Chem Tech and **B**, Biotinyl-3,6-dioxaoctanediamine(Amine PEG_2- Biotin), was purchased from Thermo Scientific. 1-Ethyl-3-[3-dimethylaminopropyl]carbodiimide hydrochloride (EDC), (N-Hydroxysuccinimide) NHS, piperidine, dimethyl formamide (DMF) and trifluoreacetic acid (TFA) were purchased from Sigma Aldrich.

Prior to the synthesis of the PCL molecule, control experiments were performed to study the photo-dissociation of molecule **A** in solution. Nearly 100 mg of compound **A** was dissolved in deuterated THF/D_2O (3:1 v/v, 1.5 mL) mixture and some of the solution was transferred to a NMR tube. Proton NMR spectra of the solution before and after UV exposure were acquired. First, the EDC assisted coupling of 175 mg **A**[††] and 100 mg of

[††] Prior to the synthesis of the PCL molecule, control experiments were performed to study the photo-dissociation of molecule **A** in THF/H_2O mixtures. A 100 mM solution of **A** was placed in an NMR tube and exposed to the UV lamp of the optical microscope. The UV exposure conditions were as follows: 20

B, was carried out in a 4:1 THF/H_2O mixture. Compounds such as EDC containing the carbodiimide functionality are used to activate carboxylic acids toward formation of an amide when reacted with an amine.[12] The reaction mixture was placed in an icebath and the reaction was carried out for 24 hours. A yield of over 50% was obtained. The reaction was monitored by thin layer chromatography (TLC) spotting using UV lamp and $KMnO_4$ staining. The solvent mixture used for TLC spotting was: 2:1:1 dicholoromethane: isopropyl alcohol: acetonitrile. Reactant **A**'s spot was visualized under UV light due to presence of aromatic ring and the spot moved with the solvent front. Reactant **B**'s spot was visualized by $KMnO_4$ staining, due oxidation of the amine group and the biotin moiety. Reactant **B**'s spot stayed at the base line of the acidic silica gel TLC plate. The product spot was visualized by both techniques and appeared at an intermediate R_f value.

The amide product was separated from the reactants by liquid-liquid extraction. First, the THF was evaporated and any unreacted **B** or water soluble byproducts of the EDC coupling reaction were removed by multiple washing water steps. While the amide product is insoluble in water, it prefers to reside in the aqueous layer thereby facilitating removal of excess **A** by multiple ether and hexane washings. The amide product was dried and was subsequently subjected to Fmoc. Fmoc is a protecting group used to block the reaction of amine functional groups in organic synthesis. In molecule A the presence of the Fmoc group prevents the polymerization of molecule **A** to itself when the EDC

---

seconds exposure time with constant shaking of the tube and light from UV source attached to microscope was focused through a 100× objective. Upon UV exposure, the solution in the NMR tube instantaneously changed color from light yellow to deep orange, likely due to the formation of the nitroso product. Proton NMR analysis of the solutions pre and post UV exposure were performed. Analysis of the post exposure tube confirmed the photo-dissociation of the compound **A**. The splitting pattern of the benzylic methyl group allowed for monitoring of the photocleavage reaction. In the reactant, the methyl group has triplet splitting pattern whereas in the methyl ketone product, a singlet peak is observed.

coupling reaction is initiated, thereby ensuring that amide bonds are formed between the carboxyl groups of **A** and the amine groups of **B**. Fmoc deprotection using piperidine and (dimethyl foramide) DMF, giving product **D**, Figure **4-10** .[13]

Product **D** was used for the next EDC coupling step where it was reacted with acid 140 mg of **C** in a 4:1 THF/H_2O mixture. The reaction was monitored by TLC using the developing solvent system described previously. Reactant **C** was not visualized due to absence of chromophores. Reactant **D**'s spot, an amine stayed close to the baseline, whereas the amide product had a higher R_f value than the reactant. The amide product was separated by liquid-liquid extraction. Reactant **D** separates into the aqueous phase. Reactant **C** is completely soluble in the hexane phase and the product, while insoluble in hexane, separates into that phase. The amide was obtained in 40% yield and was subsequently subjected to *tert*-butoxycarbonyl (Boc) deprotection using trifluoroacetic acid (TFA) in methanol, to give the final PCL molecule Boc, like Fmoc is an amine protecting functional group.[13] All reactions were carried out such that exposure to light was minimal to prevent photodecomposition of the photolabile moiety. The formation of the intermediate and final products obtained was confirmed by mass spectroscopy (Waters LCT Premier time-of-flight (TOF) mass spectrometer, electrospray ionization (ESI) in positive ion mode). The mass spectrum of the final product (PCL) Figure **4-11 ,** shows the high intensity molecular ion peak at m/z value of 796.4 units. The C-13 NMR analysis of the product was performed but did not prove to be as useful as the mass spectral analysis for identification. Product formation in each step involves amide bond formation. Both reactants and products contain amide groups in with similar chemical shifts. To ensure formation of product in high purity, multiple liquid-liquid extraction

steps were performed to separate reactants from products. In addition the mass spectrum of the final product did not contain the molecular ion peak of either reactant.

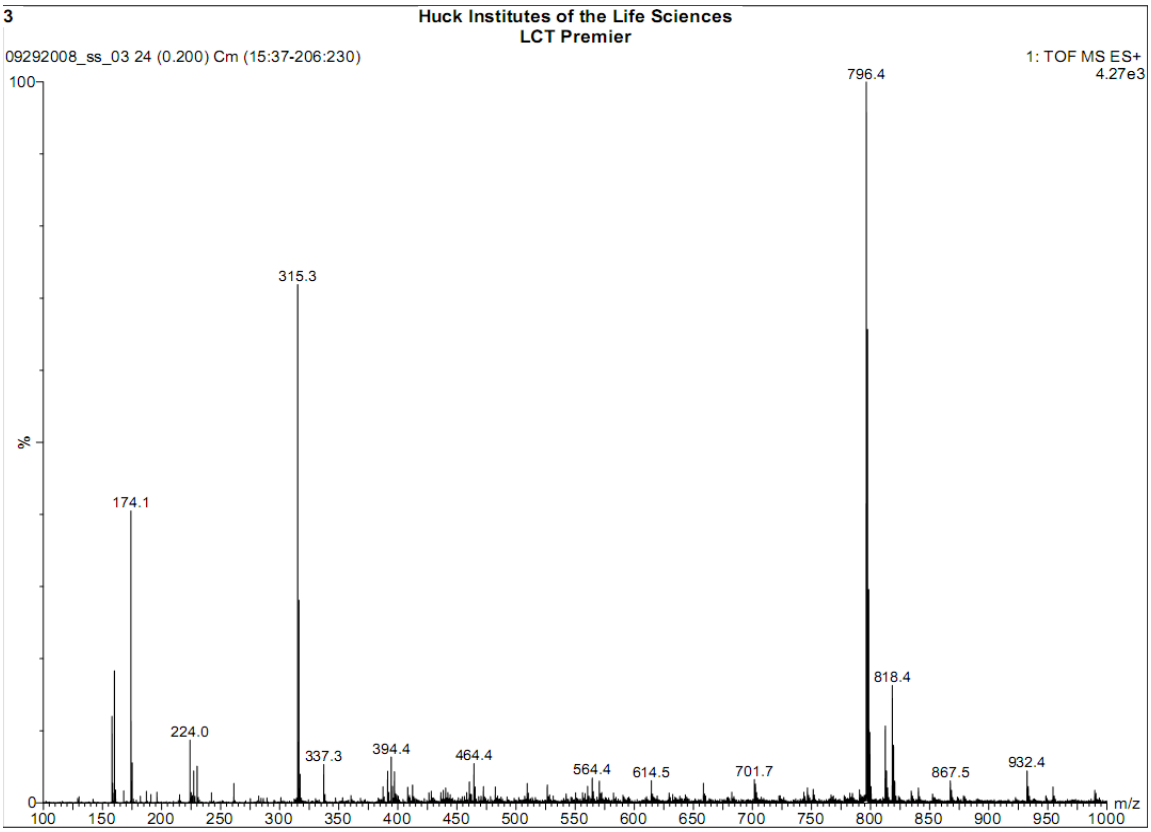

Figure **4-11**: Mass spectrum of the PCL molecule. The peak at m/z value of 794.6 corresponds to the molecular ion peak.

4.3.3 Synthesis of Pt-Au-PPy-PPyCOOH Rods with PCL Attached

Pt-Au-PPy-PpyCOOH rods were synthesized to enable covalent attachment of the amine end of the PCL to the carboxyl groups on the rods. The metallic segments of the rod were synthesized as described before.[7] The PPy-PPyCOOH segment was synthesized in the same manner as bulk films were synthesized as described in section **4.3.1** of this chapter. The electrodeposition time was increased to 30 s to yield polymer segments that

were 0.5 µm to 1.0 µm in length. The silver backing of the alumina template was dissolved in 20% nitric acid.

The attachment of the amine end of the PCL to the carboxyl groups on the polymer end of the rods was carried out while the rods were in the alumina membrane. A concentrated solution of the PCL in methanol was placed on the polymer side of the membrane and allowed to dry. Subsequently, EDC coupling was carried out to link the PCL to the polymer end. The water soluble EDC was washed and replaced multiple times to increase probability of reaction between the PCL and the polymer end of the rod. The rods were then released by dissolving the template in 0.2 M NaOH for 30 minutes. Figure **4-12** and Figure **4-13.** show SEM and TEM images of Pt-Au-PPy-PPyCOOH rods, respectively.

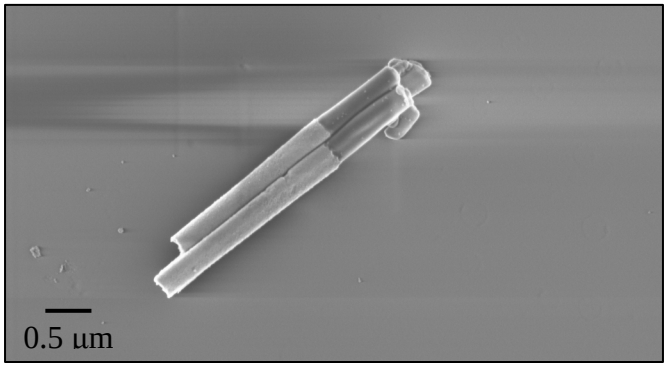

Figure **4-12**: SEM image of Pt-Au-PPy-PPyCOOH rods

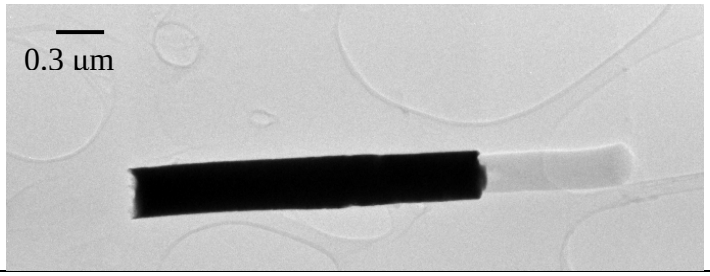

Figure **4-13**: TEM image of a Pt-Au-PPy-PPyCOOH rod.

4.3.4 Cargo Drop-Off Experiments

A dilute solution of 1 µm diameter PS-Streptavidin coated microspheres (Bangs Labs) was mixed with rods and kept aside for a few minutes to allow for rod-cargo doublet formation via biotin-streptavidin interaction This solution was then mixed with 5% H_2O_2, and a droplet of the mixture was placed in the microscope slide and irradiated with the UV lamp attached to the microscope. The light wavelength was predominantly 365 nm with a maximum power of 2.5 W/cm^2 when focused through a 100 × objective. Irradiation of UV light cleaves the photolabile bond leading to cargo drop-off.

In Figure **4-14**, the screen capture image on the left shows a Pt-Au-PPy-PPyCOOH rod linked to a streptavidin cargo via PCL molecules. The image on the right shows a screen capture shot taken post cargo drop-off.

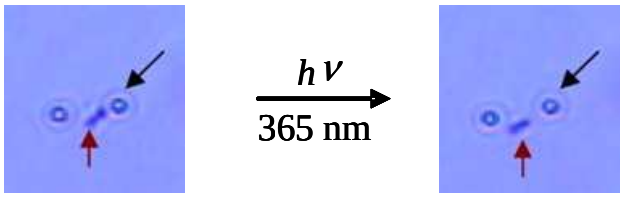

Figure **4-14**: Screen capture images depicting photocleavable linker assisted cargo drop-off. The image on the left is before UV exposure and the image on the right is post UV exposure where the streptavidin coated cargo dissociates from the Pt-Au-PPy-PPyCOOH motor. For clarity, the red arrow points to the motor and the black arrow to the cargo.

This mode of cargo drop-off typically took longer to achieve (60-100 s) than the Ag dissolution method (10-20 s). PCL assisted cargo delivery also suffered from poor

reproducibility. Cargo drop-off by this method was observed in only less than ten instances (i.e., less than ten cargo-motor doublets were seen to drop-off cargo). The Ag-assisted cargo drop-off method on the other hand was found to be far more reproducible; nearly every motor-cargo doublet with the cargo attached to the PPy end was found to release cargo upon UV exposure. The time taken for PCL detachment in motor-cargo doublets as evidenced from cargo delivery experiments (60-100 s) was slower than the photodissociation of a solution of compound **A**.[⌗] This may be attributed to the quantum yield of the PCL in the experimental conditions as well as shadowing effects of the motor and cargo.

In addition, since PCL attachment to the -COOH groups in the polymer ends of the rods was done in the confined geometry of the alumina membranes' pores, PCL loading may not have been sufficiently high. As a result, in some motor-cargo doublets, non-specific attachment of streptavidin cargo to the polymer end (with poor PCL loading) may have occurred. This was indeed the case in control experiments where streptavidin cargos were found to bind non-specifically to Pt-Au-PPy-PPyCOOH rods (without PCL). However in these control experiments motor-cargo doublets do not fall apart upon exposure to UV light. It may be noted that when the attachment of the PCL molecules was performed when the rods were released from the membranes, the rods did not exhibity motility in H_2O_2 solutions. This likely occurs due to the poisoning of the catalytic surface when it is exposed to the various chemicals used to attach the PCL to

[⌗] The photodissociation of the PCL molecule itself was not studied as the compound was not synthesized in sufficiently large quantities to perform control experiments. A solution compound **A** when exposed to UV light instantaneously changes color from light yellow to deep orange, likely due to the formation of the nitroso product, indicating the onset of photocleavage.

polymer end of the rod. When attempts were made to clean the motor surface by sonication, the polymer segment often broke off from the metallic motor segment. Therefore a milder method - vortexing was used to clean the motors post-PCL attachment but they proved to be ineffective as the motor motility was poor even after prolonged vortexing.

While we were able to demonstrate PCL assisted cargo delivery, other less arduous and more reproducible methods for cargo drop-off need to be explored. Wang et al. have proposed several cargo delivery methods using various triggers (UV light, chemicals etc.) that are worth exploring.

4.4 Summary

In this chapter two methods of cargo drop-off namely; Ag dissolution assisted and photocleavable linker assisted cargo delivery were discussed. In each case, UV light irradiation initiates a photochemical reaction that breaks the link connecting the motor and cargo. Ag dissolution assisted cargo drop-off is highly reproducible and occurs within 10-20 seconds of UV exposure. However the increase in the ionic strength of the medium due to Ag dissolution tends to slow down the motors eventually. Hence the photocleavable linker assisted route for cargo drop-off was explored to override this effect. In this method, the time required for drop-off was longer than the former method, typically 60-100 seconds of UV light exposure. Using light as a trigger for cargo drop-off, we can envision a high degree of precision in cargo drop off at desired locations. In

addition, the use of photomasks could in principle, facilitate simultaneous release of cargo at several locations.

4.5 Acknowledgements

I would like to acknowlege the following for their contributions toward the research described in this chapter: Mike Ibele for the discovery of Ag dissolution in UV light, Sam Sengupta for his assistance in the synthesis of the photocleavable linker, James Miller for acquiring mass spectra. Josh Stapleton for his assistance in grazing angle IR analysis of PPy-PPyCOOH films and Bangzhi Liu for his assistance with TEM – EDS data.

4.6 References

(1) Wang, J. *ACS Nano* **2009**, *3*, 4-9.
(2) Burdick, J.; Laocharoensuk, R.; Wheat, P. M.; Posner, J. D.; Wang, J. *J. Am. Chem. Soc.* **2008**, *130*, 8164-8165.
(3) Joksimovic-Tjapkin, S.; Delic, D. *Ind. Eng. Chem. Fundam.* **1973**, *12*, 33.
(4) *Personal communication with Michael Ibele.*
(5) Ibele, M. *Manuscript in preparation* **2010**.
(6) Clzaferri, G. *Catal. Today* **1997**, *39*, 145.
(7) Sundararajan, S.; Lammert, P. E.; Zudans, A. W.; Crespi, V. H.; Sen, A. *Nano Lett.* **2008**, *8*, 1271-1276.
(8) Holmes, C. P.; Jones, D. G. *J. Org. Chem.* **1995**, *60*, 2318.
(9) Weibel, D. B.; Garstecki, P.; Ryan, D.; DiLuzio, W. R.; Mayer, M.; Seto, J. E.; Whitesides, G. M. *Proc. Natl. Acad. Sci. U.S.A.* **2005**, *102*, 11963.
(10) Olejnik, J.; Sonar, S.; Krzymaska-Olejnik, E.; Rothschild, K. J. *Proc. Natl. Acad. Sci. U.S.A.* **1995**, *92*, 7590-7594.
(11) Holmes, C. P. *J. Org. Chem.* **1997**, *62*, 2370-2380.
(12) Hermanson, G. T. *Bioconjugate Techniques*; Academic Press: New York, 1996.
(13) *Protective groups in organic synthesis*; 3rd ed. / editors, Theodora Greene and Peter G.M. Wuts ed.; Wiley-Interscience, 1999.

Chapter 5

Enzyme Powered Micromotors

5.1 Introduction

In this chapter, experiments wherein the motility of enzyme functionalized spheres in the presence and absence of substrate is described. The enzyme catalase was immobilized asymmmetrically on 0.5 μm diameter microspheres. Catalase catalyzes the decomposition of H_2O_2 to H_2O and O_2. Since our groups' first report of Pt-Au catalytic motors, we and others have contributed to the understanding of mechanism of motility in the micromotors and explored applications for the same.[1] The mechanistic studies show that the predominant mechanism of motility is self-electrophoresis.[2,3] On the motor application front, research related to transport and delivery of cargo, improving motor speed, directionality and range of motion, have also been reported.[4-6] The use of other redox active fuels such as N_2H_4 have also been reported.[7] In all these studies, the micromotor is comprised of catalytic metal based systems such as Pt-Au or Pd-Au etc.

Feringa and coworkers reported two enzyme based motors involving decomposition of H_2O_2. In the first report, asymmetric silica particles (80 μm diameter) were functionalized with a manganese-based catalase mimic.[8] The catalyst was bound to the entire surface of the aminopropylmodified silica particles by imine linkages. Motility of the particles was observed when placed in H_2O_2 solutions. In the second report, the authors co-immobilized catalase and glucose oxidase (GOx) on multi-walled carbon

nanotubes (MWCNT, 20 - 80 nm diameter, 0.5 - 5.0 μm length).[9] Aggregates of the enzyme functionalized MWCNTs, (tens of μm in diameter) when placed in a glucose solutions, exhibited translational motion. H_2O_2, the byproduct of glucose oxidation to *δ*-glucono-1,5-lactone, served as substrate for catalase. In both reports, the motor design did not involve localized placement of the catalyst. Motility in these systems was facilitated by the inhomogeneous distribution of bubble nucleation sites on the asymmetric particle. When these particles are placed in a H_2O_2 solution, translational motion arises due to a bubble propulsion mechanism, due to expansion of oxygen bubbles that nucleated on their surface.

The most notable enzyme-based motor was designed by Heller et al.. In this breakthrough report, bioelectrochemical decomposition of substrates on either poles of a cm sized object was reported.[10] A carbon fiber (0.5 cm^{-1} length, 7 μm diameter), was functionalized with two redox enzymes. Glucose oxidase (GOx), that catalyzes the oxidation of glucose to *δ*-glucono-1,5-lactone was placed on one end and the opposite end was functionalized with bilirubin oxidase (BOD), an O_2 reducing enzyme. Equation **5.1**, **5.2**, and, **5.3** are the anodic, cathodic and overall reactions, respectively. When the fiber was placed in a buffer solution containing glucose, electrons flow along the path: glucose → GOx → carbon fiber → BOD → O_2. The fiber is propelled at the solution–air interface due to the ion flow in the fluid, accompanying the flow of electrons within the carbon fiber.

Anode reaction (at GOx):

$$\beta\text{-D-glucose} \rightarrow \delta\text{ -glucono-1,5-lactone} + 2\ H^+ + 2\ e^- \qquad \textbf{(5.1)}$$

Cathode reaction (at BOD):

$$\tfrac{1}{2}\ O_2 + 2\ H^+ + 2\ e^- \rightarrow H_2O \qquad (\mathbf{5.2})$$

Overall reaction:

$$\beta\text{-D-glucose} + \tfrac{1}{2}\ O_2 \rightarrow \delta\text{-glucono-1,5-lactone} + H_2O \qquad (\mathbf{5.3})$$

The use of enzymes for powering microscale reactions would be the next big advancement in the field of catalytic micromotors. Enzymes catalyze a wide range of reactions and are highly efficient. Catalyst turnover is crucial for motor action and enzymes such as carbonic anhydrase have reported turn over rates $10^6\ s^{-1}$.[11]

5.2 Catalase Based Micromotors

The objective of this project was to explore the feasibility of enzyme powered motion of microspheres. Catalase, an enzyme that converts H_2O_2 to O_2 and H_2O was chosen as it has one of the highest known enzymatic turnover number of nearly $10^{-7}\ s^{-1}$.[11] Also, catalase maintains its activity in the absence of buffers or in low ionic strength conditions.[12] This aspect is important due to the tendency of colloidal particles to stick to the surface or aggregate in high salt concentrations. Although the use of catalase brings us back to the use of H_2O_2 as a fuel, the enzymatic H_2O_2 decomposition is mechanistically different from the bipolar decomposition of the fuel in Pt-Au micromotors. In catalase, decomposition of the peroxide substrate occurs at a single

site.[13] Bovine liver catalase, used in our experiments, is a tetrameric enzyme containing four ferrihemoprotein groups per molecule.[14] The iron center in the active site, shuttles between the Fe (III) and Fe (IV) oxidation states as the substrate is decomposed to H_2O and O_2 in a two step reaction.

Unlike the self-electrophoretic mechanism in Pt-Au motors, a self-diffusiophoretic mechanism of motility would be in operation due to the single site decomposition of H_2O_2 in catalase.[15,16] Diffusiophoresis is the migration of colloidal objects due to a concentration gradient of a species. An object asymmetrically functionalized with a catalyst, when placed in the substrate would generate a gradient of reactants and products. Object motility arising from such self generated gradients of reactants and products is defined as self-diffusiophoresis. Golestanian et. al. reported the enhanced diffusion coefficient of half-Pt coated microspheres (1.62 μm in diameter) in H_2O_2 solutions. In their model, a self-diffusiophoretic mechanism of motion is believed to be in operation as the decomposition of the fuel occurs solely on the Pt surface.[16]

A similar approach for the design of catalase based motors was adopted, Figure **5-1**. Using particle lithography techniques, a spherical polystyrene carboxylate (PS-COOH) microsphere is coated with silica on one half. The asymmetric or Janus-type particle was then functionalized with catalase via covalent EDC assisted (1-Ethyl-3-(3-dimethylaminopropyl)carbodiimide)) coupling to the COOH groups on the uncapped side of the microsphere.

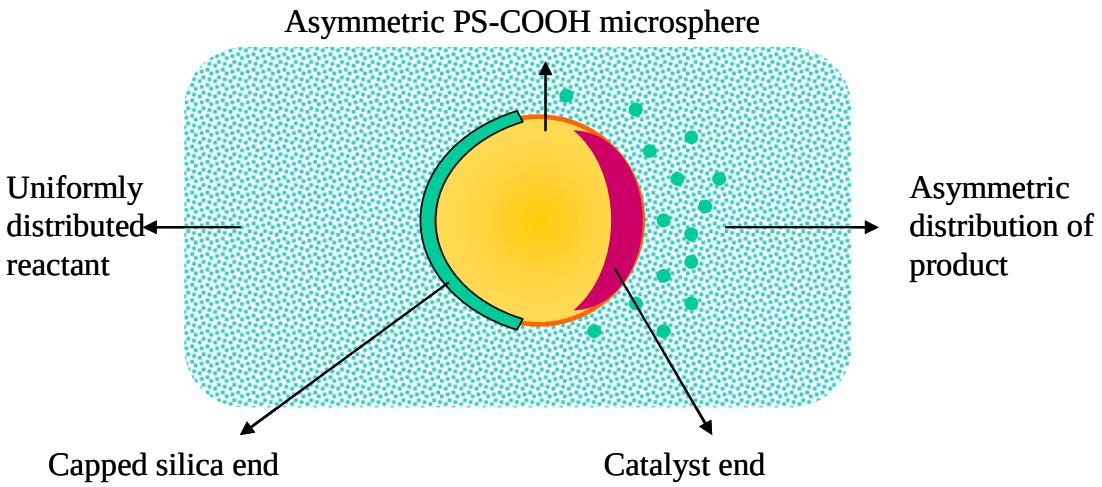

Figure **5-1**: Schematic of an self-diffusiophoretic "swimmer". A polystyrene microsphere is rendered asymmetric by evaporating silica on one end. The other end is functionalized with catalase. When placed in substrate solution the particle generates a gradient of substrate and product concentration.

It is worth mentioning here that Mallouk et al. reported that Au-Polypyrrole (PPy)/Catalase rods did not exhibit translational motion in H_2O_2 solutions.[3] In their experiment Au-PPy rods, (2 μm length, 360 nm diameter), were synthesized and catalase was physically entrapped in the polymer segment of the rod. When placed in H_2O_2 solutions, unlike Pt-Au rods, the Au-PPy/Catalase rods did not exhibit motility. The activity of the enzyme containing rods was comparable to that of the bimetallic rods. However, in their experiments, the authors were looking for fast swimmers like Pt-Au rods that move at speeds of 10 body lengths per second. The objective of the experiments discussed in this chapter was to investigate whether directional motion or just *enhancement of diffusion coefficients* would be observed in the presence of substrate.

5.2.1 Synthesis of 'Janus'-PS –Silica Particles

Polystyrene carboxylate (PS-COOH) particles 0.5 µm diameter (Polysciences) were coated on one half with silica to make them asymmetric. A monolayer of the microspheres was prepared by the procedure described by Goldenberg et al.[17] Briefly, a concentrated suspension of the microspheres was made in ethanol. A glass slide was placed in a petridish and the dish was filled with deionized water until the glass slide was completely submerged. Hexane was then pipetted onto the dish to cover the water surface. Using a micropipette, 1-3 µL of the microsphere suspension was placed at the hexane layer. A monolayer of microspheres forms at the water hexane interface. The glass slide underneath is carefully lifted through the liquid layers to keep as much of the monolayer intact on its surface as possible. After drying, 10 nm of silica was deposited on the monolayer coated glass slides (Semicore evaporator). The particles were subsequently freed from the glass slides by sonication and washed several times in ethanol. The solvent was dried to obtain the weight of the sample in order to get a estimate of the particle population required for subsequent calculations. Figure **5-2** shows an FESEM image of the PS-Silica particles. The supplier indicated the diameter of the particles to be 0.5 µm, but FESEM images reveal the diameter to be closer to 0.4 µm. The dried sample was resuspended in water and washed several times and stored in the refrigrator.

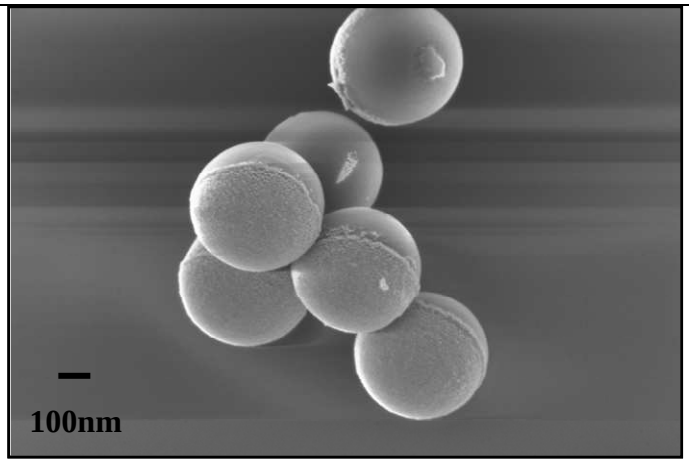

Figure **5-2**: FESEM image of 0.5 μm diameter Janus PS-Silica microspheres.

5.2.2 Catalase Immobilization on PS-Silica Microspheres

The carboxyl groups on the uncapped end of the PS-Silica particles were covalently attached to the amine groups on catalase via EDC / NHS (N-Hydroxysuccinimide) coupling. A solution of known microsphere concentration (typically 10^{9} to 10^{10} particles per mL) was washed and resuspended in deionized water, pH adjusted to 6.5. A 0.25 M solution of NHS was added to the particles followed by 0.1 M of freshly prepared EDC solution. The reaction vessel was stirred for 30 minutes to allow for formation of the NHS intermediate. NHS forms a stable intermediate with the carboxyl moiety allowing for a two-step coupling reaction. The particles were washed to remove unreacted EDC or NHS and subsequently reacted with 1 mL of a 1 mg/mL solution of bovine liver catalase (Sigma, lyophilized powder, >10,000 units/mg of protein). All solutions were made in deionized water, pH adjusted to 6.5. The reaction was allowed to take place for 5 hours after which the particles were centrifuged and the

supernatent enzyme solution was carefully recovered. The PS-Silica / Catalase particles were washed thoroughly and resuspended in 1 mL deionized water.

To quantify the amount of enzyme, aliquots of solution from the stock enzyme solution and the supernatent, recovered post-immobilization were analyzed by UV-visible spectroscopy. The absorption of catalase at 405 nm, due to the absorption of the heme moiety, was monitored in both solutions.[18] The amount of enzyme immobilized was calculated by subtracting the absorbance of the supernatant, recovered post-immobilization from the absorbance of the of the stock 1 mg/mL catalase solution.

The activity of the enzyme immobilized was measured by monitoring the decomposition of the H_2O_2 at 240 nm.[19] In a quartz cuvette, 20 μL of the PS-Silica / Catalase particles was mixed with 2 mL of H_2O_2 and and the decrease in absorbance of H_2O_2 at 240 nm was observed for 10 minutes. In between absorbance readings the cuvette was stirred to dislodge O_2 bubbles formed on the sides of the cuvette. After determining the amount of enzyme immobilized on the particles, a solution of free enzyme with concentrations comparable to that in the immobilized enzyme assay was made by serial dilution of the stock enzyme solution. Conditions for both assay experiments were identical.

The activity of the free enzyme was found to be nearly 55% of the maximum efficiency reported by the supplier (Sigma). Sigma reports a turnover rate of 1 μmol per minute for 1 unit of the enzyme. The vendor reported 135000 units of enzyme per mg of solid for that particular batch of catalase purchased. A decrease in activity was expected as the experiments were performed in deionized water instead of the recommended buffer solution. Upon immobilization, a further loss in activity was observed. In the

immobilized form, the activity was only 2-4% of the original activity reported by the supplier.

5.2.3 Tracking Diffusion Coefficients Using Nanosight LM

The Nanosight LM 10, a particle tracking instrument that uses a light scattering to track particles was used to measure diffusion coefficients of PS-Silica/Catalase particles in the presence and absence of substrate. A laser beam illuminates particles suspended in solution in the sample chamber. Video clips of particles illuminated by the beam are captured and analyzed using the tracking software provided by the vendor (Nanoparticle tracking software 2.0). The tracker records centre to centre displacement of particles in the video clip, while making corrections for bulk flow in the system. Figure **5-3** shows a screen-capture image of particles visualized by the Nanosight LM 10. The 2-D nature of the movies recorded is taken into account and the Stokes-Einstein equation for 2-D motion is utilized. The average diffusion coefficient of all the particles tracked in a video clip are exported to an excel file.

Figure **5-3**: Screen-capture image of PS-Silica/Catalase particles visualized using Nanosight LM.

Three sets of experiments were performed for each batch of PS-Silica / Catalase particles:

I) Control 1: PS-Silica/Catalase particles in deionized water

II) Control 2: PS-Silica/deactivated Catalase in 0.0625% H_2O_2 solution. In the PS-Silica/deactivated Catalase experiment, the enzyme was inactivated prior to measurement of diffusion coefficients. The inactivation was carried out by heating the particles to 75 °C for over 100 hours. Nearly 100% loss of activity was confirmed by UV assay, monitoring the turnover of H_2O_2 at 240 nm

III) PS-Silica/Catalase in substrate solution: 0.0625% H_2O_2 solution (final concentration).

5.3 Diffusion Coefficients of PS-Silica/Catalase Microspheres

Figure shows histograms of PS-Silica/Catalase particles in the three experimental conditions I), II), and III) described in the previous section. Approximately 10 video clips, 15 seconds in duration, were captured for each experiment and the experiments were repeated in triplicate to assess reproducibility. The plot in Figure **5-4** represents data from one such experiment. As the plot shows, no enhancement of translational diffusion coefficient in the presence of substrate was observed. The theoretical diffusion coefficient for 0.4 μm diameter particles is 1.23 $\mu m^2\ s^{-1}$. In Figure **5-4**, the abscissa extends to diffusion coefficient values of 4 $\mu m^2\ s^{-1}$. If the particles were monitored for longer duration the data points would converge closer to the theoretical value. In addition,

variations are expected due to polydispersity in particle size. Capturing video clips longer than 15 s in the case of experiment I) (PS-Silica/Catalase in H_2O_2) was not feasible due to disturbance caused by expansion of O_2 bubbles formed during the reaction.

Similar results were obtained for repetitions of the experiment within the same batch and across different batches of particles. The reason for no enhancement in diffusion coefficient of the particles in the presence of substrate solution, is most likely the poor activity of the immobilized enzyme. Enzyme activity may be improved upon by modifying the immobilization procedure. Instead of using a 'zero length' linker like EDC, longer molecular tethers could be used to link enzyme to the microscale object, allowing better access of the substrate to the active site.[20]

The activity (oxygen production rate) of Pt-Au rods in 3% H_2O_2 was reported to be 9.7×10^{-17} mol O_2/sec. For PS-Silica/Catalase particles the activity per particle in 0.0625% H_2O_2 was determined to be in the range 3.5 to 5.0×10^{-16} mol O_2/sec. Although catalase spheres have a higher per particle activity than the Pt-Au motors, they do not exhibit motility. This may be explained by the different mechanism of H_2O_2 decomposition. In the Pt-Au system, active fluid transport occurs from one pole of the particle to the other due to bipolar H_2O_2 decomposition. In the enzymatic system the fuel is converted to both products H_2O and O_2 at a single site. Therefore, is it plausible that self-diffusiophoresis may not be powerful enough for generation of powered Brownian or non-Brownian motion?[15] To answer this question definitively, we need to repeat this study with more active particles. Currently the immobilized enzyme activity is less than 5% of the free enzyme activity. If the activity of immobilized enzyme is improved, we may observe faster diffusion coefficients in the presence of substrates. Another factor for

consideration is particle shape. In the case of high aspect ratio rod-shaped motors, the asymmetry is more pronounced. Also for metallic rods rotational diffusion is predominantly confined to two dimensions, whereas in PS-microspheres the rotational diffusion is not confined to two dimensions.

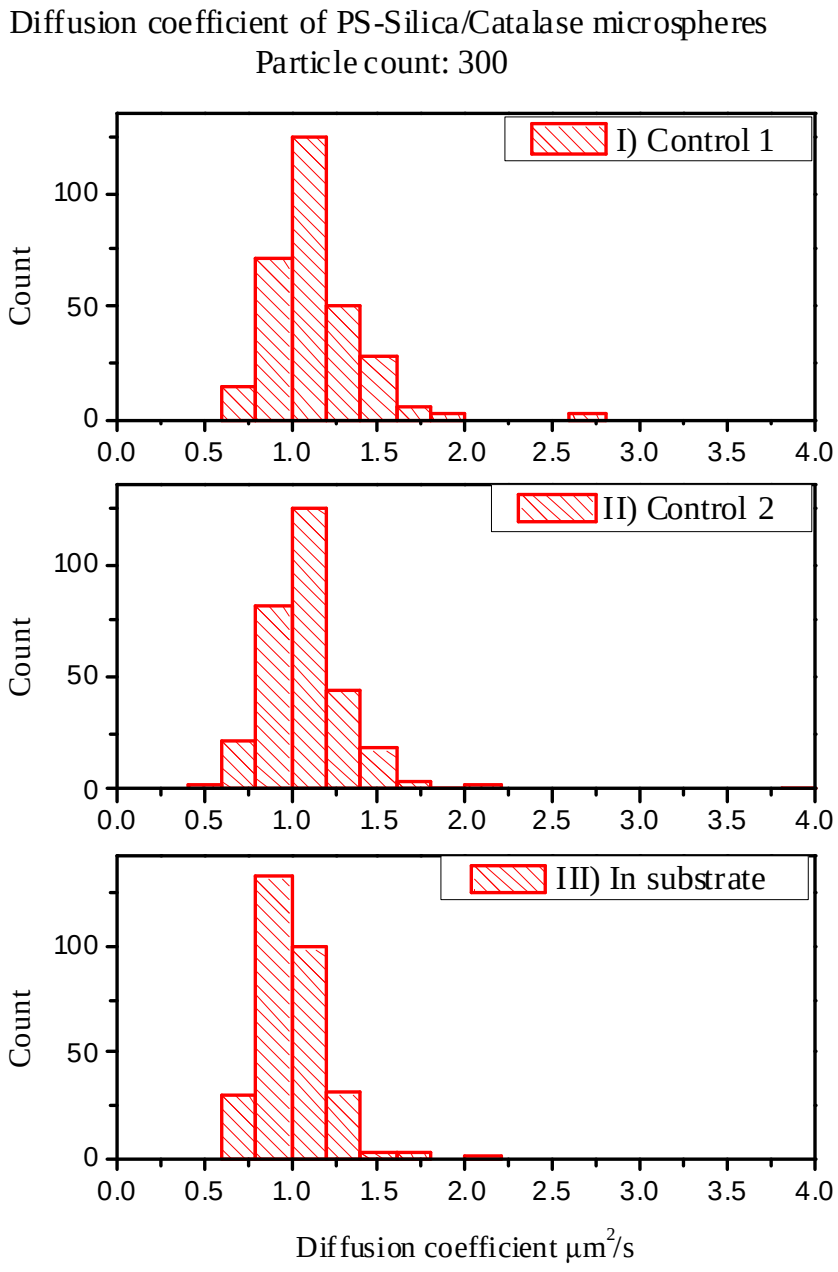

Figure **5-4**: Histogram of PS-Silica/Catalase particles in: I) Deionized water, II) In H_2O_2 when catalase is inactivated, and III) In H_2O_2 substrate. No enhancement of diffusion coefficient was observed in the presence of substrate.

5.4 Conclusions

In this chapter the feasibility of designing a self-difusiophoresis based micromotor, powered by an enzymatic reaction was explored. Diffusion coefficients of Janus type particles with catalase (PS-Silica/Catalase) in the presence and absence of H_2O_2 substrate were monitored. No enhancement of diffusion coefficient was observed in the presence of the substrate. The poor activity of the enzyme post-immobilizaion is most likely the major contributing factor. Enzyme activity may be improved by adding a longer spacer between the enzyme and particle.

This system is worth investigating further for a number of reasons. Firstly, the use of catalase affords the fabrication of a biocatalyst powered, self-diffusiophoretic system. Catalase is among the most robust and efficient enzymes known, making it a good choice for a catalyst powered micromotors. Secondly, it would be interesting to see if diffusiophoresis based motion, powered due to gradients of neutral species (H_2O_2, O_2 and H_2O in this case) is feasible. The predominant mechanism of motility in Pt-Au motors is self-electrophoresis. Sen et al. have reported powered motion of microparticles via diffusiophoresis arising from ion gradients.[21] In addition, there have been reports of micromotors powered by Pt functionalized particle by Golestenian et al.[22] The authors report that a self-diffusiophoresis mechanism in operation. A more detailed comparision of H_2O_2 turnover activity per particle in the enzymatic system and Pt only system (no other metal) needs to be done as both these systems decompose H_2O_2 via non electrochemical pathways. In such a scenario, propulsion due to netural product gradients

is likely the predominant mechanism of motility. However osmotic propulsion effects may also play a role.[23] The possibility of other mechanisms such as self-electrophoresis operating in the Pt-microsphere system needs to be examined, where different sites on the Pt surface may act as anode and cathode.

5.5 References

(1) Paxton, W. F.; Kistler, K. C.; Olmeda, C. C.; Sen, A.; St. Angelo, S. K.; Cao, Y.; Mallouk, T. E.; Lammert, P. E.; Crespi, V. H. *J. Am. Chem. Soc.* **2004**, *126*, 13424-13431.

(2) Dhar, P.; Fischer, T. M.; Wang, Y.; Mallouk, T. E.; Paxton, W. F.; Sen, A. *Nano Lett.* **2006**, *6*, 66.

(3) Wang, Y.; Hernandez, R. M.; Bartlett, D. J.; Bingham, J. M.; Kline, T. R.; Sen, A.; Mallouk, T. E. *Langmuir* **2006**, *22*, 10451-10456.

(4) Sundararajan, S.; Lammert, P. E.; Zudans, A. W.; Crespi, V. H.; Sen, A. *Nano Letters* **2008**, *8*, 1271-1276.

(5) Burdick, J.; Laocharoensuk, R.; Wheat, P. M.; Posner, J. D.; Wang, J. *J. Am. Chem. Soc.* **2008**, *130*, 8164-8165.

(6) Wang, Y.; Fei, S.-t.; Byun, Y.-M.; Lammert, P. E.; Crespi, V. H.; Sen, A.; Mallouk, T. E. *J. Am. Chem. Soc.* **2009**, *131*, 9926-9927.

(7) Ibele, M. E.; Wang, Y.; Kline, T. R.; Mallouk, T. E.; Sen, A. *J. Am. Chem. Soc.* **2007**, *129*, 7762-7763.

(8) Vicario, J.; Eelkema, R.; Browne, W. R.; Meetsma, A.; La Crois, R. M.; Feringa, B. L. *Chem. Commun.* **2005**, *2005*, 3936.

(9) Pantarotto, D.; Browne, W. R.; Feringa, B. L. *Chem. Commun.* **2008**, 1533-1535.

(10) Mano, N.; Heller, A. *J. Am. Chem. Soc.* **2005**, *127*, 11574-11575.

(11) Fersht, A. *Enzyme Structure and Mechanism*; W.H.Freeman and Company: New York, 1984.

(12) *Class I Oxidoreductases*; Springer: Berlin, 2006.

(13) Zidoni, E.; Kremer, M. L. *Arch. Biochem. Biophys.* **1974**, *161*, 658.

(14) Murthy, R. N. M.; Reid, T. J.; Sicignano, A.; Tanaka, N.; Rossman, G. *J. Mol.Bio* **1981**, 465.

(15) Golestanian, R.; Liverpool, T. B.; Ajdari, A. *Phys. Rev. Lett.* **2005**, *94*, 220801.

(16) Howse, J. R.; Jones, R. A. L.; Ryan, A. J.; Gough, T.; Vafabakhsh, R.; Golestanian, R. *Phys. Rev. Lett.* **2007**, *99*, 048102.

(17) Goldenberg, L. M.; Wagner, J.; Stumpe, J.; Paulke, B.-R.; Garnitz, E. *Langmuir* **2002**, *18*, 5627-5629.

(18) Reid, T. J.; Murthy, M. R.; Sicignano, A.; Tanaka, N.; Musick, W. D.; Rossmann, M. G. *Proc. Natl. Acad. Sci. U.S.A.***1981**, *78*, 4767-4771.

(19) Pantarotto, D.; Browne, W. R.; Feringa, B. L. *Chem. Commun.* **2008**, 1533.
(20) Cetinus, S. A.; Oztop, N. H. *Enzyme and Microbial Technology* **2003**, 889.
(21) Ibele, M.; Mallouk, T. E.; Sen, A. *Angew. Chem., Int. Ed.* **2009**, *48*, 3308-3312.
(22) Howse, J.; Jones, R.; Ryan, A.; Gough, T.; Vafabakhsh, R.; Golestanian, R. *Phys. Rev. Lett.* **2007**, *99*, 048102.
(23) Córdova-Figueroa, U. M.; Brady, J. F. *Phys. Rev. Lett.* **2008**, *100*, 158303.

Chapter 6

Summary and Conclusions

Our group has reported the autonomous motion of Pt-Au motors in hydrogen peroxide fuel solutions[1]. Initially surface tension was believed to be responsible for motor function however self-electrophoresis was proposed as a hypothesis for the observed motility.[2] In the first chapter, the self-electrophoresis mechanism of motility in Pt-Au micromotors was investigated. Negatively charged Pt-Au rods move Pt end forward. Reversal of the Pt-Au motor direction, upon changing the surface charge was observed. This result, along with experiments performed by others on surface immobilized catalysts and bimetallic rods (Ru-Au etc.), indicate that the predominant mechanism of motility is indeed due to the bipolar decomposition of the peroxide fuel.[3-5]

In the third chapter, the application of these motors for transport of colloidal cargo was demonstrated.[6] The motors retained their motility post cargo attachment. Motors slowed down when attached to cargo and the effect of cargo diameter on motor speed was studied in a quantitative manner. A good agreement with the empirically observed motor-cargo speed and the speeds computed by the completed double-layer boundary-integral equation method (CDL-BEIM) was found. Incorporation of Ni segments allowed for better control in rod motion in the presence of an external magnetic field. In the fourth chapter, two routes for cargo drop-off namely, i) silver dissolution assisted drop-off and ii) photocleavable linker assisted drop-off were described. In each case the link connecting the motor and cargo is cleaved upon exposure to UV light.[7]

In the fifth chapter the feasibility of fabricating enzyme powered motors was explored. Catalase was functionalized asymmetrically on 0.5 µm diameter, polystyrene-silica microspheres. Diffusion coefficients of the microspheres were tracked in the presence and absence of H_2O_2 substrate. No enhancement in diffusion coefficient was observed in the presence of substrate. Low activity of immobilized enzyme activity may be a contributing factor. This system needs further investigation to determine whether asymmetric gradients of neutral species can power microscale objects via self-diffusiophoresis.

The results presented in this thesis have important implications for the design and applications for catalytic micromotors. The Pt-Au/H_2O_2 system (in the year 2004) was the first report of a synthetic catalytic micromotor.[1] In the biological world, motility of microbes that propel themselves through fluid media via appendages like flagella or cilia is well-known.[8] So too are phoretic transport modes of microparticles via external fields (electrophoresis, magnetophoresis, thermophoresis, diffusiophoresis and osmophoresis.) etc).[9] The demonstration of Pt-Au chemical locomotors introduced a novel route for auto-propulsion of microscale objects by self-generated gradients. The Pt-Au-microsphere cargo system serves as a prototype for transport and delivery of payloads in the mesoscale. Applications such as bottom-up assembly of superstructures, drug delivery and sensory applications for micromotors have been proposed.[10]

While the Pt-Au/H_2O_2 system was a seminal report in the field of synthetic micromotors, this system is not without drawbacks. Limitations exist for the system at multiple levels i.e., in materials used, reaction byproducts and mechanism of motility. The oxidative nature of the peroxide fuel, and use of noble metal catalysts precludes the

use of the system for many in vivo as well as in vitro applications. Production of oxygen bubbles as byproduct also presents challenges, as presence of bubbles not only distorts the field of view but bubble expansion generates unwanted disturbances in the medium.

Pt-Au motors propel themselves through H_2O_2 solutions by bipolar decomposition of the fuel. They move at speeds of few body lengths, much like many naturally occurring bacteria. However due to the nature of the propulsive mechanism – self-electrophoresis, the system has a low tolerance for ions in surrounding media. In solutions of 1 mM $NaNO_3$, motor speed decreased by 80% compared to speeds in deionized water.[5] This aspect of the Pt-Au/H_2O_2 system makes it even more limited in its applicability.[§§,11] Therefore, it is essential to explore newer materials, catalytic reactions and mechanisms to make progress in the realm of chemically powered micromotors.

One such mechanism that may be worth exploring is osmophoresis. Sackmann et al.[12] showed that vesicles composed of both dimyristoyl phosphatidycholine (DMPC) and stearoyl oleoyl phosphatidycholine (SOPC), when placed in a gradient of a neutral solute such as sucrose, migrated toward regions of lower solute concentrations The vesicles (10 μm diameter) propelled themselves at an average speed of 1 μm/s in a gradient of 10 mM sucrose. The mechanism of propulsion was attributed to the osmotic pressure difference experienced at the poles of the vesicle. When placed in a gradient of solute, the semi-permeable vesicle selectively blocks the solute, while permitting solvent molecules to

---

[§§] Several groups have studied the relationship between transcellular ion currents observed in living cells, and their motility. It has been suggested that self-generated electric fields may provide a means for propulsion in these systems. [11] While the topic remains under investigation, it would be interesting to see if self-electrophoresis contributes to motility in living systems, mainly because biosystems operate at higher ionic strength environments than experimental conditions (deionized water with conductivity of 18 MΩ˙cm) used for self-electrophretic Pt-Au motors.

pass through. The active transport of solvent from one end of the vesicle to the other propels the vesicle forward. Some principles for osmophoresis have been discussed by Anderson.[13] One can think of designing an auto-osmophoretic motor, powered by self generated gradients.

Figure **6-1** shows a schematic of an asymmetrically functionalized osmophoretic motor. The vesicle is asymmetrically functionalized with a catalyst on one side and placed in a uniform solution of substrate A. The catalyst turns over one mole of reactant A to two moles of product B. The osmotic pressure on the left side (non catalytic pole) is greater than the right side (pole catalyzing the conversion of A to 2B), resulting in vesicle motion toward regions of higher osmotic pressure or lower solute concentration regions. As a first step, the design of Janus-type vesicle particles needs to be explored. There have been several innovative reports on the synthesis of Janus particles that would aid in the design of such structures.[14] It is worth noting the similarity in the osmophoresis and self-electrophoresis; both involve active transport of the fluid from one pole of the object to the other. The use of vesicle based motors lends such a system the advantage of biocompatibility.

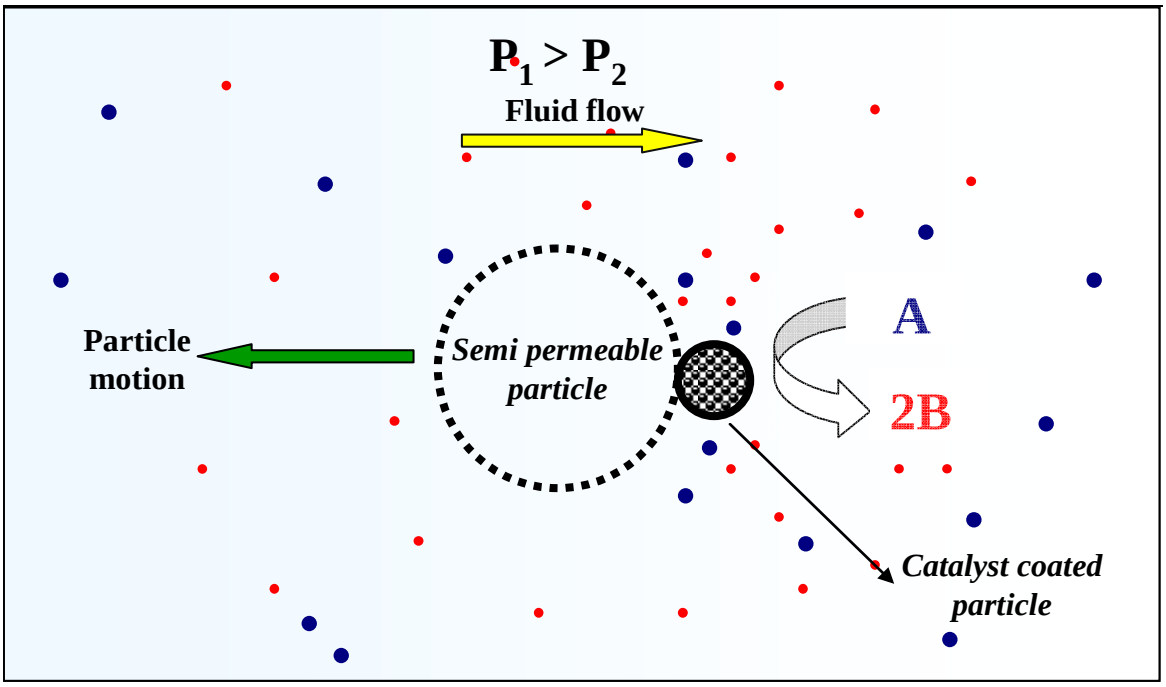

Figure **6-1**: Schematic for the design of a self-osmophoretic motor powered by a catalytic reaction. A semi-permeable particle such as a vesicle that allows transport of the solvent molecules through it but impermeable to solute molecules, is asymmetrically functionalized with a catalyst coated particle. The catalyst facilitates the conversion of one mole of reactant A, to two moles of product B. When placed in a solution of uniform concentration of 'fuel' A, due to the catalytic conversion of A to B, an osmotic pressure gradient is generated at the two poles of the vesicle. The osmotic pressure P_1, on the left pole of the vesicle is greater than the osmotic pressure P_2, on the right pole (the side bearing the catalyst). The imbalance in pressure drives fluid from left to right, resulting in particle motion with the catalytic end trailing.

Immense progress has been made in the field of catalytic micromotors with numerous contributions from several research groups.[15-18] While there is a need to look ahead in terms of motors powered by newer reactions and exploring applications, there remain several unanswered questions in the noble metal catalyst-H_2O_2 fuel based motors. In the currently known systems, motor dimensions are either larger than 80 μm or smaller than 10 μm.[19-21] In the larger motors, bubble propulsion is the mechanism in operation. The only two exceptions are: a) the 150 μm diameter

Pt-Au gears system designed by fabricated by Catchmark et al. and, b) the millimeter sized bi-enzymatic system designed by Heller et al. which are powered via self-electrophoresis.[22,23] Bi-metallic (or multi-metallic) motors under 10 μm are all also driven by self-electrophoresis. There is a gap in our understanding of what mechanism (phoretic or bubble propulsion) would be favored in motors within the 10 – 80 μm size range. Mallouk et al. studied the motion of lithographically fabricated, 20 μm Pt-Au structures on photoresist scaffolds, but the mechanism of motility in these systems is not clear.[24]

The question of bubble propulsion vs. phoretic transport as the dominant contributor to motility is even less understood in Pt-only systems in the sub-10 μm size regime. A case in point is the observation of bubble-propulsion in Si-Pt motors designed by Zhao et al., whereas diffusiophoresis is attributed to the motility of 1.62 μm diameter Pt-PS microspheres system designed by Golestanian et al.[25,26] The motility of 1 μm length Pt only rods is also not well-studied.[21] To add to the complexity, if self-diffusiophoresis is indeed the operative mechanism in the Golestanian (Pt-PS microsphere) system, why do other catalytic particles (Au-catalase rods and PS-Silica/Catalase microspheres) which likely have higher or comparable per particle turnover numbers, not exhibit motility.[***,27]

While we channel more efforts to design better motors, we also need to reevaluate our goals for the field of micromotor research with a renewed perspective. A critical evaluation of some of currently proposed applications is required. For example,

---

[***] See Chapter 5 of this thesis for details.

applications for micromotors as sensors or as agents of transport and delivery in biomedicine have been suggested.[28] As roving sensors, what advantages would motors provide over existing analytical techniques? If chemical locomotors are capable of detecting and mapping the concentration profile of an analyte in a defined region, how can feedback other than visual mapping (as this may not be feasible in all experimental conditions) be obtained? If we are able to design motors that can function in physiological conditions, what are the ramifications of introducing a self-propelled object in biosystems that are already endowed with circulatory mechanisms of their own?

Irrespective of some of the challenges outlined in this chapter, the topic of catalytic micromotor research has undoubtedly supplemented the existing knowledge and aided in understanding of motion of microscale objects. There has been a renewed interest in field from the perspective of physics of motion at the small scale and design aspects of micromotor fabrication, as evidenced by the abundance of experimental as well as theoretical studies on the subject. The results presented in this thesis have added to the understanding of mechanistic, as well as application oriented facets of catalytic micromotor research and would be of use for future endeavors in the field.

6.1 References

(1) Paxton, W. F.; Kistler, K. C.; Olmeda, C. C.; Sen, A.; St. Angelo, S. K.; Cao, Y.; Mallouk, T. E.; Lammert, P. E.; Crespi, V. H. *J. Am. Chem. Soc.* **2004**, *126*, 13424-13431.

(2) Paxton, W. F.; Sen, A.; Mallouk, T. E. *Chem. Eur. J.* **2005**, *11*, 6462-6470.

(3) Kline, T. R.; Paxton, W. F.; Wang, Y.; Velegol, D.; Mallouk, T. E.; Sen, A. *J. Am. Chem. Soc.* **2005**, *127*, 17150-17151.

(4) Wang, Y.; Hernandez, R. M.; Bartlett, D. J.; Bingham, J. M.; Kline, T. R.; Sen, A.; Mallouk, T. E. *Langmuir* **2006**, *22*, 10451-10456.

(5) Paxton, W. F.; Baker, P. T.; Kline, T. R.; Wang, Y.; Mallouk, T. E.; Sen, A. *J. Am. Chem. Soc.* **2006**, *128*, 14881.

(6) Sundararajan, S.; Lammert, P. E.; Zudans, A. W.; Crespi, V. H.; Sen, A. *Nano Lett.* **2008**, *8*, 1271-1276.

(7) Sundararajan, S.; Sengupta, S.; Ibele, M.; Sen, A. *Unpublished.* **2010**.

(8) Lauga, E.; Powers, T. R. *Rep. Prog. Phys.* **2009**, *72*, 096601.

(9) Anderson, J. L. *Ann. Rev. Fluid Mech.* **1989**, *21*, 61-99.

(10) Paxton, W. F.; Sundararajan, S.; Mallouk, T. E.; Sen, A. *Angew. Chem. Int. Ed.* **2006**, *45*, 5420.

(11) Lammert, P. E.; Prost, J.; Bruinsma, R. *J. Theor. Biol.* **1996**, *178*, 387-391.

(12) Nardi, J.; Bruinsma, R.; Sackmann, E. *Phys. Rev. Lett.* **1999**, *82*, 5168 - 5171.

(13) Anderson, J. L. *Ann. N. Y. Acad. Sci.* **1986**, *469*, 166-177.

(14) Pawar, A. B.; Kretzschmar, I. *Macromol. Rap. Commun.* **2010**, *31*, 150-168.

(15) Paxton, W. F.; Sundararajan, S.; Mallouk, T. E.; Sen, A. *Angew. Chem., Int. Ed.* **2006**, *45*, 5420-5429.

(16) Sánchez, S.; Pumera, M. *Chem. Asian J.* **2009**, *4*, 1402-1410.

(17) Wang, J.; Manesh, K. M. *Small* **2010**, *6*, 338-345.

(18) Mirkovic, T.; Zacharia, N. S.; Scholes, G. D.; Ozin, G. A. *Small* **2010**, *6*, 159-167.

(19) Stock, C.; Heureux, N.; Browne, W. R.; Feringa, B. L. *Chem. Eur. J.* **2008**, *14*, 3146-3153.

(20) Solovev, A. A.; Mei, Y.; Ureña, E. B.; Huang, G.; Schmidt, O. G. *Small* **2009**, *5*, 1688-1692.

(21) Paxton, W. F.; Kistler, K. C.; Olmeda, C. C.; Sen, A.; St Angelo, S. K.; Cao, Y. Y.; Mallouk, T. E.; Lammert, P. E.; Crespi, V. H. *J. Am. Chem. Soc.* **2004**, *126*, 13424.

(22) Catchmark, J. M.; Subramanian, S.; Sen, A. *Small* **2005**, *1*, 202-206.

(23) Mano, N.; Heller, A. *J. Am. Chem. Soc.* **2005**, *127*, 11574-11575.

(24) Wang, Y.; Fei, S.-t.; Crespi, V. H.; Sen, A.; Mallouk, T. E. *Materials Research Society Symposium Proceedings*; Materials Research Society, **2009**, *1135*, 1103-1109.

(25) He, Y.; Wu, J.; Zhao, Y. *Nano Lett.* **2007**, *7*, 1369-1375.

(26) Howse, J.; Jones, R.; Ryan, A.; Gough, T.; Vafabakhsh, R.; Golestanian, R. *Phys. Rev. Lett.* **2007**, *99*, 048102.

(27) Dhar, P.; Fischer, T. M.; Wang, Y.; Mallouk, T. E.; Paxton, W. F.; Sen, A. *Nano Lett.* **2006**, *6*, 66.
(28) Wang, J. *ACS Nano* **2009**, *3*, 4-9.

VITA

Shakuntala Sundararajan received her B.Sc. Chemistry degree in 2001 from Stella Maris College, India. She then completed her M.Sc. Chemistry degree in 2003 from the Indian Institute of Technology Madras, India. She joined the Department of Chemistry at the Pennsylvania State University, University Park in Fall 2003 under the guidance of Dr. Ayusman Sen. Her graduate research has consisted of studying the mechanism of motility in microscale Pt-Au motors and exploring applications for the same.